University of Reading

Thiolated and PEGylated organosilica nanoparticles: A model carrier for drug delivery to the hair follicles and vitreous humour

Jamila Harib Al Mahrooqi

Submitted as partial fulfillment for the degree of Doctor of Philosophy

School of Pharmacy

April 2021

Declaration of original authorship

‘Declaration: I confirm that this is my own work and the use of all material from other sources has been properly and fully acknowledged.’

Jamila Al Mahrooqi

April 2021

I dedicate this thesis to my father, to the soul of my mother who was always encouraging me to learn, to the soul of His Majesty Sultan Qaboos for the grant he gave for postgraduate scholarships and to the soul of my beloved ones who passed away during this pandemic.

Acknowledgment

First and foremost, praises and thanks to Allah, the Almighty, for His showers of blessings throughout my research work to complete the research successfully.

I would like to express my deep and sincere gratitude to my supervisors, Professor Vitaliy Khutoryanskiy and Professor Adrian Williams for their support, inspiration, patience, and invaluable guidance throughout my research. Their immense knowledge and plentiful experience have encouraged me in all the time of my academic research.

The University of Reading, the Chemical Analysis Facility are acknowledged for providing access to transmission electron microscopy, fluorescence microscopy, fluorescence spectrophotometer and thermogravimetric analysis. Ministry of Higher Education, Research and Innovation, Sultanate of Oman for funding and Oman College of Health Sciences for nomination for the scholarship. I would also like to thank Dr. Ali Al Hinai for his support and Professor Mustafa Fahmy for his endless encouragement and support since I was his student.

My heartfelt thanks go to the pleasant people that helped with various analyses, Dr. Daulet Kaldybekov, Dr. Sam Bizley, Dr. Peter Harris, Dr. Pedro Rivas Ruiz and other wonderful people that I cannot afford to express all their names. I would like to thank my friends, lab mates, colleagues and research team (Twana, Dami, Roman, Sam, Ibrahim, Az, Nancy, Natalia, Fhata and all those who left and who joined the group recently) for a cherished time spent together in the lab, and in social settings.

My biggest thank go to my husband Jamal and my children Almunther, Arwa, Marwa and Muhanad for their support, patience, sacrifice, and encouragement. I would also like to thank my father, my siblings, and my in-laws for their endless support. Special thanks to my parents in-law for taking care of my children who were not able to join me and their endless encouragement and to my sweet sisters in-law Eiman and Jokha for being always with me whenever I need them. This would be impossible to achieve without their support.

Finally, I would like to thank my friends and neighbors Fazilet, Charu, Asmita, Dr Faheem, Bishara and Saba for their support. My friends, Dalal, Faten, Luma, Fatma, Afnan, Laila, Maha, Najat, Shamsa and Muna. I have an endless list of friends who I consider them gift of Allah, The

Almighty, as they were always there for me when I needed support and they made me feel home with their kindness and hospitality. I feel I am blessed; I was surrounded with so many supporting and good friends and whenever I needed help someone was there for me.

Jamila Al Mahrooqi

April 2021

Abstract

Thiol functionalised organosilica nanoparticles were explored in this PhD project as a model carrier for targeted drug delivery to the hair follicles and the posterior segment of the eye. These two organs were chosen as they are equipped with multiple barriers which present a challenge for drug delivery and the development of a novel drug delivery system is required. Modification of these nanoparticles with polyethylene glycol (PEG) and fluorescent dye was feasible as they are readily functionalised.

The first chapter provides an overview of thiol functionalised nanoparticles, their synthesis, and possible applications. In addition, the structure of the skin and the eye and barriers to drug delivery are discussed. Chapter two focuses on the synthesis of particles with predetermined size and was achieved after exploring different reaction parameters that govern the characteristics of the resulting nanoparticles using a pre-established modified Stöber protocol. The nanoparticles were characterised using several methods including dynamic light scattering, transmission electron microscopy and Ellman's assay. Equations that can be used to design particles with the required size by changing the dielectric constant of the solvents used or varying the concentration of the catalyst NaOH when dimethylsulfoxide (DMSO) is used were established. The smallest nanoparticles (45 ± 3 nm) with high thiol content (249 ± 30 μmol/g) were produced when DMSO was used as the solvent and had a narrow polydispersity (0.181) and zeta potential of (-55 ± 7 mV); therefore, these particles were selected for subsequent studies. The mucoadhesive properties of these nanoparticles to several mucosal tissues including the eye, urinary bladder and the intestine were previously studied and modification with PEG was reported to improve the penetration and diffusion of the nanoparticles. Thus, in the third chapter, the nanoparticles were modified by PEGylation and fluorescently labelled and their penetration to the follicular appendages to overcome the barrier function of the stratum corneum was investigated using a tape stripping method and fluorescence microscopy. PEGylation was found to significantly improve the penetration of the nanoparticles with better penetration of particles functionalised with higher molecular weight PEG with penetration depth values of 1400 μm for PEGylated 5000 Da nanoparticles and 450 μm for PEGylated 750 Da nanoparticles. The fourth chapter investigates the diffusion of thiolated and PEGylated (750, 5000 and 10000 Da) nanoparticles in the vitreous humour (decanted into a cuvette) using a novel *in vitro* fluorescence-based method and measuring the distance travelled overtime. PEGylation enhanced the diffusion of the nanoparticles in the vitreous humour as they travelled around 20 μm compared to thiolated particles which did not diffuse. The final chapter discusses the general conclusions and possible future work. These nanoparticles were found to be a good model to explore surface modification of nanoparticles in drug delivery.

List of publications

Al Mahrooqi, J., Mun, E., Williams, A. and Khutoryanskiy, V., (2018). Controlling the Size of Thiolated Organosilica Nanoparticles. *Langmuir*, 34(28), pp.8347-8354.

Al Mahrooqi, J., Khutoryanskiy, V. and Williams, A., (2021). Thiolated and PEGylated silica nanoparticle delivery to hair follicles. *International Journal of Pharmaceutics*, 593, p.120130.

List of conferences

Pharmacy PhD showcase, University of Reading, March 2017 - Poster

UK colloids 2017, Manchester, July 2017 - Poster

Pharmacy PhD showcase, University of Reading, April 2018 - Talk

4th annual keele nanopharmaceutical symposium, Keele University, June 2018 - Poster

78th world FIP congress, Glasgow, September 2018 - Poster

APS@FIP, Glasgow, September 2018 - Poster

McBain colloidal conference, London, December 2018 - Poster

Omani open day, Newcastle University, March 2019 - Poster

Pharmacy PhD showcase, University of Reading, April 2019 – Talk

1st Online British-Kazakh-Russian conference on drug delivery, May 2020 – Talk

Omani student open day, virtual, November 2020 - Poster

Awards:

Outstanding academic performance for the academic year 2017/18 award by Oman cultural attaché' of London, March 2019

Best poster in scientific poster competition in Omani open day, Newcastle, March 2019

Best poster in scientific poster competition in Omani open day, virtual, November 2020

Table of contents

List of figures

Chapter 1

Chapter 2

Chapter 3

Chapter 4

List of tables

Chapter 2

Chapter 3

Chapter 4

Abbreviations

AA	Acrylic acid
AcN	Acetonitrile
ANOVA	Analysis of variance
APTES	3-aminopropyl triethoxysilane
VGEF	Vascular endothelial growth factor
CPD	Concentrated polymer brushes
CTAB	Cetyltrimethylammonium bromide (cetrimonium bromide)
DEA	Diethylamine
DLS	Dynamic light scattering
DMF	Dimethyl formamide
DMSO	Dimethylsulfoxide
DNTB (Ellman's reagent)	5,5'-dithio-bis-(2-nitrobenzoic acid)
FDA	Food and Drug Administration
GSH	Glutathione
HEC	Hydroxyethylcellulose
HECEs	Human corneal epithelial cells
5-IAF	5-(iodoacetoamido)-fluorescein
MPDMS	3-mercaptopropylmethyldimethoxysilane
MPES	3-mercaptopropyltriethoxysilane
MPTS	3-mercaptopropyltrimethoxysilan
NMP	N-Methyl-2-pyrrolidone
NMR	Nuclear magnetic resonance
OCT	Optimal cutting temperature compound
PAA	Poly(acrylic acid)
PBS	Phosphate buffered saline
PEG	Polyethylene glycol
PEO	Poly(ethylene oxide)
PEOZ	Poly(2-ethyl-2-oxazoline)
PLA	Polylactic acid
PLGA	Poly (lactide-*co*-glycolide)
PMOZ	Poly(2-methyl-2-oxazoline)
PNIPAM	Poly(N-isopropyl acrylamide)
PNPOZ	Poly(2-n-propyl-2-oxazoline)
POE/POP	Polyoxyethylene– polyoxypropylene
POZ	Poly(2-alkyl-2-oxazoline)
PVP	Poly(N-vinylpyrrolidone)
SANS	Small angle neutron scattering
SDPB	Semi-dilute polymer brush
TEA	Triethylamine
TEOS	Tetraethyl orthosilicate
TEM	Transmission electron microscopy
THF	Tetrahydrofuran
TSNPs	Thiolated silica nanoparticles

Chapter 1

Overview of thiol functionalised silica nanoparticles: the role of nanoparticles in overcoming the barriers in the eye and skin

This chapter illustrates the synthesis, properties, and possible biomedical applications of thiol functionalised nanosystems. In addition, the structure of the eye and the skin, with a focus on the barriers to drug delivery, are discussed. Strategies to overcome these barriers are also discussed.

Introduction:

Nanotechnology has numerous potential pharmaceutical benefits such as enhancing drug targeting and efficacy, thereby reducing side effects. Nanomaterials have unique properties, due to their size, which often differ than those on macroscale. In the size range 1-300 nm, nanomaterials provide very high surface area to weight ratios compared to larger objects resulting in higher reactivity, conductivity and properties related to light reflection and refraction. They also have different elastic, tensile, and magnetic properties. These characteristics make nanoparticles good candidates for applications in several fields including healthcare, energy, and information technology. General applications in healthcare are in imaging, diagnostics and drug carriers [1–5]. Doxil, a liposomal formulation of doxorubicin, is an anticancer drug which is considered as the first FDA approved nanodrug with prolonged drug circulation, efficacy and fewer side effects compared to conventional formulation [1,6]. Diprivan, limethason and diazemuls are examples of nano-emulsion formulations for intravenous delivery of poorly water soluble drugs [7]. Among inorganic nanoparticles, gold nanoparticles are extensively exploited for biomedical applications especially for cancer therapy and imaging [2,4,5]. Similarly, silica nanoparticles are used in drug delivery as they are biocompatible, easy to functionalise, and cheaper than gold nanoparticles and can be inorganic or organic depending on the silica precursor [4,8,9]. Inorganic silica nanoparticles are prepared from tetraethylorthosilane while organic silica nanoparticles are prepared from substituted alkoxysilanes [10–14]. Thiol functionalised organosilica has gained popularity as the resulting nanoparticles exhibit mucoadhesive properties and can be modified to gain penetrative properties [8,11,15–20]. Here, we focus on thiol functionalised silica nanoparticles and their potential biomedical and pharmaceutical applications.

Synthesis, properties, biomedical and pharmaceutical applications of thiolated silica nanoparticles and microparticles:

Silica nanoparticles can be synthesised from tetraethyl orthosilicate (TEOS) using the Stöber method or a microemulsion method [8,12]. Stöber et al. reported the formation of spherical silica nanoparticles with a size range of less than 0.05 µm to 2 µm by means of hydrolysis and subsequent condensation of TEOS to silicic acid in alcoholic solutions using ammonia as a catalyst [10]. The microemulsion technique involves the formation of oil in water (O/W) micelles or water in oil (W/O) reverse micelles. Surfactants such as, Tweens and Pluronics are added to stabilise the micelles and act as nanoreactors for the particles synthesis in the presence of catalysts, e.g., hydrochloric acid or ammonia [8,21,22]. The size range reported by Esquena et al. when using this method was 2-1000 µm when hydrochloric acid was used and 0.5-10 µm when ammonia was used [21]. As the surface of these nanoparticles are rich in silanol groups (Si-OH), they can be further modified using organosilica source, such as, 3-mercaptopropyltrimethoxysilane (MPTS) and 3-aminopropyl triethoxysilane (APTES). This method was adopted but using different silica precursors or using an organosilica source in addition to TEOS [8].

Thiolated materials are exploited in the design of dosage forms for drug delivery as they form disulfide bonds with mucus. Thiomers which are thiolated polymers were reported to improve mucoadhesion, enzyme inhibiting and permeation properties [23–27]. Nakamura et al. used the thiol functionalized organosilica source 3-mercaptopropyltrimethoxysilane (MPTS) to synthesise of nanoparticles using the Stöber method and compared them to nanoparticles synthesised using TEOS. They reported higher negative values of zeta potential, larger size with wide polydispersity and greater ability to absorb protein in case of MPTS nanoparticles compared to TEOS. However, the formation of the nanoparticles was slower and took up to 3 days when MPTS was used, whereas nanoparticles formed within 9 hours when using TEOS. TEOS nanoparticles start forming by hydrolysis of the silica precursor by ammonium hydroxide followed by self-condensation, formation of silica matrices and precipitation of the nanoparticles. They reported that the reaction mixture becomes cloudy within a few hours after starting the synthesis of MPTS nanoparticles, but the nanoparticles were not recovered after the washing procedure they used in their experiments. They hypothesise that MPTS micelles were formed prior to hydrolysis and polymerisation of the micelles to form the nanoparticles. Further modification in the synthesis method was sought for more rapid formation of nanoparticles with narrow polydispersity, for biomedical use. Subsequently, the same researchers prepared nanoparticles using three different thiol-organosilica sources 3-mercaptopropyltrimethoxysilane, 3-mercaptopropyltriethoxysilane (MPES) and 3-mercaptopropylmethyldimethoxysilane (MPDMS) using either Stöber method or aqueous solvent synthesis with either 2% or 27% ammonium hydroxide. They reported variation in nanoparticles formation trends and rates depending on the organosilica precursor used, concentrations, and synthetic conditions. They reported that the Stöber method was not suitable for the formation of thiolated silica nanoparticles and found that exclusion of alcohol and using 27% of ammonium hydroxide were optimum for the formation of the nanoparticles.

They also functionalised the nanoparticles with fluorescent dye internally in a one-pot synthesis. Moreover, the nanoparticles were functionalised externally with fluorescent dye maleimide and protein maleimide by covalent bonding with thiol groups [13]. Modification of these nanoparticles with fluorescent dyes and proteins have potentials for use in different applications, such as biomedical analysis, chip-based technology, multi-target detection systems, imaging in vitro and in vivo, and drug delivery systems [12,14]. Later, they reported the synthesis of dual fluorescent thiol-organosilica nanoparticles as non-photoblinking quantum dots (thiol-OS-QD) by encapsulation of fluorescent dye and quantum dots by thiol-organosilica layer. The fluorescent properties of the nanoparticles were preserved under sever acid and alkali condition in comparison to the bare quantum dots. In addition, *in vivo* study of cells labelled with thiol-OS-QD were detected clearly with reduced photoblinking using multi-purpose zoom microscope. They also conjugated the nanoparticles with rituximab and incubated with Raji cells, a characterised B lymphoblastic cell line CD20 derived from patient with Burkitt’s lymphoma, for molecular imaging. Fluorescent microscopy images were clear and did not show any photoblinking or photobleaching [28].

Irmukhametova et al. modified the Stöber method and synthesised sub-100 nm thiolated silica nanoparticles from MPTS in dimethylsulfoxide (DMSO) in the presence of atmospheric oxygen and using sodium hydroxide as the catalyst. The resulting nanoparticles exhibited mucoadhesive properties and were retained on bovine ocular mucosal surfaces. In their experiments, they prepared nanoparticles by varying synthesis conditions and studied their effect on the characteristics of the resulting nanoparticles. When protic solvents were used, the resulting nanoparticles were larger due to rapid particles growth and aggregation as they are involved in the hydrolysis and subsequent condensation of methoxysilane groups. In addition, bubbling the reaction mixture with atmospheric oxygen mediated the formation of disulfide bridges from thiol groups and when hydrogen peroxide was used instead, the resulting nanoparticles had wider polydispersity. Moreover, 3-aminopropyltrimethoxysilane was used instead of MPTS but nanoparticles were not formed as MPTS self-condensation occurs via S-S bridge formation [11].

Melnyk et al. reported the synthesis of mesoporous silica microspheres with relatively highly ordered texture and functionalised with thiol groups using sol-gel self-assembly and spray drying which can have potential use in environmental remediation or metallic nano-particle syntheses. They used TEOS, hydrochloric acid and isopropanol, MPTS was added later for functionalisation and CTAB was added before spray drying [29].

The organosilica precursor 3-mercaptopropyltrimethoxysilane was used for the functionalisation of mesoporous silica nanoparticles with thiol groups for further modification. The nanoparticles were PEGylated and then conjugated to (S)-2-(4-isothiocyanatobenzyl)-1,4,7-triazacyclononane-1,4,7- triacetic acid (NOTA), TRC105 antibody and subsequently PEGylated then labelled to generate a complex ^{64}Cu-NOTA-mSiO$_2$-PEG-TRC105 nanoconjugate. TRC105 binds to human and murine CD105 which is expressed in xenograft tumour models, such as triple-negative breast cancer, pancreatic cancer, prostate cancer, and brain tumour. Transmission electron microscopy images revealed the formation of spherical nanoconjugates and dynamic light scattering measurement of the final size and net charge of the nanoconjugate was 168 ± 8.2 nm and -2.7 ± 1 mV. Tumour targeting of the nanoconjugates *in vivo* in a mouse model of breast cancer was reported and quantified noninvasively by positron emission tomography. In addition, a doxorubicin loaded nanoconjugate was injected intravenously to 4T1 tumour-bearing mice and doxorubicin targeted tumour delivery was reported [30]. Dong et al. used MPTS to attach gold into iron oxide nanoparticles to form core/shell nanocomposites. Scanning electron microscopy results and elemental analysis revealed the formation of spherical, monodispersed 150 nm nanocomposites with core/shell structure of Fe$_3$O$_4$@hybrid@Au. They reported effective killing of MCF-7 cancer cells (human breast adenocarcinoma cell line) with exposure to a NIR 808 nm laser irradiation with no influence on cell viability from both the nanocomposite and laser alone. They also reported the efficiency of the nanocomposite as a contrast agent for magnetic resonance imaging (MRI) and suggested further research on the potential use of these nanocomposites for MRI guided photothermal tumour therapy [31].

Degradation

Thiol groups are partially oxidised during the synthesis of nanoparticles, which results in the formation of disulfide bonds [11]. Disulfide bonds can be reduced by glutathione redox triggering which is based on the difference of intracellular and extracellular glutathione concentration which is several orders of magnitude higher intracellularly than extracellularly [32]. In addition, it was reported that the concentration of glutathione in cancer cells is considerably higher than normal cells due to their higher metabolic rate [33]. This variation in concentration was utilised to release drugs linked to their carrier via disulfide bonds after internalisation by a cell (Figure 1) [34] and for targeted delivery of drugs to cancer cells [32]. Moreover, introducing disulfide bonds to mesoporous silica nanoparticles can facilitate their cleavage by glutathione into small pieces after drug delivery and increase their biodegradability [35,36].

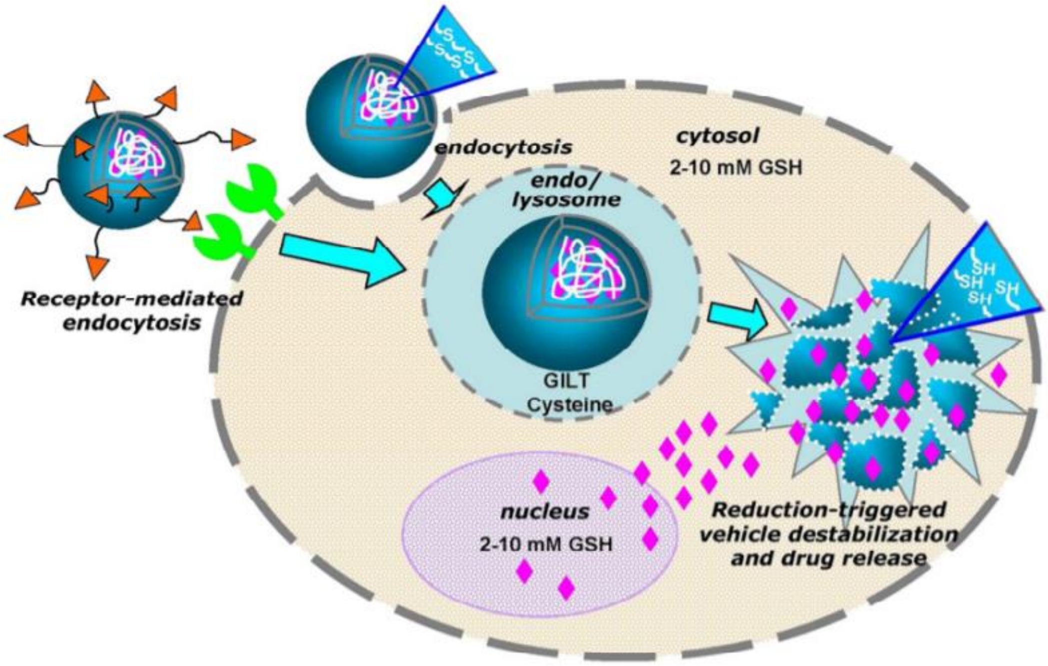

Figure 1: Schematic illustration of the intracellular trafficking pathway of GSH-responsive nano-vehicles including steps of cellular internalization, endosomal escape, reduction-triggered vehicle degradation, and drug release [34]**.**

Yang et al. prepared dendritic mesoporous organosilica nanoparticles with disulfide bonds and two different pore size. They reported a glutathione-responsive and structural-dependant biodegradation of nanoparticles. The degradation of these nanoparticles was slow in normal cells regardless of the pore size due to low levels of intracellular glutathione but nanoparticles with larger pore sizes showed faster degradation rate in cancer cells due to higher level of intracellular glutathione [37]. It was reported that incorporation of disulfide bonds in molecularly organic-inorganic hybridized hollow mesoporous organosilica nanocapsules enhanced their activity in physiological conditions, such as in the reducing microenvironment of tumour tissues and improved their biodegradation [38].

Doura et al. studied the relationship between the chemical structure of thiol-organosilica nanoparticles and their glutathione-responsive degradability. They synthesised hybrid nanoparticles were composed of variable proportions of two types of thiol-organosilicate, 3-mercaptopropyletriethoxysilane (MPTS) and 3-mercaptopropyl(dimethoxy)methylsilane (MPDMS). They carried out thermo-gravimetric analysis, solid-state ^{13}C NMR, Raman spectroscopic measurement and Ellman’s assay for the chemical characterisation of the resulting nanoparticles. They reported greater thiol content for particles prepared using higher proportion of MPTS, whereas increasing the proportion of MPDMS increased disulfide bonds within the nanoparticles structure. However, Ellman's assay results showed an increase in thiol content with increasing the concentration of MPDMS which contradicted results obtained from other tests and was related to the variability of the interior and exterior structure of the nanoparticles resulting from variation of concentration of silica precursors used and the availability of thiol groups to react with Ellman's reagent. The degradation of these nanoparticles in the presence of glutathione was studied using two concentrations, 10 and 40 mM of glutathione. The nanoparticles were incubated with 10 mM glutathione (corresponding to intracellular concentration in cancer cell) at 37 ºC for 2 or 7 days and transmission electron microscopic images were taken. The outer edges of nanoparticles prepared from MPTS were slightly affected after 7 days and as the concentration of MPDMS increase damage to the nanoparticles increased and occurred in shorter period. For instance, images taken for nanoparticles prepared from MPDMS alone after 2 days of incubation showed aggregates of partially collapsed nanoparticles and destroyed materials were observed after 7 days. Moreover, the nanoparticles were incubated with 40 mM glutathione at 80 ºC for 2 months and electron microscopic analysis revealed greater destruction of nanoparticles with higher concentration of MPDMS and complete collapse of MPDMS nanoparticles, whereas MPTS nanoparticles retained their spherical shape. These results were related to the susceptibility of MPDMS and MPTS-MPDMS nanoparticles to the attack by glutathione and the degree of degradability was related to the content of disulfide bonds [39].

Modification with polymers:

Thiolated silica nanoparticles prepared from MPTS were modified with polyethylene glycol (PEG), poly(2-alkyl-2-oxazoline) (POZ), poly(N-isopropyl acrylamide) (PNIPAM) and hydroxyethylcellulose (HEC) [11,15,16,18,40–42]. Irmukhametova et al studied the retention of fluorescently labelled PEGylated thiolated silica nanoparticles prepared from MPTS on the surface of bovine corneal tissue using fluorescence microscopy. They used wash-off method with artificial tear fluid and fluorescent microphotographs were taken after each wash cycle. The PEGylated nanoparticles were removed from corneal surface very rapidly and disappeared completely after the third wash cycle. The reduction in mucoadhesive properties was related to the reduction of exposed thiol groups on the surface of the nanoparticle to bind to mucin on the surface of the ocular tissue [11]. Mun et al. reported the use of fluorescently labelled nanoparticles, PEGylated with PEG 750 and 5000 Da and studied their penetration through de-epithelialized ocular tissue using fluorescent microscope. Thiolated and PEGylated 750 Da remained bound the ocular surface while PEGylated 5000 Da nanoparticles started permeating gradually to the stroma after 1 hour of application [18]. Later, they studied the retention of fluorescently labelled PEGylated 750 and 5000 Da on the mucosal surface of porcine urinary bladder using the wash-off method with artificial urine solution and used chitosan and dextran as positive and negative controls, respectively. PEGylated 750 Da nanoparticles were completely removed after 6 wash cycles and PEG 5000 Da were removed after 5 wash cycles similarly to the negative control [16]. Mansfield et al. prepared PEGylated 5000 Da and POZylated 5000 Da thiolated silica nanoparticles and used nanoparticle tracking analysis to determine their diffusion coefficient through 1% w/v gastric mucus and reported higher diffusion coefficient values for POZylated nanoparticles. In addition, they studied the penetration of fluorescently labelled PEGylated and POZylated nanoparticles into porcine stomach mucosa using fluorescence microscopy. Both PEGylated and POZylated nanoparticles showed enhanced penetration into the gastric mucosa compared to unmodified nanoparticles due to the stealth character of the polymers which prevents their interaction with the mucous gel [41]. Later, they used the same method to compare the penetration of POZylated thiolated silica nanoparticles with variation of the alkyl chain length. The nanoparticles were functionalised with poly(2-methyl-2-oxazoline) (PMOZ), poly(2-ethyl-2-oxazoline) (PEOZ), and poly(2-n-propyl-2-oxazoline) (PNPOZ). They reported a higher diffusion coefficient values and deeper penetration into the porcine gastric mucosa of particles grafted with short chain length POZ (PMOZ) which decreases with the increase in chain length. This was related to the stealth effect and the hydration of the polymer as hydrophobic molecules are poorly penetrating through mucosal barriers [19]. Ways et al. studied the retention of fluorescently labelled PEGylated 5000 Da and POZylated 5000 Da thiolated silica nanoparticles on the surface of rat intestinal mucosa using a wash-off method with phosphate buffer pH 6.8 and compared them to chitosan and dextran. The wash-off profile for both was similar to dextran which indicated poor retention [15].

Mansfield et al. functionalised thiolated silica nanoparticles in a “one pot” reaction with variable concentrations of HEC (0.1, 0.5, 1, 2% w/v). Characterisation of the nanoparticles for size and surface functionality revealed an increase in nanoparticle size and reduction in the number of thiol groups with increasing concentration of HEC. Size measurements obtained from dynamic light scattering (DLS) were compared with size generated from small angle neutron scattering (SANS) and transmission electron microscopy (TEM) and revealed the formation clusters of nanoparticles. As the concentration of HEC was increased, the number of aggregating nanoparticles increased. They were able to identify a correlation between the aggregate size and number of nanoparticles per aggregate based on the discrepancy in size measurements obtained from DLS and SANS which can be used to control the size of aggregate during synthesis [42].

Isomeric temperature-responsive polymers, poly(N-isopropyl acrylamide) (PNIPAM), and poly(2-n-propyl-2-oxazoline) (PNPOZ) with similar molecular weights (5000 Da) and grafting density were used to graft onto thiolated silica nanoparticles. Temperature induced aggregation of these nanoparticles with polymer lower critical solution temperature behaviour were explored. The aggregation mechanism of polymer grafted nanoparticles was studied using dynamic light scattering and small-angle neutron scattering. It was reported that the aggregation temperature of the nanoparticles grafted with PNPOZ and PNIPAM were different but were consistent with the lower critical solution temperatures of the polymers. However, both nanoparticles showed similar aggregation mechanism which starts by the formation of small aggregates which interacts with each other as temperature increase resulting in full aggregation and phase separation [43].

Mucoadhesion

Mucoadhesion is the attachment or adherence of a material to a mucosal membrane in the human body resulting in temporary retention. Examples of mucosal membranes include gastric, nasal, ocular and vaginal [44,45]. Mucosal membranes are composed of epithelial cells coated with a hydrated viscoelastic gel layer of mucus which is composed of membrane bound and soluble mucins. Soluble mucins are high-molecular-weight glycoproteins with intramolecular cystein-cystein disulfide bridges [44]. Thiolated materials were extensively exploited for the development of mucoadhesive excipients for oral, nasal, ocular, and intravesical drug delivery [11,15,16,18,23,24,27,46–48]. They were reported to form disulfide bonds with mucin in the mucosal layer resulting in the improvement in the mucoadhesion.

Irmukhametova et al. studied the mucoadhesion of fluorescently labelled thiolated silica nanoparticles, prepared using MPTS, to bovine ocular surfaces using fluorescence microscopy. The nanoparticles were left for 3 minutes after application, then washed off using artificial tear fluid and fluorescence microphotographs were taken after each wash cycle. They reported that these nanoparticles exhibited excellent mucoadhesive properties as they were retained on corneal surface even after 5 wash cycles [11]. Later, these nanoparticles were also reported to stay bound to the surface of de-epithelialized ocular tissue [18]. Moreover, the retention of thiolated silica nanoparticles with different sizes prepared in different aprotic solvents to the mucosal surface of porcine urinary bladder was studied using a wash-off method with artificial urine fluid and compared to chitosan and dextran as positive and negative control, respectively. Solvents used for the synthesis of thiolated nanoparticles were dimethyl sulfoxide (DMSO), dimethyl formamide (DMF) and acetonitrile (AcN) and the size and thiol content of the resulting nanoparticles were determined using dynamic light scattering and Ellman's assay, respectively. Nanoparticles prepared in DMSO (SH, 118 µmol/g) had greater retention than those from DMF (SH, 119 µmol/g) whilst those prepared in AcN (SH, 40 µmol/g) had the poorest retention. Nanoparticles with higher thiol content had greater retention, however, the thiol content of nanoparticles prepared in DMSO and DMF were similar but better retention was related to the smaller size of nanoparticles prepared in DMSO (21 nm) than those prepared in DMF (95 nm). Moreover, two sets of nanoparticles were prepared in DMSO, one was 21 nm with thiol content of 118 µmol/g and the other was 45 nm with thiol content 249 µmol/g. Their retention on porcine urinary bladder was compared and nanoparticles with higher thiol content had better retention though they were larger [16]. Thiolated nanoparticles were also reported to exhibit mucoadhesivness to the rat intestinal mucosa using the same wash-off method with phosphate buffer pH 6.8 [15].

Nitric oxide conjugation

Nitric oxide (NO) is a free radical released by immune cells in response to infections and NO donor molecules such as sodium nitrite, diazeniumdiolates, and S-Nitrosothiols (RSNO) group exhibit broad spectrum antimicrobial activity [8]. The main mechanism of antimicrobial action is by chemical alteration of DNA by reactive nitrogen oxide species (RNOS) and can occur by three mechanisms: direct reaction of RNOS with DNA structure, inhibition of its repair and increased generation of the genotoxic alkylating agents and hydrogen peroxide [49].

Chang et al. prepared nitric oxide-releasing thiolated silica nanoparticles using the Stöber method. They optimised the synthesis conditions to produce spherical, monodisperse nanoparticles with size < 1 µm as scaffolds for RSNO donors that store and release NO in proportional to the molar percentage of MPTS used in the synthesis. They reported NO releasing time from the nanoparticles exceeded 48 h under physiological condition and in the absence of light [50].

Cell-penetration studies

Mesoporous silica nanoparticles-based drug delivery system have been designed to deliver drugs into the target site and to improve their accumulation at tumour sites when the nanocarrier surface is functionalised with targeting ligand such as cell penetrating peptides, peptides, antibodies and folate [51,52]. Li et al. synthesized thiol functionalised mesoporous nanoparticles and Arg-Gly-Asp (RGD) peptide was linked to the nanoparticles by disulfide bonds then doxorubicin was loaded on the nanoparticles to form DOX@MSN-S-S-RGD drug delivery system. RGD enhanced tumour cell uptake of the delivery system and doxorubicin was released in a burst mode by intercellular glutathione breaking the disulfide bonds [51]. Xiao et al. prepared pH and redox-responsive tumour triggered targeted mesoporous silica nanoparticles (TTTMSN) as the pH varies from the blood (7.4), tumour extracellular environment (<6.8) and in endosomes and lysosomes (5-5.5). The mesoporous silica nanoparticles were functionalised with thiol groups then modified with azide terminated tumour-targeting peptide RGDFFFFC as a potential gatekeeper via disulfide linkages. The nanoparticles were loaded with doxorubicin then PEGylated with alkynyl modified MPEG with a benzoic-imine bond. When the nanoparticles reached the tumour site, the MPEG benzoic-imine bonds were hydrolysed at the acidic extracellular environment of the tumour and PEG chains were removed. The RGD ligand facilitated the internalization of the nanoparticles by the tumour cells and removal of the ligand and cleavage of disulfide bonds was facilitated by glutathione released by the tumour cell and the loaded doxorubicin was subsequently released. The nanoparticles were tested on U-87 cells using MTT assay which revealed reduction in cell viability up to 60% at pH 7.4 and was further reduced to 20% at pH 5 [52].

Kim et al. used cyclodextrin as a gatekeeper for the pores of mesoporous silica nanoparticles by connecting it to the surface of the nanoparticles via disulfide bonds. First the nanoparticles were functionalised with thiol group using MPTS (Si-SH) and the disulfide linker was introduced by reacting it with S -(2-aminoethylthio)-2-thiopyridine hydrochloride to produce (Si-SS-NH_2), which is reacted with propargyl bromide to yield (Si-SS-alkyne). Doxorubicin was loaded before introducing the gatekeeper cyclodextrin by click coupling of mono-6-azido- β -CD with Si-SS-alkyne to produce (Si-SS-CD), which was PEGylated to improve the solubility. A549 cells were incubated with the nanoparticles with a high concentration of glutathione and cells without glutathione and were observed using confocal laser scanning microscopy and release of doxorubicin was observed in cells with glutathione only. The survival of the cells was investigated using different concentrations of doxorubicin and revealed the reduction in cell survival with increasing dose [53].

Zhou et al. used fluorescently labelled mesoporous silica glyconanoparticles as a drug carrier, functionalised with D-mannose and incorporated a redox-sensitive disulfide moiety as a linker. Doxorubicin was then loaded in particle pores and the nanoparticles were capped with concanavalin A (Con A). The gatekeeper Con A blocked the reduction of disulfide bonds at low levels of glutathione in normal cells, whereas, at higher concentrations in cancer cells the disulfide bond was reduced, Con A was uncapped and doxorubicin was released successfully [33].

Gayam et al. synthesized mesoporous silica nanoparticles and functionalised with thiol using MPTS then further modified using S-(2-aminoethylthio)-2-thiopyridine hydrochloride to achieve nanoparticles containing disulfide bonds and with amino-terminated alkyl chains (MSNP-SS-NH_2). The nanoparticles were further modified by alkyl containing pyridine to construct azide terminated stalk (MSNP-SS-N_3) which is encircled by the macrocycle Pd-tridentate ligand, after loading with doxorubicin, to form a rotaxane nanovalve then functionalised with folic acid (MSNP-SS-FA). In these nanoparticles, the folic acid head group facilitated the uptake of the nanoparticles by cancer cells specifically and rotaxane valves lock the cargo doxorubicin molecules inside the mesopores. The valve is opened, and cargo is released inside the cancer cell after cleavage of the disulfide bonds by glutathione. The nanoparticles were tested on HeLa cells using MTT cell viability assay and confocal laser scanning microscopy, and high level of apoptosis was reported in the drug loaded nanoparticles group compared to drug free nanoparticles group which suggested the safety, specifity and efficacy of the delivery method [54].

Imaging and diagnostics

Thiol functionalised mesoporous silica was conjugated with radioisotopes of arsenic for image-guided drug delivery studies of the arsenic-based chemotherapeutic arsenic trioxide (ATO) with positron emission tomography (PET), a non-invasive quantitative imaging modality. Arsenic loading capacity on the nanoparticles was 20mg of ATO per gram of mesoporous silica nanoparticles, which are sufficient to deliver chemotherapeutic quantities of the drug. Stability toward dearsynylation was reported from PET imaging of *in vivo* murine biodistribution of radiolabelled silica nanoparticles. The results obtained show potential for the use of thiol functionalised silica nanoparticles for image-guided drug delivery of ATO-based chemotherapeutics [55]. Baeckmann et al. used a multistep synthesis of functional MCM-48-type mesoporous silica nanoparticles and used APTS and MPTS for amine and thiol functionalisation. The nanoparticles were then functionalised with PEG and/or with diethylenetriaminepentaacetic acid chelates (DTPA), a pro-chelate ligand used as a magnetic resonance imaging contrast agent, and/or loaded with quercetin and/or grafted with an organic dye (rhodamine). They reported the existence of unreacted surface group though already functionalised with PEG and DTPA and the possibility of using the system as a multi-imaging (MRI and fluorescence) platform [56].

Kalantari et al. prepared thiolated dendritic mesoporous silica nanoparticles (T-DMSNs) with high thiol contents and loaded with gold nanoparticles for the preparation of nanozymes (T-DMSNs-Au) for future diagnostic applications. They reported high loading of gold nanoparticles (34%) with size range 1.2- 2.7 nm. The peroxidase-like activity of T-DMSNs-Au was evaluated and was found to be dependent on the gold nanoparticles size with the highest activity reported for 1.9 nm particles [57].

Toxicology

Thiolated silica was used for coating iron oxide nanoparticles and the cytotoxic effects were evaluated using human lung epithelial cells A549. It was reported that the exposure of these nanoparticles reduced the size of focal adhesions of the cells and caused disruption of the actin microfilaments and microtubule cytoskeleton. Additionally, the phosphorylation of focal adhesion kinase (FAK), extracellular-signal-regulated kinase (ERK), p38, and cell adhesion were significantly affected [58].

Mun et al. used the slug mucosal irritation test to evaluate the mucosal irritation of thiolated and PEGylated nanoparticles and compared them to benzalkonium chloride and phosphate buffer saline as positive and negative control, respectively [59]. This method was developed by Adriaens and Remon for screening toxicity of materials on mucosal surfaces. Slugs have mucus secreting cells on their foot which secretes two types of mucus, thin and watery and thick and sticky. Thick mucus is produced when an irritating compound is applied to slugs. The assay is based on measuring the weight loss and mucus production which correlates to level of toxicity [60]. As Mun et al. were testing the nanoparticles on eyes, they used a classification model based on mucus production with the following ranges: ≤3 (non-irritant), >3≤6 (irritating to eyes) and >6 (risk of serious damage to eyes). When positive and negative control was applied to slugs, mucus production was 19.3 (irritant) and 1.8% (non-irritant), respectively. Thiolated silica nanoparticles (0.1% w/v in PBS) produced 1.4% of mucus thus were determined as non-irritant. In addition, PEGylated 750 and 500 Da (0.1% w/v in PBS) were applied and mucus production was 1.3 and 1.2 respectively and were determined as non-irritant [59].

Eye structure and barriers:

The eye is specialised organ that captures visual information and transmits it to the visual cortex of the brain via the optic nerve for processing. The eyeball is accommodated within the orbit surrounded with adipose tissue that support it in the orbital cavity and consists of three different layers enclosing different anatomical structures (Figure 2) [61,62].

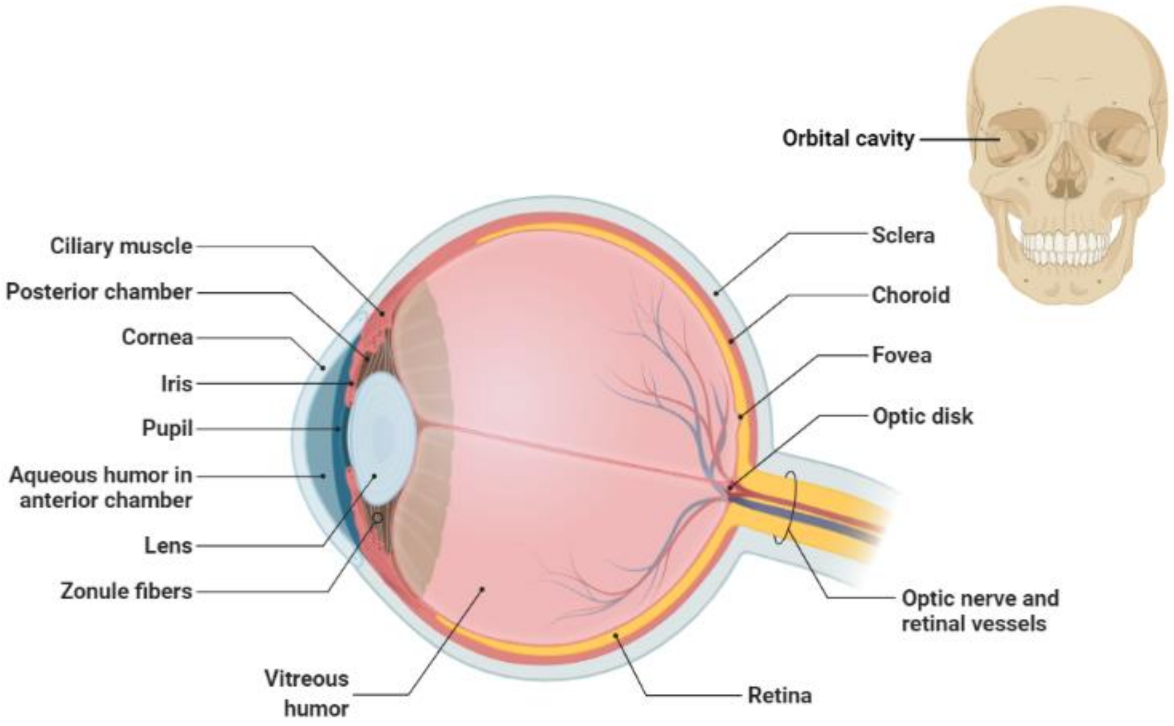

Figure 2: General anatomy of the eye presented as a cross section image.

The first layer is *Tunica Fibrosa Oculi* which is the outermost layer which maintains the spherical shape of the eyeball and consists of the cornea, sclera, and conjunctiva. The cornea is a transparent, multilayer, avascular layer and the average central thickness is ~540 µm which gets thicker towards the periphery. This multilayer keratinised structure acts as a barrier as it is relatively impermeable to both hydrophilic and hydrophobic drug molecules. This property is related to the outermost two to three layers of the corneal squamous epithelial cells and damaging this layer affects the permeability of this barrier. The cornea is covered with a protective tear film which consists of three layers, the outermost lipid layer followed by middle aqueous layer then mucous layer. The lipid lubricates the lid margins and is secreted from meibomian gland, whereas lacrimal glands produce the free lipid and soluble mucin within the aqueous layer and goblet cells secrete the mucous in the mucous layer. The tear is drained through the nasolacrimal duct to the nasal cavity. The tear film acts as a barrier by interacting with drugs applied externally which results in refractive changes and causes blinking and excessive lacrimation. This movement spreads the tear film across the cornea and pushes it to the nasolacrimal duct to be drained to the nasal cavity. The conjunctiva is another protective layer and contains two or more layers of isoperimetric to highly prismatic epithelial cells. The palpebral conjunctiva is vascular and covers the posterior surface of the upper and lower lids. The bulbar conjunctiva is avascular and consists of stratified non-keratinised epithelial cells. It is slightly mobile and starts from the upper and lower fornices (conjunctival sac) and lies over the sclera up to the cornea region. The lower conjunctival sac can contain a drug droplet of up to 25 µL when the lower eyelid is pulled down and when it returns to its normal position the capacity will decrease to less than 10 µL. The sclera is the outer layer of the eye globe and is covered by a loose connective tissue layer called episcleral. It lies up to the corneal limbus anteriorly and to the optic nerve posteriorly. It is avascular and consists of collagen, glycoproteins, elastin and proteoglycans [61–64].

The second layer is the anterior chamber of the eye which is the space between the cornea’s endothelium and the anterior surface of the iris and filled with aqueous humour which is an optically clear fluid. The aqueous humour maintains the intraocular pressure, provides nutrients and oxygen to the cornea and lens, and removes metabolic waste. The iris is part of the uveal tract and separates the anterior and posterior chambers and controls the intensity of light transmitting into the eye. The ciliary body lies behind the iris and produces the aqueous humour, uveoscleral outflow and hyaluronate and plays an important role in maintaining the blood-aqueous barrier. The vitreous body is the third chamber and located between the lens and the retina. It is a gel-like substance composed mainly of water (>98%) and other components such as, collagen fibres, hyaluronic acid, and proteins. As the vitreous body is avascular, molecular movement is mainly driven by diffusion [61,62].

The third layer is the choroid which is a vascularised layer around the sclera (between the sclera and the retina) and includes the iris and ciliary body. It provides oxygen and nutrients to the retina, ciliary body, and iris. Membranes within this vascular layer maintain the clarity of the light transmitting pathways by preventing the passage compromising substance. Close to the choroid lies the retina which is ~0.5 mm thick multilayer structure lining the posterior inner surface of the eye extending towards the ciliary body. It is composed of highly specialised nerve tissue continuous to the optic nerve and links to the visual cortex in the brain. When light falls upon the retina, it converts it to visual signals which are interpreted by the brain as images. The retinal pigmented epithelium and blood-retina barrier regulate solute movement to the retina and into the body of the eye. In addition, nutrients and metabolic maintenance of the retina are regulated by retinal pigmented epithelium. The inner surface of the retina is covered with the internal limiting membrane which forms a selective permeation barrier between the intercellular space of the retina and the vitreous [61–63].

Ocular drug delivery systems

Delivering drugs to the eye is challenging due to the complicated anatomy of the eye and multiple barriers present. The blood retinal barrier is a two-sided barrier (inner and outer) which is maintained by tight junctions that keeps the eye resistant to exposure to foreign substances including drugs. However, multiple entry routes are present in the eye that can be used to deliver drugs to the anterior segment and posterior segment of the eye. Topical and subconjunctival injections can be used to deliver drugs to the anterior segment whereas, topical, systemic, intraocular injection (intravitreal) are used to deliver drugs to the posterior segment [65,66]. Figure 3 presents different routes of drug administration and barriers to drug delivery [66].

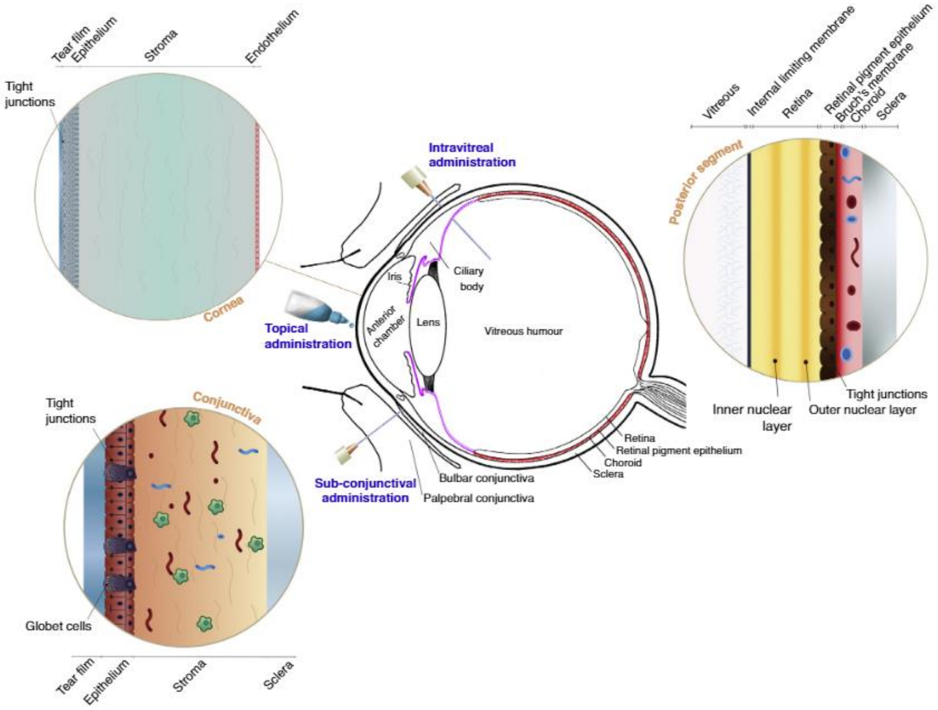

Figure 3: Cross-section of the eye and routes of drug administration (topical, subconjunctival, and intravitreal). The barriers for drug penetration after topical, subconjunctival and intravitreal delivery are shown in the zoomed pictures [66].

Delivery to the anterior segment

Topical application

Eye drops are one of the most used formulations to deliver drugs to the anterior segment of the eye as it is convenient, with high patient compliance and is a non-invasive mode of administration. However, only 20% of the administered dose is retained after topical application and the rest is lost due to blinking [67]. After topical application of a drug, the corneal epithelium is the major barrier to absorption, however, after crossing this barrier it can diffuse freely in the corneal stroma and endothelium to the aqueous humour then to the trabecular meshwork, iris, and ciliary body. Diffusion to the vitreous humour and the retina is restricted by the lenticular barrier, iris-ciliary body blood flow and aqueous humour turnover. Aqueous humour outflow can eliminate both small and large molecules at flow rates 5-35 mL/min and 2.4-5.2 mL/min respectively, whereas blood flow of the iris and ciliary body can eliminate only small molecules. Moreover, the conjunctiva and the sclera are another route of drug absorption to the iris and/or ciliary body directly escaping the aqueous humour which can be used for the absorption of hydrophilic small molecules and large molecules as well. Although compounds with molecular weight up to 5 kDa can permeate through the conjunctiva and macromolecules of 100 kDa can pass through the sclera, only small drug molecules are used clinically for topical application [66,68].

Conventional topical ocular drug delivery systems include eye drop solutions, suspensions, emulsions, and ointments. Topical eye drop instillation provides a pulse drug concentration followed by rapid decline in concentration. Additives such as, viscosity and penetration enhancers are added in attempts to improve the contact time, bioavailability, and corneal uptake. Examples of viscosity and penetration enhancers include hydroxymethyl cellulose and benzalkonium chloride, respectively. However, significant precorneal loss is still reported even with the addition of viscosity enhancers [67,69]. Moreover, bioavailability was reported to improve with addition of penetration enhancers, but more toxicological research is required for those which are not in clinical use [62,67].

Emulsions improve solubility and bioavailability, of drugs by improving precorneal residence time and corneal penetration, and can be water in oil (w/o) or oil in water (o/w) with preference to o/w for ocular drug delivery [67]. Tajika et al. evaluated ocular distribution and excretion of tritium-labelled difluprednate ((3)H-DFBA) ophthalmic emulsion 0.05% after a single or repeated instillation to pigmented rabbit eyes. They were able to detect difluprednate in the anterior and posterior segments of the eye after single and multiple topical drug instillation. Highest to lowest concentration of radioactivity was in the cornea, iris-ciliary body, retina-choroid, conjunctiva, sclera, aqueous humour, lens, and vitreous humour, respectively. The highest radioactive concentration, after a single application, in the ocular tissue was reached in 0.5 h and in the periocular tissue in 1 h. The detection of the drug in the anterior and posterior segments shortly after topical application suggests the potential use of this formulation for the treatment of inflammation in these areas [70].

Suspensions are dispersions of finely divided drug in (usually for the eye) aqueous solvent containing a suspending agent. The retention of suspension particles in the precorneal pocket results in longer contact time and longer duration of action in comparison to drug solutions. Duration of action is size dependent with larger particles retained for longer time with slow drug dissolution. However, increasing the particles size may cause irritation of the eye [69]. TobraDex® suspension is a combination of tobramycin (antibiotic) and dexamethasone (steroid) which is widely used; however, high viscosity is a disadvantage of this product. In attempts to improve the product TobraDex ST® suspension has very low settling (3%) over 24 hours with better quality, kinetics and tissue permeation [67]. Scoper et al. compared the pharmacokinetics and tissue permeability of TobraDex® and TobraDex ST® suspensions using a rabbit eye model and a clinical study with cataract patients. They reported higher concentration of tobramycin and dexamethasone with 8.3-fold increase of tobramycin in rabbit tear film and 12.5-fold increase in ocular tissue post dose of TobraDex ST® compared to TobraDex®. The *in vitro* bactericidal activity revealed greater activity of TobraDex ST® against *Staphylococcus aureus* and *Pseudomonas aeruginosa*. In addition, human clinical study revealed greater dexamethasone concentration at 1 hour in the aqueous humour for patients who received TobraDex ST® suggesting it as a better option for treatment of eye infection and inflammation [71].

Ointments are mixtures of biocompatible semisolid and a solid hydrocarbon with melting points at the physiological temperature of the eye (34 ºC) [67]. Ointments provide prolonged contact time as are not prone to tear dilution, thus, improve bioavailability and result in sustained drug release. However, application of ointments causes blurred vision which limits the time of application and may affect patient compliance [67,69].

Generally, the above topical formulations are widely used for anterior segment treatment, however, irritation, redness of the eye and blurred vision are examples of side effects that they can cause. Research is being carried to develop long-acting formulations with improved efficacy and fewer side effects for anterior segment treatments [66,67].

Subconjunctival injections:

In addition to topical formulations, subconjunctival injections are used to deliver drugs such as local anaesthetics and anti-inflammatory drugs to the anterior segment [65,66]. The injections are placed between the bulbar conjunctiva and sclera resulting in delivering the drug directly from the sclera to the iris and ciliary body without distributing to the aqueous humour. Very small amount can reach the retina and choroid due to loss at injection site, retinal barriers and clearance by choroidal blood flow leaving it as an option for anterior segment delivery only [66].

Delivery to the posterior segment

To deliver drugs to the posterior segment i.e., retina and choroid, intraocular (intravitreal) injections are used. Diffusion in the vitreous takes place post injection then the drug is cleared via anterior and posterior routes. When the drug diffuses from the vitreous to the aqueous humour it results in anterior elimination, however, this route is limited by iris-ciliary body and the lens resulting in long half-life (days). In order to eliminate the drug posteriorly, it has to permeate across the blood ocular barriers in the retina and iris-ciliary body with limitation in permeation of large molecules and faster permeation of small molecules [66]. In addition, the inner limiting membrane is another barrier that limits the retinal penetration of nanoparticles and large molecules. For example, large molecules like Anti-VEGF biologics poorly permeate across the blood-retinal barrier resulting in anterior elimination of ~90% of the dose and half-lives in the range of a week although they are administered every 1-2 months. On the other hand, small molecules that can cross the blood-retinal barrier have short half-lives (2-10 hours) in the vitreous humour resulting in the need for more frequent injections unless slow-release formulations are used. Dosing interval is an important factor and crucial issue for intravitreal injections and more effective, long acting drugs are needed [66].

Nanosystems for ocular drug delivery

Nonosystems such as, nanoparticles, nanomicelles, niosomes and liposomes are developed for ocular drug delivery as they have advantages over conventional formulations including better permeability and bioavailability, longer duration of action and targeted drug delivery [67,72–74]. It was reported that polymeric nanoparticles and niosomes permeated to the aqueous humour, liposomes, nanomicelles, polymeric micelles, PEGylated, and solid lipid nanoparticles permeated to the retina and dendrimers permeated to the choroid [74,75].

Nanoparticles intended for ocular drug delivery are usually composed of proteins, lipids, and polymers such as, albumin, chitosan, poly (lactide-co-glycolide) (PLGA), and polylactic acid (PLA). Nanosphere and nanocapsules are drug loaded nanoparticles where the drug is within a spherical polymeric shell to form nanosphere, and when the drug is distributed in polymeric matrix uniformly it is called nanocapsule. Due to their small size, they offer a sustained release property and can cause less irritation. However, they are also prone to rapid elimination from the precorneal pocket and to increase residence time mucoadhesive materials such as chitosan have been employed. Size and surface charge of the nanoparticles was reported to influence site of delivery to the eye. Cationic nanoparticles were reported to be attracted by the cornea and conjunctiva after topical application due to electrostatic interactions [75–77]. In addition, nanoparticles sized less than 200 nm were taken up in the cornea and the conjunctiva [75,78,79]. Hydrophilic nanoparticles with size range of 20-80 nm were reported to pass the sclera pores [75,80,81] whereas nanoparticles smaller than 250 nm were reported to be taken up by the retinal cells via endocytosis [75,82] and particles up to 350 nm were reported to reach the retina when injected intravitreally [75,83]. Moreover, cationic nanoparticles were reported to be trapped whereas anionic nanoparticles diffused after injecting to the vitreous humour [78,80,83–85]. Bhatta et al. prepared natamycin encapsulated lecithin/ chitosan nanoparticles for prolonged ocular drug release. The resulting nanoparticles were around 213 nm with zeta potential value of +43 mV and in vitro drug release revealed a biphasic profile with a burst release followed by slow release. They also compared the minimum inhibition concentration 90 (MIC90) of the nanoparticles with a marketed suspension and free natamycin against *Candida albicans* and *Aspergillus fumigates* and reported a similar antifungal activity. When evaluated on rabbits, the nanoparticles exhibited significant adhesion to mucin resulting in 1.74 fold increase in ($AUC_{0-\infty}$) and 7.4-fold reduction in clearance in comparison to the marketed suspension [86]. Zhang et al. loaded poly(lactic acid–*co*-glycolic acid) nanoparticles with dexamethasone and studied their tolerance and pharmacokinetics after intravitreal injection to rabbits in comparison to conventional dexamethasone. The resulting nanoparticles diameter was 232 ± 5 nm and dexamethasone encapsulation efficacy was 56%. They reported a sustained release of dexamethasone for around 50 days with relatively constant levels for over 30 days with no abnormalities reported even after 50 days. The bioavailability of dexamethasone nanoparticles was significantly higher than conventional dexamethasone [87]. Research on the use of mesoporous silica nanoparticles for ocular drug delivery is ongoing. Qu and co-workers conjugated epithelial cell adhesion molecule (EpCAM), a transmembrane protein, to mesoporous silica nanoparticles loaded with carboplatin, an anticancer drug used for the treatment of retinoblastoma. They reported the formation of spherical nanoparticles with controlled release kinetics. A cell uptake assay was performed on human retinoblastoma cell (Y79) and revealed enhanced internalisation of the conjugated nanoparticles in comparison to the nonconjugated nanoparticles (nontargeted). Caspase-3 protein analysis revealed 2-fold increase in caspase-3 level in cells treated with conjugated nanoparticles compared to free carboplatin indicating higher rate of apoptosis [88]. Liao et al. prepared gelatine functionalised pilocarpine loaded mesoporous silica nanoparticles and injected intracamerally to the anterior chamber of the eyes of glaucoma experimental model rabbits. A long-lasting release profile up to 36 days with high release percentage (50%) was demonstrated *in vitro*, whereas *in vivo* studies reported the maintenance of intraocular pressure for 21 days [89]. Sun et al. prepared mesoporous silica nanoparticles encapsulated bevacizumab (anti-angiogenic agent) delivery system. Subconjunctival injection was administered to mouse models with alkaline burn-induced corneal neovascularization and intravitreal injection used mouse models with oxygen-induced retinopathy. The residence time of the bevacizumab nanosystem in the vitreous humour was prolonged from 5 to 13 days after injection with long-lasting release reaching up to 28 days. In addition, the efficacy of bevacizumab was improved, and the inhibition of corneal neovascularization was significantly enhanced in comparison to free drug especially 14 days post injection. Moreover, the area of retinal neovascularization was significantly reduced in comparison to free drug [90]. The toxicity of silica nanoparticles on ocular surface cells was investigated by Park and co-workers. They used human corneal epithelial cells (HCECs) cell lines to evaluate the cytotoxicity of variable concentrations (up to 100 µg/mL) of silica nanoparticles sized 50, 100, 150 nm. The nanoparticles were left up to 48 hours in the cultured HCECs and were up taken by the cells inside the cytoplasmic vacuoles. Although there was mild elevation in the generation of cellular reactive species which was dose dependent, there was no significant decrease in cell viability of all sizes even at high concentration. Thus, no significant cytotoxicity in cultured HCECs was reported for all tested silica nanoparticles [91].

Nanomicelles are self-assembled amphoteric copolymers that form core-shell nanocarriers in the size range of 10-100 nm which encapsulate hydrophobic drugs to protect them from degradation. Micelles were initially composed of polyoxyethylene– polyoxypropylene (POE/POP) block copolymers. Later, poly-lactic acid (PLA), Pluronic, N-isopropylacrylamide (NIPAAM), vinylpyrrolidone (VP), acrylic acid (AA), polyhydroxyethylaspartamide (PHEA-C16) and N0 -methylene bis-acrylamide (MBA), were used to prepare micelles and their ability to enhance corneal permeation was evaluated [74,77]. Polymeric nanomicelles composed of α-lipoic acid in Solplus® were prepared for the treatment of diabetes-associated corneal disease and compared to commercial eye drops. The solubility of α-lipoic acid was enhanced by 10-fold and the corneal residence time was also enhanced [92]. Polyvinyl caprolactam–polyvinyl acetate–polyethylene glycol graft copolymer was used to prepare curcumin loaded micelles for the treatment of ocular inflammation. The solubility and chemical stability of curcumin was improved, and *in vitro* cellular uptake of curcumin loaded micelles was greater in comparison to free curcumin. In addition, *in vivo* studies were performed in rabbits and mice and revealed enhanced corneal uptake and improved anti-inflammatory efficacy in animals treated with the micelles formulation compared to free curcumin [93]. It was reported that the amphiphilic copolymers have the ability to disturb cell membrane resulting in enhanced drug permeability through transcellular and/or paracellular pathways [94].

Liposomes are vesicles composed of an aqueous core surrounded by a lipid bilayer [80]. They are biocompatible, biodegradable and can incorporate hydrophilic and hydrophobic in a single system and have been investigated for prolonged drug release and targeted drug delivery [74]. Visudyne is a liposomal formulation of verteporfin, a hydrophobic photosensitizer, which is used for photodynamic therapy for the treatment of choroidal neovascularization and is the only ocular liposomal drug approved by FDA. The conventional formulation undergoes self-aggregation in aqueous media limiting its bioavailability in biological system and this was resolved by developing the liposomal formulation. The drug is injected intravenously followed by photodynamic therapy resulting in selective uptake of this photosensitive dye and selective closure of choroidal neovascularization vessels by thrombosis after its activation by a specific laser [80,95]. Liposomal formulation of bevacizumab was injected intravitreally to rabbits and compared to free drug. The concentration of bevacizumab in the vitreous humour from the liposomal formulation was five-times higher at 42 days with sustained release for at least 6 weeks [96].

Skin structure and barriers

The skin is the largest organ in the body that forms a barrier between the body and the environment and provides protection from chemicals and microorganisms and regulates body temperature and water loss. It is composed of three main layers: epidermis, dermis, and hypodermis (Figure 4). The hypodermis or subcutaneous fat layer is the layer that connects the skin to the underlaying muscles and provides support for the skin. It contains blood vessels and nerves and is not considered as an important barrier for topical and transdermal drug delivery as it is just below the dermis which is rich in blood supply [97,98].

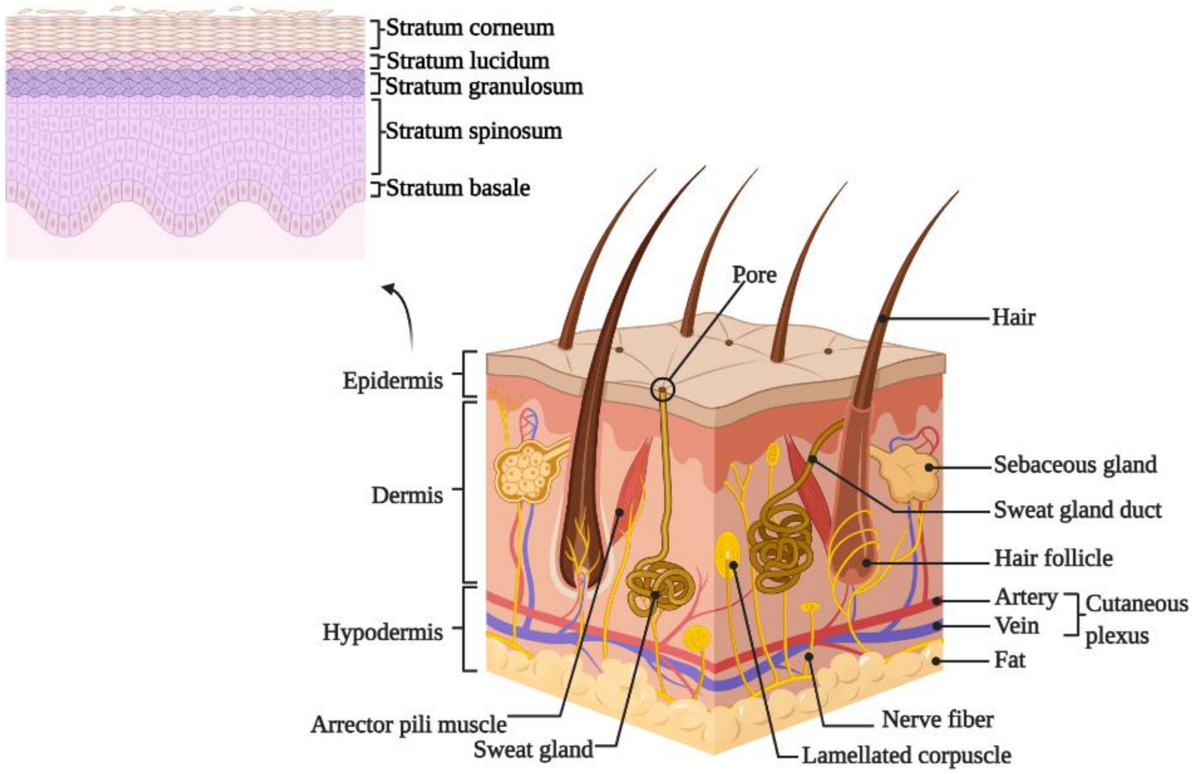

Figure 4: Structure of the human skin and epidermal layers.

The dermis is 3-5 mm thick layer above the hypodermis that forms the main component of the human skin and is composed of papillary and reticular layers. The reticular layer is in the lower dermis and is composed of densely packed collagen and elastin fibres in an amorphous gel-like matrix that contains glycoproteins, hyaluronan and water. This layer supports the blood vessels, nerve endings, pilosebaceous units and sweat glands. Above this layer is the papillary layer which contains loosely arranged collagen fibres and terminal capillary networks. This layer increases the surface area between the dermis and epidermis, thus, enhances the exchange of oxygen, nutrients, and waste between them. In addition, this enhances the removal of permeants from the dermal-epidermal boundary which promotes transdermal drug delivery polar. The rich vascular network in the dermis plays an important role in regulating body temperature, oxygen and nutrients supply, and waste removal. Moreover, drug molecules can be removed which maintains a driving force for diffusion. In addition to the vascular network, the lymphatic system is within the dermal-epidermal boundary which facilitates immunological response, regulates interstitial pressure and waste removal. Permeated drug molecules are also removed via lymphatic vessels. The pilosebaceous units (hair follicles and sebaceous glands), eccrine and apocrine glands are appendages found on the surface of the skin that originated in the dermis. These appendages are also called shunt routes as drug molecules could avoid the stratum corneum and enter to the lower layers of the skin through them.

The pilosebaceous unit is comprised of the hair shaft, hair follicle, sebaceous gland and arrector pili muscle. The hair structure can be divided into hair shaft and hair follicle. The hair shaft is composed of medulla enveloped by a cortex then a cuticle. The root sheath is multi-layered with a keratinised outer root that continues with the epidermis which is of importance for drug diffusion and delivery. The outer part of the hair follicle is the infundibulum which extends from the skin surface to the sebaceous duct in which the hair shaft moves freely. The thickness of the stratum corneum decreases in deeper infundibulum resulting in a reduced barrier to drug diffusion. In addition, sebaceous glands are associated with hair follicles which release lipids through holocrine secretion. Eccrine glands are coiled glands located in the lower dermis found over most of the body surface and are 500-700 µm in diameter. Sweat, which is a dilute salt solution, is secreted by eccrine gland and is stimulated by exercise, emotional stress and hight environmental temperature. Apocrine glands are found in specific areas of the skin and the gland coil size is similar to the eccrine gland. However, apocrine glands provide lipoidal and milk protein nutrients at the upper region of the hair follicle for skin bacteria [97,98]. Among these appendages, hair follicles are the most important with regards to the surface area and skin depth. To understand follicular penetration, it is essential to know hair follicle densities at different body sites, size of their orifices, follicular volume, and surface area. Otberg et al. studied the characteristics of hair follicles at seven different areas in the body, lateral forehead, thorax, back, upper arm, forearm, thigh, and calf. Areas with highest and lowest density were forehead and calf with the values 292 and 29 follicle/cm^2, respectively. In terms of diameter of the follicular orifice, there is considerable variation between different body sites with smallest diameter openings reported in forehead and largest diameters in the calf region. Areas with higher follicular density or with larger follicle orifice can be considered to offer higher transfollicular absorption. The hair shaft on the thigh and calf is significantly thicker than other regions. In addition, the volume of the follicular infundibula was measured with the forehead and calf having the highest volume, even though hair density in the forehead is 20 time higher, and forearm having the lowest density. Having very close follicular infundibula volume with large differences in hair density was explained by the fact that hair follicles are established during the foetal period and the density of the hair follicles depends on the area of the skin. With growth, the body proportions changes resulting in the movement of the hair follicles apart. In comparison to the extremities, the head has a lower growth resulting in having more numerous hair follicles on the scalp and in the face [99].

The epidermis is the outermost, multiple layered membrane which contains five layers (from outside to inside): stratum corneum, stratum lucidum, stratum granulosum, stratum spinosum, and stratum basale (Figure 4). The basement membrane is the dermal-epidermal junction that maintains their adhesion and acts as a mechanical barrier for the diffusion of large molecules and migration of malignant cells from the epidermis to dermis. Attached to the basement membrane is stratum basale which is a column of cuboidal single-cell layer attached to the basement membrane by hemidesmosomes and joined to stratum spinosum by desmosomes. Keratinocytes, melanocytes, Langerhans cells and Merkle cells are cells found within the basal layer. The next layer is stratum spinosum which is composed of 2-6 layers of keratinocytes that differentiate within this layer to form keratin. On top of this layer is stratum granulosum, which is 1-3 layers thick, where the keratinocytes continue to differentiate, form keratin, and start to flatten. Keratohyalin granules and membrane-coating granules which contain lamellar subunits are within this layer. They are arranged in parallel stacks and are precursors of intercellular lipid lamellae of the stratum corneum. The next layer is the stratum lucidum which is a clear layer composed of 3-5 cell layers and keratinocytes forming this layer are dead and flattened. The cells are densely packed with eleidin (a clear protein rich in lipids) derived from keratohyalin which is converted to keratin in the upper part of the layer. The stratum corneum is the outermost layer and is composed of 10-15 cell layers and is 5-20 µm thick when dry. It provides a protective barrier and is the main barrier for topical and transdermal drug delivery. It is composed of a corneocytes network, which result from programmed destruction of the keratinocytes from the basal layer of the epidermis, in an extracellular lipid matrix. This forms the “bricks and mortar” model with the protein rich corneocytes are embedded in a lipid matrix; the organisation of the extracellular lipid matrix forms lamellar membranes. The lamella of the stratum corneum intracellular lipids has two co-existing phases based on the repeat distance between lipid head groups, short periodicity (∼6.4 nm) and long periodicity (∼13.4 nm). The lateral packing of the lipid takes three states: crystalline highly ordered densely packed orthorhombic phase which exhibits low permeability to drug molecules, gel-like ordered less densely packed hexagonal phase which is more permeable and a liquid phase which is disordered and more permeable [97,98].

There are three potential pathways across the epidermis for the penetration of drug molecules applied to the skin surface, sweat ducts, hair follicles and sebaceous gland (transappendageal route) or across the stratum corneum (transcellular and intercellular routes). Most molecules permeate the skin by a combination of pathways dependent on the physicochemical properties of the permeating molecule [98,100].

The transcellular route is also known as polar route through the stratum corneum as the corneocytes are polar in nature and hydrated as they contain intercellular keratin matrix. However, molecules permeating via this route must partition repeatedly between the polar corneocytes and lipid domains. The intercellular route is through the lipid bilayers in the stratum corneum where the permeant diffuses through intercellular lipid domains. However, the lipid composition within the stratum corneum exists in variety states, crystalline, gel-like and liquid with variable permeabilities. This offers multiple domains for the distribution and diffusion of drugs with different physicochemical properties [98,100].

The appendages offer a shunt route, which is low resistant, for the molecules to enter the lower layers of the skin without having to pass through the stratum corneum. However, they represent 0.1-1% of the skin surface area with variability from forearm to forehead. Moreover, eccrine ducts are relatively small and are filled with sweat, and hair follicle pore is larger, but they are less numerous, and the sebaceous gland is filled with sebum. However, from the above discussion on hair follicle distribution and dimensions in different areas of the body, the contribution of hair follicles in transdermal drug delivery cannot be ignored [98–102].

Nanoparticles targeted delivery to follicles and possible applications

Various of nanoparticles for skin delivery are available as they offer higher drug concentration, enhanced chemical and physical stability, and they provide both sustained and controlled drug release [102]. The stratum corneum is the primary barrier for drugs applied topically to the skin and lipid content of this layer is considered the main rate-limiting factor for diffusion. Most literature suggests that nanoparticles are too big to permeate through intact human skin and indeed most commercially successful products contain relatively small molecular weight drugs (typically < 500 Da). However, some reports suggest that 13 nm sized pores were reported between the hydrophilic heads which when the stratum corneum is hydrated, larger aqueous channels are formed between the lipids. This may facilitate the diffusion of small size nanoparticles through these pores; however, size is not the only factor enhance penetration. Surface chemistry plays an important role in nanomaterial penetration [103]. Modifying 95 nm nanoparticles with positively charged chitosan enabled the cutaneous penetration of these nanoparticles [104]. Moreover, selective accumulation of nanomaterials that do not penetrate the stratum corneum within the pilosebaceous unit is reported which can be used for targeted drug delivery especially in areas with high follicular density [103,105,106]. Vogt et al. reported the penetration of only 40 nm particles through vellus hair opening and through the follicular epithelium and internalisation of these nanoparticles by Langerhans cells after transcutaneous application of 40, 750 and 1500 nm nanoparticles [107]. Several types of nanoparticles were exploited for follicular drug delivery. Superior penetration and longer storage within the hair follicle of polymeric nanoparticles sized 320 nm in comparison to non-nanoparticle formulation was reported [105]. Limcharoen et al. prepared chitosan grafted retinal, a vitamin A derivative used for acne, to overcome dose-related side effect and enhance its penetration and bioavailability. They reported a significant increase of retinal concentration in the stratum corneum and hair follicle which can be of potential use for the treatment of acne and retinoid responsive skin diseases [108]. Lipid nanoparticles can be of potential benefit for follicular drug delivery due to the presence of sebum which is lipophilic [102]. Increased follicular uptake of lipid nanoparticles and liposomes was observed. Diphencyprone, an agent used to trat alopecia areata, was loaded into a nanostructured lipid carrier to improve skin uptake and follicular targeting. Three formulations were prepared using different emulsifiers, hydrogenated soybean phosphatidylcholine (SPC) and soyethyl morpholinium ethosulfate (SME) with two different concentrations of SPC. The resulting nanoparticles were in the size range 308-365 nm with negative zeta potential for those prepared using SPC and positive zeta potential for nanoparticles prepared using SME. Enhanced percutaneous and follicular uptake was reported for all three formulations with improved diphencyprone delivery to the hair follicles for lipid nanocarriers with excess SPC. In addition, a cationic lipid nanocarrier showed selective penetration to the hair follicle with minimised total skin deposition and intercellular route [109]. The penetration of 5 liposomal formulations (amphoteric, anionic, cationic, hydrophilic, and lipophilic dye loaded) in the hair follicles was studied by Jung et al. Generally, all liposomes showed greater penetration depth in comparison to a standard formulation. Amphoteric and cationic liposomes showed greater penetration depth with an average of almost 70% of the full hair follicle length [109].

Aims and objectives

As seen from above, targeted delivery of drugs using various nanosystems has been extensively researched to achieve enhanced efficacy and reduce side effects. The eye and the skin are composed of complex multiple barriers which require formulations with unique properties to overcome them. There is a great interest in thiolated silica due to the potential for functionalisation and modification for various applications such as drug delivery, imaging, and diagnostics. In this study, the synthesis of thiolated silica nanoparticles was extensively investigated to understand the effects of varying the synthesis condition on the characteristics of the resulting nanoparticles. The stability of the nanoparticles on skin and penetration of thiolated and PEGylated nanoparticles into the hair follicles, to overcome the barrier function of the stratum corneum, was investigated. In addition, the mucoadhesion of the nanoparticles to the surface of the eye, bladder, and the intestinal mucosa was extensively investigated in previous studies in addition to their diffusion in mucin and in aqueous polymer solution. The diffusivity of thiolated and PEGylated silica nanoparticles in the vitreous humour was researched.

References:

(1) McNeil, S. E. Unique Benefits of Nanotechnology to Drug Delivery and Diagnostics. *Methods Mol. Biol.* **2011**, *697*, 3–8.

(2) Chenthamara, D.; Subramaniam, S.; Ramakrishnan, S. G.; Krishnaswamy, S.; Essa, M. M.; Lin, F. H.; Qoronfleh, M. W. Therapeutic Efficacy of Nanoparticles and Routes of Administration. *Biomater. Res.* **2019**, *23*, 1–29.

(3) Mudshinge, S. R.; Deore, A. B.; Patil, S.; Bhalgat, C. M. Nanoparticles: Emerging Carriers for Drug Delivery. *Saudi Pharm. J.* **2011**, *19*, 129–141.

(4) Wilczewska, A. Z.; Niemirowicz, K.; Markiewicz, K. H.; Car, H. Nanoparticles as Drug Delivery Systems. *Pharmacol. Reports* **2012**, *64*, 1020–1037.

(5) Bose, R. J. C.; Lee, S. H.; Park, H. Biofunctionalized Nanoparticles: An Emerging Drug Delivery Platform for Various Disease Treatments. *Drug Discov. Today* **2016**, *21*, 1303–1312.

(6) Barenholz, Y. Doxil® - The First FDA-Approved Nano-Drug: Lessons Learned. *J. Control. Release* **2012**, *160*, 117–134.

(7) Norouzi, P.; Rastegari, A.; Mottaghitalab, F.; Farokhi, M.; Zarrintaj, P.; Saeb, M. R. Nanoemulsions for Intravenous Drug Delivery. In *Nanoengineered Biomaterials for Advanced Drug Delivery*; Mozafari, M., Ed.; Elsevier Ltd., 2020; pp 581–601.

(8) Selvarajan, V.; Obuobi, S.; Ee, P. L. R. Silica Nanoparticles—A Versatile Tool for the Treatment of Bacterial Infections. *Front. Chem.* **2020**, *8*, 1–16.

(9) Vallet-Regí, M.; Colilla, M.; Izquierdo-Barba, I.; Manzano, M. Mesoporous Silica

Nanoparticles for Drug Delivery: Current Insights. *Molecules* **2018**, *23*, 1–19.

(10) Stöber, W.; Fink, A.; Bohn, E. Controlled Growth of Monodisperse Silica Spheres in the Micron Size Range. *J. Colloid Interface Sci.* **1968**, *26*, 62–69.

(11) Irmukhametova, G. S.; Mun, G. A.; Khutoryanskiy, V. V. Thiolated Mucoadhesive and PEGylated Nonmucoadhesive Organosilica Nanoparticles from 3-Mercaptopropyltrimethoxysilane. *Langmuir* **2011**, *27*, 9551–9556.

(12) Nakamura, M.; Ishimura, K. Synthesis and Characterization of Organosilica Nanoparticles Prepared from 3-Mercaptopropyltrimethoxysilane as the Single Silica Source. *J. Phys. Chem. C* **2007**, *111*, 18892–18898.

(13) Nakamura, M.; Ishimura, K. One-Pot Synthesis and Characterization of Three Kinds of Thiol−Organosilica Nanoparticles. *Langmuir* **2008**, *24*, 5099–5108.

(14) Nakamura, M.; Ozaki, S.; Abe, M.; Doi, H.; Matsumoto, T.; Ishimura, K. Size-Controlled Synthesis, Surface Functionalization, and Biological Applications of Thiol-Organosilica Particles. *Colloids Surfaces B Biointerfaces* **2010**, *79*, 19–26.

(15) Ways, T. M. M.; Lau, W. M.; Ng, K. W.; Khutoryanskiy, V. V. Synthesis of Thiolated, PEGylated and POZylated Silica Nanoparticles and Evaluation of Their Retention on Rat Intestinal Mucosa in Vitro. *Eur. J. Pharm. Sci.* **2018**, *122*, 230–238.

(16) Mun, E. A.; Williams, A. C.; Khutoryanskiy, V. V. Adhesion of Thiolated Silica Nanoparticles to Urinary Bladder Mucosa: Effects of PEGylation, Thiol Content and Particle Size. *Int. J. Pharm.* **2016**, *512*, 32–38.

(17) Storha, A.; Mun, E. A.; Khutoryanskiy, V. V. Synthesis of Thiolated and Acrylated Nanoparticles Using Thiol-Ene Click Chemistry: Towards Novel Mucoadhesive Materials for Drug Delivery. *RSC Adv.* **2013**, *3*, 12275–12279.

(18) Mun, E. A.; Morrison, P. W. J.; Williams, A. C.; Khutoryanskiy, V. V. On the Barrier Properties of the Cornea: A Microscopy Study of the Penetration of Fluorescently Labeled Nanoparticles, Polymers, and Sodium Fluorescein. *Mol. Pharm.* **2014**, *11*, 3556–3564.

(19) Mansfield, E. D. H.; de la Rosa, V. R.; Kowalczyk, R. M.; Grillo, I.; Hoogenboom, R.; Sillence, K.; Hole, P.; Williams, A. C.; Khutoryanskiy, V. V. Side Chain Variations Radically Alter the Diffusion of Poly(2-Alkyl-2-Oxazoline) Functionalised

Nanoparticles through a Mucosal Barrier. *Biomater. Sci.* **2016**, *4*, 1318–1327.

(20) Ways, T. M. M.; Ng, K. W.; Lau, W. M.; Khutoryanskiy, V. V. Silica Nanoparticles in Transmucosal Drug Delivery. *Pharmaceutics* **2020**, *12*, 1–25.

(21) Esquena, J.; Pons, R.; Azemar, N.; Caelles, J.; Solans, C. Preparation of Monodisperse Silica Particles in Emulsion Media. *Colloids Surfaces A Physicochem. Eng. Asp.* **1997**, *123–124*, 575–586.

(22) Bagwe, R. P.; Hilliard, L. R.; Tan, W. Surface Modification of Silica Nanoparticles to Reduce Aggregation and Nonspecific Binding. *Langmuir* **2006**, *22*, 4357–4362.

(23) Prüfert, F.; Bonengel, S.; Menzel, C.; Bernkop-Schnürch, A. Enhancing the Efficiency of Thiomers: Utilizing a Highly Mucoadhesive Polymer as Backbone for Thiolation and Preactivation. *Eur. J. Pharm. Sci.* **2017**, *96*, 309–315.

(24) Mahmood, A.; Bonengel, S.; Laffleur, F.; Ijaz, M.; Leonaviciute, G.; Bernkop-Schnürch, A. An In-Vitro Exploration of Permeation Enhancement by Novel Polysulfonate Thiomers. *Int. J. Pharm.* **2015**, *496*, 304–313.

(25) Bernkop-Schnürch, A.; Walker, G. Multifunctional Matrices for Oral Peptide Delivery. *Crit. Rev. Ther. Drug Carrier Syst.* **2001**, *5*, 459–501.

(26) Bernkop-Schnrüch, A.; Schwarz, V.; Steininger, S. Schnürch - Polymer with Thiol Groups.Pdf. *Pharmaceutical Research*. 1999, pp 876–881.

(27) Palmberger, T. F.; Laffleur, F.; Greindl, M.; Bernkop-Schnürch, A. In Vivo Evaluation of Anionic Thiolated Polymers as Oral Delivery Systems for Efflux Pump Inhibition. *Int. J. Pharm.* **2015**, *491*, 318–322.

(28) Nakamura, M.; Ozaki, S.; Abe, M.; Matsumoto, T.; Ishimura, K. One-Pot Synthesis and Characterization of Dual Fluorescent Thiol-Organosilica Nanoparticles as Non-Photoblinking Quantum Dots and Their Applications for Biological Imaging. *J. Mater. Chem.* **2011**, *21*, 4689–4695.

(29) Melnyk, I. V.; Zub, Y. L.; Véron, E.; Massiot, D.; Cacciaguerra, T.; Alonso, B. Spray-Dried Mesoporous Silica Microspheres with Adjustable Textures and Pore Surfaces Homogenously Covered by Accessible Thiol Functions. *J. Mater. Chem.* **2008**, *18*, 1368–1382.

(30) Chen, F.; Hong, H.; Zhang, Y.; Valdovinos, H. F.; Shi, S.; Kwon, G. S.; Theuer, C. P.;

Barnhart, T. E.; Cai, W. In Vivo Tumor Targeting and Image-Guided Drug Delivery with Antibody-Conjugated, Radiolabeled Mesoporous Silica Nanoparticles. *ACS Nano* **2013**, *7*, 9027–9039.

(31) Dong, W.; Li, Y.; Niu, D.; Ma, Z.; Gu, J.; Chen, Y.; Zhao, W.; Liu, X.; Liu, C.; Shi, J. Facile Synthesis of Monodisperse Superparamagnetic Fe 3O 4 Core@hybrid@Au Shell Nanocomposite for Bimodal Imaging and Photothermal Therapy. *Adv. Mater.* **2011**, *23*, 5392–5397.

(32) Trofimov, A. D.; Ivanova, A. A.; Zyuzin, M. V.; Timin, A. S. Porous Inorganic Carriers Based on Silica, Calcium Carbonate and Calcium Phosphate for Controlled/Modulated Drug Delivery: Fresh Outlook and Future Perspectives. *Pharmaceutics* **2018**, *10*, 1–35.

(33) Zhou, J.; Hao, N.; De Zoyza, T.; Yan, M.; Ramström, O. Lectin-Gated, Mesoporous, Photofunctionalized Glyconanoparticles for Glutathione-Responsive Drug Delivery. *Chem. Commun.* **2015**, *51*, 9833–9836.

(34) Cheng, R.; Feng, F.; Meng, F.; Deng, C.; Feijen, J.; Zhong, Z. Glutathione-Responsive Nano-Vehicles as a Promising Platform for Targeted Intracellular Drug and Gene Delivery. *J. Control. Release* **2011**, *152*, 2–12.

(35) Quignard, S.; Masse, S.; Laurent, G.; Coradin, T. Introduction of Disulfide Bridges within Silica Nanoparticles to Control Their Intra-Cellular Degradation. *Chem. Commun.* **2013**, *49*, 3410–3412.

(36) Xu, Z.; Zhang, K.; Liu, X.; Zhang, H. A New Strategy to Prepare Glutathione Responsive Silica Nanoparticles. *RSC Adv.* **2013**, *3*, 17700–17702.

(37) Yang, Y.; Wan, J.; Niu, Y.; Gu, Z.; Zhang, J.; Yu, M.; Yu, C. Structure-Dependent and Glutathione-Responsive Biodegradable Dendritic Mesoporous Organosilica Nanoparticles for Safe Protein Delivery. *Chem. Mater.* **2016**, *24*, 9008–9016.

(38) Huang, P.; Chen, Y.; Lin, H.; Yu, L.; Zhang, L.; Wang, L.; Zhu, Y.; Shi, J. Molecularly Organic/Inorganic Hybrid Hollow Mesoporous Organosilica Nanocapsules with Tumor-Specific Biodegradability and Enhanced Chemotherapeutic Functionality. *Biomaterials* **2017**, *125*, 23–37.

(39) Doura, T.; Nishio, T.; Tamanoi, F.; Nakamura, M. Relationship between the Glutathione-Responsive Degradability of Thiol-Organosilica Nanoparticles and the

Chemical Structures. *J. Mater. Res.* **2019**, *34*, 1266–1278.

(40) Mun, E. A.; Hannell, C.; Rogers, S. E.; Hole, P.; Williams, A. C.; Khutoryanskiy, V. V. On the Role of Specific Interactions in the Diffusion of Nanoparticles in Aqueous Polymer Solutions. *Langmuir* **2014**, *30*, 308–317.

(41) Mansfield, E. D. H.; Sillence, K.; Hole, P.; Williams, A. C.; Khutoryanskiy, V. V. POZylation: A New Approach to Enhance Nanoparticle Diffusion through Mucosal Barriers. *Nanoscale* **2015**, *7*, 13671–13679.

(42) Mansfield, E. D. H.; Pandya, Y.; Mun, E. A.; Rogers, S. E.; Abutbul-Ionita, I.; Danino, D.; Williams, A. C.; Khutoryanskiy, V. V. Structure and Characterisation of Hydroxyethylcellulose-Silica Nanoparticles. *RSC Adv.* **2018**, *8*, 6471–6478.

(43) Mansfield, E. D. H.; Filippov, S. K.; De, V. R.; Cook, M. T.; Grillo, I.; Hoogenboom, R.; Williams, A. C.; Khutoryanskiy, V. V. Understanding the Temperature Induced Aggregation of Silica Nanoparticles Decorated with Temperature-Responsive Polymers : Can a Small Step in the Chemical Structure Make a Giant Leap for a Phase Transition ? *J. Colloid Interface Sci.* **2021**, *590*, 249–259.

(44) Khutoryanskiy, V. V. Advances in Mucoadhesion and Mucoadhesive Polymers. *Macromol. Biosci.* **2011**, *11*, 748–764.

(45) Smart, J. D. The Basics and Underlying Mechanisms of Mucoadhesion. *Adv. Drug Deliv. Rev.* **2005**, *57*, 1556–1568.

(46) Deutel, B.; Laffleur, F.; Palmberger, T.; Saxer, A.; Thaler, M.; Bernkop-Schnürch, A. In Vitro Characterization of Insulin Containing Thiomeric Microparticles as Nasal Drug Delivery System. *Eur. J. Pharm. Sci.* **2016**, *81*, 157–161.

(47) Barthelmes, J.; Dünnhaupt, S.; Unterhofer, S.; Perera, G.; Schlocker, W.; Bernkop-Schnürch, A. Thiolated Particles as Effective Intravesical Drug Delivery Systems for Treatment of Bladder-Related Diseases. *Nanomedicine* **2013**, *8*, 65–75.

(48) Albrecht, K.; Zirm, E. J.; Palmberger, T. F.; Schlocker, W.; Bernkop-Schnürch, A. Preparation of Thiomer Microparticles and in Vitro Evaluation of Parameters Influencing Their Mucoadhesive Properties. *Drug Dev. Ind. Pharm.* **2006**, *32*, 1149–1157.

(49) Schairer, D. O.; Chouake, J. S.; Nosanchuk, J. D.; Friedman, A. J. The Potential of

Nitric Oxide Releasing Therapies as Antimicrobial Agents. *Virulence* **2012**, *3*, 271–279.

(50) Chang, W. L.; Peng, K. J.; Hu, T. M.; Chiu, S. J.; Liu, Y. L. Nitric Oxide-Releasing S-Nitrosothiol-Modified Silica/Chitosan Core-Shell Nanoparticles. *Polymer (Guildf).* **2015**, *57*, 70–76.

(51) Li, Z. Y.; Hu, J. J.; Xu, Q.; Chen, S.; Jia, H. Z.; Sun, Y. X.; Zhuo, R. X.; Zhang, X. Z. A Redox-Responsive Drug Delivery System Based on RGD Containing Peptide-Capped Mesoporous Silica Nanoparticles. *J. Mater. Chem. B* **2015**, *3*, 39–44.

(52) Xiao, D.; Jia, H. Z.; Zhang, J.; Liu, C. W.; Zhuo, R. X.; Zhang, X. Z. A Dual-Responsive Mesoporous Silica Nanoparticle for Tumor-Triggered Targeting Drug Delivery. *Small* **2014**, *10*, 591–598.

(53) Kim, H.; Kim, S.; Park, C.; Lee, H.; Park, H. J.; Kim, C. Glutathione-Induced Intracellular Release of Guests from Mesoporous Silica Nanocontainers with Cyclodextrin Gatekeepers. *Adv. Mater.* **2010**, *22*, 4280–4283.

(54) Gayam, S. R.; Wu, S. P. Redox Responsive Pd(Ii) Templated Rotaxane Nanovalve Capped Mesoporous Silica Nanoparticles: A Folic Acid Mediated Biocompatible Cancer-Targeted Drug Delivery System. *J. Mater. Chem. B* **2014**, *2*, 7009–7016.

(55) Ellison, P. A.; Chen, F.; Goel, S.; Barnhart, T. E.; Nickles, R. J.; DeJesus, O. T.; Cai, W. Intrinsic and Stable Conjugation of Thiolated Mesoporous Silica Nanoparticles with Radioarsenic. *ACS Appl. Mater. Interfaces* **2017**, *9*, 6772–6781.

(56) von Baeckmann, C.; Guillet-Nicolas, R.; Renfer, D.; Kählig, H.; Kleitz, F. A Toolbox for the Synthesis of Multifunctionalized Mesoporous Silica Nanoparticles for Biomedical Applications. *ACS omega* **2018**, *3*, 17496–17510.

(57) Kalantari, M.; Ghosh, T.; Liu, Y.; Zhang, J.; Zou, J.; Lei, C.; Yu, C. Highly Thiolated Dendritic Mesoporous Silica Nanoparticles with High-Content Gold as Nanozymes: The Nano-Gold Size Matters. *ACS Appl. Mater. Interfaces* **2019**, *11*, 13264–13272.

(58) Královec, K.; Melounková, L.; Slováková, M.; Mannová, N.; Sedlák, M.; Bartáček, J.; Havelek, R. Disruption of Cell Adhesion and Cytoskeletal Networks by Thiol-Functionalized Silica-Coated Iron Oxide Nanoparticles. *Int. J. Mol. Sci.* **2020**, *21*, 1–19.

(59) Mun, E. A. Functionalised Organosilica Nanoparticles: Synthesis, Mucoadhesion and Diffusion, 2014.

(60) Adriaens, E.; Remon, J. P. Gastropods as an Evaluation Tool for Screening the Irritating Potency of Absorption Enhancers and Drugs. *Pharm. Res.* **1999**, *16*, 1240–1244.

(61) Morrison, P. W. J.; Khutoryanskiy, V. V. Anatomy of the Eye and the Role of Ocular Mucosa in Drug Delivery. In *Mucoadhesive Materials and Drug Delivery Systems*; Khutoryanskiy, V. V., Ed.; Wiley Online Books; 2014; pp 39–60.

(62) Moiseev, R. V.; Morrison, P. W. J.; Steele, F.; Khutoryanskiy, V. V. Penetration Enhancers in Ocular Drug Delivery. *Pharmaceutics* **2019**, *11*, 1–33.

(63) Abdulrazik, M.; Benita, S.; Behar-Cohen, F. Drug Delivery Systems for Enhanced Ocular Absorption. In *Enhancement in Drug Delivery*; Touitou, E., Barry, B. W., Eds.; Taylor & Francis Group, 2006; pp 490–517.

(64) Wilson*, C. G.; Tan, L. E. Nanostructures Overcoming the Ocular Barrier: Physiological Considerations and Mechanistic Issues. In *Nanostructured Biomaterials for Overcoming Biological Barriers*; The Royal Society of Chemistry, 2012; pp 173–189.

(65) Kang-Mieler, J. J.; Rudeen, K. M.; Liu, W.; Mieler, W. F. Advances in Ocular Drug Delivery Systems. *Eye* **2020**, *34*, 1371–1379.

(66) Subrizi, A.; del Amo, E. M.; Korzhikov-Vlakh, V.; Tennikova, T.; Ruponen, M.; Urtti, A. Design Principles of Ocular Drug Delivery Systems: Importance of Drug Payload, Release Rate, and Material Properties. *Drug Discov. Today* **2019**, *24*, 1446–1457.

(67) Patel, A. Ocular Drug Delivery Systems: An Overview. *World J. Pharmacol.* **2013**, *2*, 47.

(68) Prausnitz, M. R.; Noonan, J. S. Permeability of Cornea, Sclera, and Conjunctiva: A Literature Analysis for Drug Delivery to the Eye. *J. Pharm. Sci.* **1998**, *87*, 1479–1488.

(69) Wadhwa, S.; Paliwal, R.; Paliwal, S.; Vyas, S. Nanocarriers in Ocular Drug Delivery: An Update Review. *Curr. Pharm. Des.* **2009**, *15*, 2724–2750.

(70) Tajika, T.; Isowaki, A.; Sakaki, H. Ocular Distribution of Difluprednate Ophthalmic Emulsion 0.05% in Rabbits. *J. Ocul. Pharmacol. Ther.* **2010**, *27*, 43–49.

(71) Scoper, S. V; Kabat, A. G.; Owen, G. R.; Stroman, D. W.; Kabra, B. P.; Faulkner, R.; Kulshreshtha, A. K.; Rusk, C.; Bell, B.; Jamison, T.; Bernal-Perez, L. F.; Brooks, A. C.; Nguyen, V. A. Ocular Distribution, Bactericidal Activity and Settling Characteristics of TobraDex ST Ophthalmic Suspension Compared with TobraDex Ophthalmic Suspension. *Adv. Ther.* **2008**, *25*, 77—88.

(72) Omerović, N.; Vranić, E. Application of Nanoparticles in Ocular Drug Delivery Systems. *Health Technol. (Berl).* **2020**, *10*, 61–78.

(73) Rodrigues, F. S. C.; Campos, A.; Martins, J.; Ambrósio, A. F.; Campos, E. J. Emerging Trends in Nanomedicine for Improving Ocular Drug Delivery: Light-Responsive Nanoparticles, Mesoporous Silica Nanoparticles, and Contact Lenses. *ACS Biomater. Sci. Eng.* **2020**, *6*, 6587–6597.

(74) Gorantla, S.; Rapalli, V. K.; Waghule, T.; Singh, P. P.; Dubey, S. K.; Saha, R. N.; Singhvi, G. Nanocarriers for Ocular Drug Delivery: Current Status and Translational Opportunity. *RSC Adv.* **2020**, *10*, 27835–27855.

(75) Tsai, C. H.; Wang, P. Y.; Lin, I. C.; Huang, H.; Liu, G. S.; Tseng, C. L. Ocular Drug Delivery: Role of Degradable Polymeric Nanocarriers for Ophthalmic Application. *Int. J. Mol. Sci.* **2018**, *19*.

(76) Nagarwal, R. C.; Kant, S.; Singh, P. N.; Maiti, P.; Pandit, J. K. Polymeric Nanoparticulate System: A Potential Approach for Ocular Drug Delivery. *J. Control. Release* **2009**, *136*, 2–13.

(77) Reimondez-Troitiño, S.; Csaba, N.; Alonso, M. J.; De La Fuente, M. Nanotherapies for the Treatment of Ocular Diseases. *Eur. J. Pharm. Biopharm.* **2015**, *95*, 279–293.

(78) Tseng, C. L.; Chen, K. H.; Su, W. Y.; Lee, Y. H.; Wu, C. C.; Lin, F. H. Cationic Gelatin Nanoparticles for Drug Delivery to the Ocular Surface: In Vitro and in Vivo Evaluation. *J. Nanomater.* **2013**, *2013*, 1–11.

(79) Hagigit, T.; Abdulrazik, M.; Valamanesh, F.; Behar-Cohen, F.; Benita, S. Ocular Antisense Oligonucleotide Delivery by Cationic Nanoemulsion for Improved Treatment of Ocular Neovascularization: An in-Vivo Study in Rats and Mice. *J. Control. Release* **2012**, *160*, 225–231.

(80) Joseph, R. R.; Venkatraman, S. S. Drug Delivery to the Eye: What Benefits Do Nanocarriers Offer? *Nanomedicine* **2017**, *12*, 683–702.

(81) Jo, D. H.; Lee, T. G.; Kim, J. H. Nanotechnology and Nanotoxicology in Retinopathy. *Int. J. Mol. Sci.* **2011**, *12*, 8288–8301.

(82) Bisht, R.; Mandal, A.; Jaiswal, J. K.; Rupenthal, I. D. Nanocarrier Mediated Retinal Drug Delivery: Overcoming Ocular Barriers to Treat Posterior Eye Diseases. *Wiley Interdiscip. Rev. Nanomedicine Nanobiotechnology* **2018**, *10*, 1–21.

(83) Koo, H.; Moon, H.; Han, H.; Na, J. H.; Huh, M. S.; Park, J. H.; Woo, S. J.; Park, K. H.; Chan Kwon, I.; Kim, K.; Kim, H. The Movement of Self-Assembled Amphiphilic Polymeric Nanoparticles in the Vitreous and Retina after Intravitreal Injection. *Biomaterials* **2012**, *33*, 3485–3493.

(84) Zhang, Q.; Li, J.; Gao, W.; Zhang, L. Nanoparticles for Ocular Drug Delivery. In *Ophthalmic Disease Mechanisms and Drug Discovery*; Zhang, K., Ed.; WORLD SCIENTIFIC, 2015; pp 197–223.

(85) Kaur, I. P.; Kakkar, S. Nanotherapy for Posterior Eye Diseases. *J. Control. Release* **2014**, *193*, 100–112.

(86) Bhatta, R. S.; Chandasana, H.; Chhonker, Y. S.; Rathi, C.; Kumar, D.; Mitra, K.; Shukla, P. K. Mucoadhesive Nanoparticles for Prolonged Ocular Delivery of Natamycin: In Vitro and Pharmacokinetics Studies. *Int. J. Pharm.* **2012**, *432*, 105–112.

(87) Zhang, L.; Li, Y.; Zhang, C.; Wang, Y.; Song, C. Pharmacokinetics and Tolerance Study of Intravitreal Injection of Dexamethasone-Loaded Nanoparticles in Rabbits. *Int. J. Nanomedicine* **2009**, *4*, 175–183.

(88) Qu, W.; Meng, B.; Yu, Y.; Wang, S. EpCAM Antibody-Conjugated Mesoporous Silica Nanoparticles to Enhance the Anticancer Efficacy of Carboplatin in Retinoblastoma. *Mater. Sci. Eng. C* **2017**, *76*, 646–651.

(89) Liao, Y. Te; Lee, C. H.; Chen, S. T.; Lai, J. Y.; Wu, K. C. W. Gelatin-Functionalized Mesoporous Silica Nanoparticles with Sustained Release Properties for Intracameral Pharmacotherapy of Glaucoma. *J. Mater. Chem. B* **2017**, *5*, 7008–7013.

(90) Sun, J. G.; Jiang, Q.; Zhang, X. P.; Shan, K.; Liu, B. H.; Zhao, C.; Yan, B. Mesoporous Silica Nanoparticles as a Delivery System for Improving Antiangiogenic Therapy. *Int. J. Nanomedicine* **2019**, *14*, 1489–1501.

(91) Park, J. H.; Jeong, H.; Hong, J.; Chang, M.; Kim, M.; Chuck, R. S.; Lee, J. K.; Park, C.

Y. The Effect of Silica Nanoparticles on Human Corneal Epithelial Cells. *Sci. Rep.* **2016**, *6*, 1–11.

(92) Alvarez-Rivera, F.; Fernández-Villanueva, D.; Concheiro, A.; Alvarez-Lorenzo, C. α-Lipoic Acid in Soluplus® Polymeric Nanomicelles for Ocular Treatment of Diabetes-Associated Corneal Diseases. *J. Pharm. Sci.* **2016**, *105*, 2855–2863.

(93) Li, M.; Xin, M.; Guo, C.; Lin, G.; Wu, X. New Nanomicelle Curcumin Formulation for Ocular Delivery: Improved Stability, Solubility, and Ocular Anti-Inflammatory Treatment. *Drug Dev. Ind. Pharm.* **2017**, *43*, 1846–1857.

(94) Pepiæ, I.; Lovriæ, J.; Filipoviæ-Grèiæ, J. Polymeric Micelles in Ocular Drug Delivery: Rationale, Strategies and Challenges. *Chem. Biochem. Eng. Q.* **2012**, *26* (4), 365–377.

(95) Brown, D. M.; Kaiser, P. K.; Michels, M.; Soubrane, G.; Heier, J. S.; Kim, R. Y.; Sy, J. P.; Schneider, S. Ranibizumab versus Verteporfin for Neovascular Age-Related Macular Degeneration. *N. Engl. J. Med.* **2006**, *355*, 1432–1444.

(96) Abrishami, M.; Ganavati, S. Z.; Soroush, D.; Rouhbakhsh, M.; Jaafari, M. R.; Malaekeh-Nikouei, B. Preparation, Characterization, and in Vivo Evaluation of Nanoliposomes-Encapsulated Bevacizumab (AVASTIN) for Intravitreal Administration. *RETINA* **2009**, *29*, 699–703.

(97) Brown, M. B.; Williams, A. C. Structure and Function of Human Skin. In *The art and science of dermal formulation development*; CRC Press: Florida, 2019; pp 1–12.

(98) Benson, H. A. E. Skin Structure, Function, and Permeation. In *Topical and Transdermal Drug Delivery*; Benson, H. A. E., Watkinson, A. C., Eds.; Wiley Online Books; 2011; pp 1–22.

(99) Otberg, N.; Richter, H.; Schaefer, H.; Blume-Peytavi, U.; Sterry, W.; Lademann, J. Variations of Hair Follicle Size and Distribution in Different Body Sites. *J. Invest. Dermatol.* **2004**, *122*, 14–19.

(100) Brown, M. B.; Williams, A. C. Theoretical Aspects of Transdermal and Topical Drug Delivery. In *The art and science of dermal formulation development*; CRC Press: Florida, 2019; pp 21–34.

(101) Lademann, J.; Otberg, N.; Jacobi, U.; Hoffman, R. M.; Blume-Peytavi, U. Follicular Penetration and Targeting. *J. Investig. Dermatol. Symp. Proc.* **2005**, *10*, 301–303.

(102) Patzelt, A.; Lademann, J. Recent Advances in Follicular Drug Delivery of Nanoparticles. *Expert Opin. Drug Deliv.* **2020**, *17*, 49–60.

(103) Mordorski, B.; Landriscina, A.; Friedman, A. An Overview of Nanomaterials in Dermatology. In *Nanoscience in Dermatology*; Hamblin, M. R., Avci, P., Prow, T. W. B. T.-N. in D., Eds.; Academic Press, 2016; pp 31–46.

(104) Tan, Q.; Liu, W.; Guo, C.; Zhai, G. Preparation and Evaluation of Quercetin-Loaded Lecithin-Chitosan Nanoparticles for Topical Delivery. *Int. J. Nanomedicine* **2011**, *6*, 1621–1630.

(105) Lademann, J.; Richter, H.; Teichmann, A.; Otberg, N.; Blume-Peytavi, U.; Luengo, J.; Weiß, B.; Schaefer, U. F.; Lehr, C.-M.; Wepf, R.; Sterry, W. Nanoparticles – An Efficient Carrier for Drug Delivery into the Hair Follicles. *Eur. J. Pharm. Biopharm.* **2007**, *66*, 159–164.

(106) Fang, C.-L.; Aljuffali, I. A.; Li, Y.-C.; Fang, J.-Y. Delivery and Targeting of Nanoparticles into Hair Follicles. *Ther. Deliv.* **2014**, *5*, 991–1006.

(107) Vogt, A.; Combadiere, B.; Hadam, S.; Stieler, K. M.; Lademann, J.; Schaefer, H.; Autran, B.; Sterry, W.; Blume-Peytavi, U. 40 Nm, but Not 750 or 1,500 Nm, Nanoparticles Enter Epidermal CD1a+ Cells after Transcutaneous Application on Human Skin. *J. Invest. Dermatol.* **2006**, *126*, 1316–1322.

(108) Limcharoen, B.; Toprangkobsin, P.; Banlunara, W.; Wanichwecharungruang, S.; Richter, H.; Lademann, J.; Patzelt, A. Increasing the Percutaneous Absorption and Follicular Penetration of Retinal by Topical Application of Proretinal Nanoparticles. *Eur. J. Pharm. Biopharm.* **2019**, *139*, 93–100.

(109) Lin, Y.-K.; Al-Suwayeh, S. A.; Leu, Y.-L.; Shen, F.-M.; Fang, J.-Y. Squalene-Containing Nanostructured Lipid Carriers Promote Percutaneous Absorption and Hair Follicle Targeting of Diphencyprone for Treating Alopecia Areata. *Pharm. Res.* **2013**, *30*, 435–446.

Chapter 2

Controlling the size of thiolated organosilica nanoparticles

The modified stöber is chosen for the synthesis as nanoparticles prepared using this method are small and their surfaces are rich in thiol. This chapter explores the effect of different reaction parameters on the characteristics of the resulting nanoparticles.

This chapter was published as Al Mahrooqi, J., Mun, E., Williams, A. and Khutoryanskiy, V., (2018). Controlling the Size of Thiolated Organosilica Nanoparticles. *Langmuir*, 34(28), pp.8347-8354.

Contributions

Ellina A. Mun carried out the experiments and the analysis on the effect of solvent.

LANGMUIR
Article
Cite This: *Langmuir* 2018, 34, 8347−8354
pubs.acs.org/Langmuir

Controlling the Size of Thiolated Organosilica Nanoparticles

Jamila H. Al Mahrooqi, Ellina A. Mun, Adrian C. Williams, and Vitaliy V. Khutoryanskiy*

Reading School of Pharmacy, University of Reading, Reading RG6 6AD, U.K.

Supporting Information

ABSTRACT: Nanoparticle characteristics, including their size, are governed by the reagents employed and the reaction parameters. Here, we systemically vary the catalyst, oxygen content, temperature, and solvent to modify the size and zeta-potential of thiolated organosilica nanoparticles. The particles were synthesized by self-condensation of 3-mercaptopropyltrimethoxysilane in a range of organic solvents in contact with oxygen, with NaOH and other catalysts. The particle size increased with increasing reaction temperature (70 ± 1 nm at 50 °C; 50 ± 1 nm at room temperature) but decreased when air was bubbled through the reaction mixture compared to no bubbling. A significant decrease in the particle size was seen when increasing the dielectric constant of the solvent and when increasing the catalyst concentration; from these, we provide empirical equations that can be used to design particle sizes by manipulating the dielectric constant of the solvent (or cosolvents) or by varying the NaOH catalyst concentration when dimethylsulfoxide is the selected solvent.

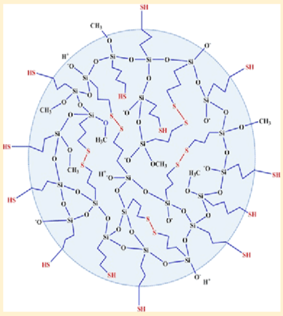

INTRODUCTION

The introduction of nanoparticles has led to major advances in fields including targeted therapeutics, medical diagnostics, molecular biology, and cell biology. Nanoparticles have been evaluated for cancer cell imaging, ultrasensitive single bacterium detection, deoxyribonucleic acid microarray detection, and gene delivery.[1−4] To fully exploit nanoparticles in these areas, they should provide strong signals (such as fluorescence), have high specificity and binding affinities, and, ideally, should be suitable for use in controlled release systems.[3,4] Doxil, an 80−85 nm PEGylated liposome encapsulating doxorubicin hydrochloride, and Abraxane, with paclitaxel bound to albumin in particles of ∼130 nm, are examples of nanoscale anticancer therapeutics currently approved by the US Food and Drug Administration.[6]

Silica nanoparticles are good candidates for biomedical applications because their production and separation are simple; they are hydrophilic and may be modified or labeled.[3] Further, many biological studies have shown them to be biocompatible and nontoxic.[7] The introduction of functional groups such as amines, thiols, and carboxyls is relatively straightforward because of the high surface area and silanol surface concentration in addition to the highly interconnected open spaces in their three-dimensional structure.[8,9] Researchers have sought to define the factors controlling the particle size and morphology of silica nanoparticles. Regulating hydrolysis during synthesis when alkoxysilanes are used as a pure silica source is an effective way to control size and can be achieved by adding alcohol, by varying the concentration of the catalyst and by selecting alkoxysilanes of different natures.[10] The temperature, pH, and type of catalyst used also affect the size of silica nanoparticles produced.[3,10−14]

Thiolated organosilica nanoparticles have attracted considerable attention for their ability to bind transition metals, with opportunities for diverse functionalization and use in catalysis.[5] Organosilicon molecules containing thiol groups have been successfully used for the synthesis of silsesquioxane-based thermally stable networks[15] and ionic liquids.[16] Thiolated organosilica nanoparticles are typically synthesized by co-condensing 3-mercaptopropyltrimethoxysilane (MPTS) with tetraethoxysilane or tetramethoxysilane in protic solvents such as water or alcohols. Co-condensation is induced by the addition of NaOH or NH_4OH, and the formed material has particle sizes larger than 500 nm.[3,5] The particle size was varied by changing the mercaptosilane derivative and concentration.[1,2] Fluorescent thiol-organosilica nanoparticles (100 nm) were used for time-lapse fluorescence imaging of mouse peritoneal macrophages, which clearly demonstrated cellular uptake and uptake kinetics.[17] Thiolated organosilica nanoparticles (sub-100 nm) were obtained by self-condensation of MPTS in dimethylsulfoxide (DMSO) in contact with atmospheric oxygen.[5,18] The resulting nanoparticles were versatile as they can be fluorescently labeled and are mucoadhesive, but as nonporous and nonswellable materials, opportunities for their drug loading were limited.[19]

The ability of thiolated nanoparticles to adhere to and to be retained on different mucosal tissues has been investigated in vitro.[5,20−22] Mucoadhesion and retention on mucosal surfaces is due to the disulfide bond formation between thiol groups available in mucin glycoproteins and on the surface of the nanoparticles.[23] It was reported that these materials exhibited strong adherence to ocular mucosal surfaces, but PEGylation of the nanoparticles significantly reduced mucoadhesion because of the reduction in the number of free thiol groups

Received: May 11, 2018
Revised: June 10, 2018
Published: June 18, 2018

DOI: 10.1021/acs.langmuir.8b01556
Langmuir 2018, 34, 8347−8354

but improved mucus penetration.[5,20,21] As the cornea acts as a chemical and mechanical barrier to the passage of external materials, including drugs, penetration of thiolated and PEGylated (750, 5000 Da) nanoparticles into intact, pretreated (with β-cyclodextrin, a penetration enhancer), and scraped epithelium tissues of the cornea was explored. Fluorescence microscopy images showed that neither thiolated nor PEGylated nanoparticles penetrated the cornea or epithelium treated with β-cyclodextrin; when the epithelium was removed, only PEGylated (5000 Da) nanoparticles permeated into the stroma.[21] Additionally, mucoadhesion of thiolated and PEGylated (750 and 5000 Da) nanoparticles on porcine urinary bladder mucosa was compared to nonmucoadhesive dextran (negative control) and the well-established mucoadhesive material chitosan (positive control). Following sequential washing with artificial urine, the thiolated nanoparticles were retained on the bladder mucosa for longer periods than dextran but for a shorter time than chitosan. Again, PEGylation significantly reduced mucoadhesion which was correlated with the reduced thiol content. Another study used various poly(2-alkyl-2-oxazoline)s to functionalize thiolated nanoparticles, and penetration of the POZylated nanoparticles with different side chain lengths (methyl, ethyl, and propyl) into gastric mucosa was assessed using fluorescence microscopy. Penetration significantly reduced as the alkyl chain length increased, and POZylation reduced nanoparticle mucoadhesion because of the reduction of their surface thiol group content.[20]

Here, thiolated organosilica nanoparticles were synthesized following the protocol introduced by Irmukhametova et al., with modifications.[5] Particles were produced by self-condensation of MPTS in various solvents (predominantly DMSO) with or without bubbling with atmospheric or enriched oxygen. Reaction conditions also varied monomer concentration, catalyst choice, and concentration and reaction temperature. The resulting nanoparticles were characterized using dynamic light scattering (DLS), transmission electron microscopy (TEM), and zeta-potential measurements. By systematically exploring reaction conditions, the relationship between the resultant particle size and the dielectric constant of the solvent or catalyst concentrations was defined, allowing the rational design of thiolated organosilica nanoparticles with required sizes.

■ EXPERIMENTAL SECTION

Materials. MPTS (95%), *N*-methyl-2-pyrrolidine (NMP), acetonitrile (AcN), trimethylamine (TEA, ≥99%), diethylamine (DEA, ≥99.5%), sodium phosphate dibasic (≥99%), sodium phosphate monobasic dihydrate (≥99%), 5,5′-dithiobis(2-nitrobenzoic acid) (DTNB, ≥98% TLC), and acetone were purchased from Sigma-Aldrich (UK). DMSO, dimethyl formamide (DMF), tetrahydrofuran (THF), and sodium hydroxide pellets were purchased from Fisher Scientific (UK). 1,4-Dioxane (dioxane) was purchased from Acros (UK). Hydrochloric acid solution (1 mol/L) was from Fluka (UK). L-Cysteine hydrochloride anhydrous (98%) was purchased from Alfa Aesar (UK). All materials were used as received.

Synthesis of Thiolated Nanoparticles. Nine different synthetic conditions were used to prepare organosilica nanoparticles:

Effect of Catalyst.

(1) MPTS (0.75 mL; 0.2 mol/L) was mixed with DMSO (20 mL) and 0.5 mL of serial concentrations of NaOH (0.05; 0.1; 0.2; 0.3; 0.5; 0.7; and 0.9 mol/L). The reaction mixtures were left for 24 h at room temperature with air bubbling and continuous stirring.

(2) MPTS (0.75 mL; 0.2 mol/L) was mixed with DMSO (20 mL) and 0.5 mL of serial concentrations of hydrochloric acid (HCl) (0.1; 0.3; and 0.5 mol/L). The reaction mixtures were left for 24 h at room temperature with air bubbling and continuous stirring.

(3) MPTS (0.75 mL; 0.2 mol/L) was mixed with DMSO (20 mL) and 0.5 mL of DEA (0.2 mol/L) and left for 24 h at room temperature with air bubbling and continuous stirring.

(4) MPTS (0.75 mL; 0.2 mol/L) was mixed with DMSO (20 mL) and 0.5 mL of triethylamine (0.2 mol/L) and left for 24 h at room temperature with air bubbling and continuous stirring.

Effect of Monomer Concentration.

(5) Serial volumes of MPTS (0.15; 0.25; 0.5; 0.75; 1.0; and 1.5 mL; 0.04; 0.07; 0.13; 0.2; 0.27; and 0.4 mol/L) were mixed with DMSO (20 mL) and 0.5 mL of 0.5 mol/L NaOH. The reaction mixtures were left for 24 h at room temperature with air bubbling and continuous stirring.

Effect of Solvent.

(6) MPTS (0.75 or 0.38 mL; 0.2 or 0.1 mol/L) was mixed with an organic solvent (20 mL) and 0.5 mL of NaOH (0.5 mol/L) and left for 24 h at room temperature with air bubbling and continuous stirring. The following organic solvents were used: DMF, NMP, AcN, THF, dioxane, and acetone.

Effect of Temperature.

(7) MPTS (0.75 mL; 0.2 mol/L) was mixed with DMSO (20 mL) and 0.5 mL of NaOH (0.5 mol/L) and left for 24 h at 50 °C with air bubbling and continuous stirring.

Effect of Air Bubbling.

(8) MPTS (0.75 mL; 0.2 mol/L) was mixed with DMSO (20 mL) and 0.5 mL of serial concentrations of NaOH (0.05; 0.1; 0.2; 0.3; 0.5; 0.7; and 0.9 mol/L). The reaction mixtures were left for 24 h at room temperature with continuous stirring but no air bubbling.

(9) MPTS (0.75 mL; 0.2 mol/L) was mixed with DMSO (20 mL) and 0.5 mL of NaOH (0.5 mol/L) and left for 24 h at room temperature with enriched oxygen (95% O_2/5% CO_2) bubbling and continuous stirring.

All synthesized nanoparticles were purified by dialysis against deionized water (5 L, eight changes of water) using dialysis tubing with a 12 000−14 000 Da molecular weight cutoff (Medicell Membranes Ltd., UK). The purified aqueous dispersions of the nanoparticles were stored at 4 °C.

DLS and Zeta-Potential Measurements. DLS and zeta-potential measurements were conducted with dilute dispersions of nanoparticles at 25 °C using a Nano-S Zetasizer (Malvern Instruments, UK). Each batch of nanoparticles was synthesized in triplicate, and the analysis was carried out three times for each sample. The mean and standard deviation of particle size, polydispersity, and zeta-potential were calculated.

Transmission Electron Microscopy. TEM images of thiolated nanoparticles were acquired using a JEOL 2010 transmission electron microscope operating at an accelerating voltage of 200 kV. For sample preparation, carbon-coated Cu grids were brought into contact with the aqueous nanoparticle dispersions for 60 s. One sample from each NaOH catalyst concentration was analyzed, and ImageJ software was used to process the images for size measurements. The mean ± standard deviation values of nine measurements were calculated for each sample.

Ellman's Assay. The thiol group content in nanoparticles was determined by Ellman's assay. Before analysis, all nanoparticles were freeze-dried using a Heto Power Dry LL 3000 freeze-drier (Thermo Electron Corporation). The dispersions (0.3 mg/mL) of nanoparticles were prepared in 10 mL of phosphate buffer solution (0.5 mol/L, pH 8) and were allowed to hydrate for 1 h. In the meantime, 3 mg of Ellman's reagent (DTNB) was dissolved in 10 mL of 0.5 mol/L phosphate buffer solution at pH 8. After particle hydration, 500 μL of DTNB solution was added to 500 μL aliquots of the nanoparticle

DOI: 10.1021/acs.langmuir.8b01556
Langmuir 2018, 34, 8347−8354

Scheme 1. Three Main Stages of Nanoparticle Formation and the Proposed Structure of MPTS Nanoparticles

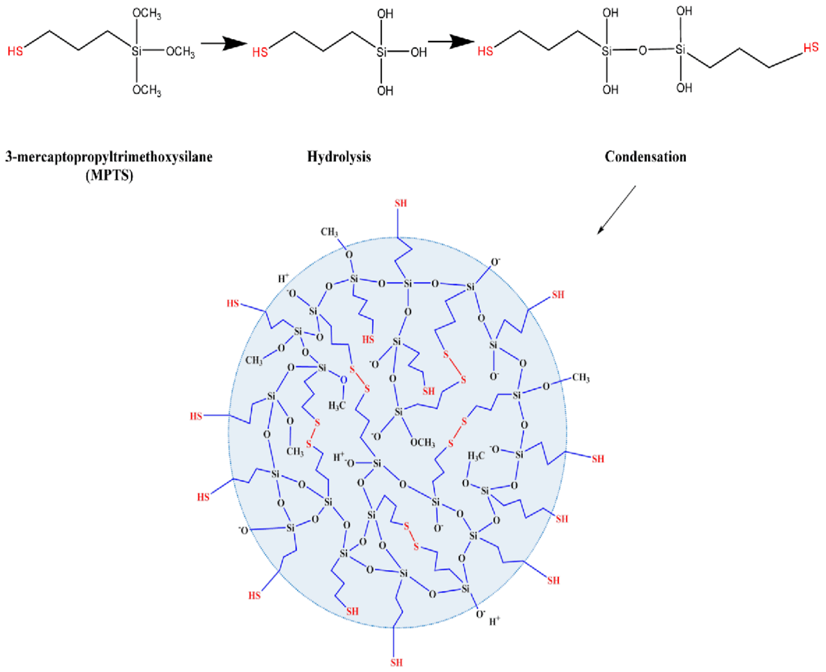

Table 1. Characterization of Thiolated Organosilica Nanoparticles Prepared in DMSO Using 0.2 mol/L MPTS with Varying Concentrations of NaOH Under Continuous Stirring and Air Bubbling

concentration of NaOH, mol/L	size (DLS), nm	PDI	size (TEM), nm	ξ-potential, mV	yield, w/w %	SH content, μmol/g
0.05	291 ± 30	0.151 ± 0.017	586 ± 119	−25 ± 8	2 ± 1	127 ± 52
0.1	193 ± 22	0.114 ± 0.014	100 ± 29	−40 ± 2	8 ± 12	121 ± 54
0.2	161 ± 40	0.162 ± 0.047	78 ± 21	−32 ± 4	24 ± 15	131 ± 49
0.3	59 ± 3	0.090 ± 0.003	35 ± 5	−45 ± 2	40 ± 2	150 ± 39
0.5	50 ± 1	0.134 ± 0.010	27 ± 3	−55 ± 2	49 ± 31	152 ± 55
0.7	47 ± 2	0.162 ± 0.009	22 ± 4	−34± 1	55 ± 28	152 ± 19
0.9	47 ± 5	0.169 ± 0.040	16 ± 3	−35± 12	53 ± 15	113 ± 15

dispersion and incubated in the dark for 90 min. The nanoparticle dispersion was then centrifuged for 10 min at 13 000 rpm (Sanyo, MSE Micro Centaur), and 200 μL of the supernatant was placed in a 96-well microtiter plate. Absorbance was measured at 420 nm with a plate reader (Epoch, BioTek). Thiol concentration was calculated from a calibration curve of cysteine hydrochloride prepared as a series of solutions under the same conditions from 0.004 to 0.634 μmol/mL (Figure S1). The analysis was carried out three times, and the mean ± standard deviation values were calculated.

■ RESULTS AND DISCUSSION

Synthesis of Thiolated Silica Nanoparticles. Thiolated silica nanoparticles were synthesized following the protocol introduced by Irmukhametova et al.,[5] using MPTS as the monomer. The hydrolysis and condensation of the monomer and the proposed structure of MPTS nanoparticles are presented in Scheme 1. As in the protocol, NaOH was the principal catalyst, though others were evaluated as below, and DMSO was the typical solvent,[5] but, again, others were explored. The literature protocol employed air bubbling through the reaction media and again was used here, alongside no air bubbling and bubbling with 95% O_2.

Effect of Catalyst. It was anticipated that, for a defined concentration of MPTS, in a given solvent at a fixed temperature and with air bubbling, increasing the catalyst concentration would decrease the resultant particle size; the results from this study, using NaOH as the catalyst, largely confirmed this expectation as shown in Table 1.

Data from both DLS and TEM (Figures 1 and S2) showed that particle size decreases with increasing concentration of NaOH but to a lower limit. From the DLS analysis, relatively large particles were synthesized using our most dilute 0.05 and 0.1 mol/L NaOH with sizes of ∼290 and ∼195 nm, respectively. Using ≥0.5 up to 0.9 mol/L NaOH did not further reduce the particle size, resulting in the nanoparticles of ∼50 nm (Table 1). Similarly, different concentrations of NaOH (1−5 mmol/L) were used for the synthesis of silica nanoparticles from tetraethoxysilane (TEOS); higher concentrations resulted in the formation of smaller and more uniform particles.[24] Particle size was previously reported to decrease when 2 and 27% NH_4OH catalyzed the synthesis of thiol-organosilica nanoparticles.[2]

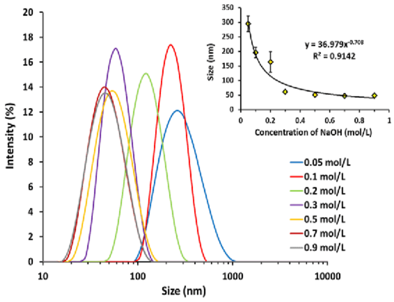

Figure 1. DLS size distributions of particles prepared using different concentrations of NaOH catalyst with 0.2 mol/L MPTS in DMSO. Inset: Relationship between mean (±SD) DLS size of thiolated organosilica nanoparticles and the concentration of NaOH used in the reaction mixture.

A similar trend but with differences in values was seen in the TEM data for the same particles. Unlike DLS, TEM measures the size of the particle per se rather than the particle with its hydration layer, and so smaller particle sizes are typically recorded by electron microscopy. This is evident for the particles produced with 0.1−0.7 mol/L NaOH where the "core" particle size decreases to a lower limit of ∼35 nm, and all sizes are somewhat smaller than the DLS values. However, TEM shows that very large particles are produced with the most dilute catalyst (0.05 mol/L, particles ≈ 586 nm). The images (Figure S2) suggest that these particles are less dense and may result from aggregation of primary particles or poor and/or incomplete synthesis—noting that the yield for this reaction was very low (2%). Interestingly, following an apparent plateau in size with 0.3−0.7 mol/L NaOH, further increase in the catalyst concentration to 0.9 mol/L appears to further reduce the particle size as determined by TEM ($p < 0.05$).

All the nanoparticles carry a net negative zeta-potential, attributed to the presence of Si−O$^-$ and −S$^-$ groups at their surfaces. No clear trend was seen between the zeta-potential and catalyst concentration.

The thiol content on the surface of the nanoparticles was determined using Ellman's assay and ranged from 113 to 152 μmol/g, with a general trend of increasing content per gram with decreasing particle size (and increasing catalyst concentration). This could be due to the availability of a larger number of −SH groups being able to react with Ellman's reagent arising from the increase in surface area per gram of the smaller particles. The yields of nanoparticles prepared using low concentrations of NaOH were relatively poor (2−24%), with higher yield recorded when [NaOH] > 0.2 mol/L.

Alternative catalysts were investigated in the reaction, namely, HCl, DEA, and TEA, using the same protocol (Table S1). Particles obtained using different concentrations of HCl (0.1, 0.3, and 0.5 mol/L) were large (1184, 5309, and 10 460 nm, respectively) with negative zeta-potential and high polydispersity. In contrast, the bases DEA and TEA at 0.2 mol/L produced particles in the same size range (∼250 nm) but statistically significantly larger ($P < 0.05$) than those obtained using NaOH. A reduction in particle size has been reported when the concentration of TEA was reduced in the reaction with TEOS.[11,13,14] In contrast, Shi et al. found that adding more TEA formed smaller particles.[25] This discrepancy may be due to other variations in the reaction conditions including using a different monomer and solvent. It was reported that base-catalyzed condensation-mediated synthesis is faster than acid-catalyzed synthesis as the latter proceeds through hydrolysis and requires an additional step of condensation for nucleation which results in the formation of larger particles.[26,27] Additionally, when NaOH was used instead of NH_4OH as a catalyst in a 1:1 ratio of water and ethanol for synthesizing nanoparticles from TEOS, reaction time reduced 60-fold, and the obtained particles had a greater surface area compared to the particles produced using the conventional Stöber method.[26]

Effect of Monomer Concentration. It was anticipated that, at a fixed catalyst concentration, increasing the monomer concentration would increase the particle size. However, particle size was modified by varying the concentration of the monomer (Table 2); for very dilute starting monomer concentrations (0.04 and 0.07 mol/L), an initial decrease in size with increasing monomer concentration was seen. However, from the DLS size distribution of the lowest concentration (Figure S3), there were two principal particle populations with the majority ≥100 nm and fewer that were 10−20 nm, resulting in a larger mean particle size with wide standard deviation values. As monomer concentration increased, the proportion of smaller to larger particles increased. This could be due to nucleation being restricted at lower concentrations, adsorption of oligomer nuclei on the surface of existing nuclei, or the fusion of several silica nuclei which results in the formation of larger particles.[28−30] Nucleation and growth of nanoparticles from different materials in solutions were reviewed and are highly dependent on the reaction conditions; relatively minor changes may result in different particle growth mechanisms.[31] It was reported that particles prepared using the Stöber method grow by nucleation followed by diffusion-controlled coalescence.[31,32] Subsequently, it was reported that particle growth by the Stöber method was by continuous nucleation of primary particles simultaneously with their aggregation.[31,33] Here, with monomer concentrations ≥ 0.13 mol/L, the particle size increased with increasing monomer concentration. There was a significant difference in size between the larger particles obtained using both a very low concentration of MPTS (0.04 mol/L, $P < 0.05$) and 10 times that concentration (0.4 mol/L, $P < 0.01$) when compared to particles prepared using our "standard" 0.2 mol/L MPTS or indeed for MPTS concentrations between the extremes (Figure 2). All nanoparticles had negative zeta-potentials (−14 to −45 mV) with relatively low

Table 2. Characterization of Thiolated Organosilica Nanoparticles Prepared in DMSO Using 0.5 mol/L NaOH and by Varying the Concentrations of MPTS with Continuous Stirring and Air Bubbling

concentration of MPTS, mol/L	size (DLS), nm	PDI	ξ-potential, mV	yield, w/w %
0.04	113 ± 22	0.620 ± 0.031	−41 ± 2	40 ± 10
0.07	51 ± 30	0.638 ± 0.248	−42 ± 2	53 ± 1
0.13	38 ± 1	0.361 ± 0.053	−46 ± 5	24 ± 4
0.2[a]	50 ± 1	0.134 ± 0.010	−55 ± 2	49 ± 31
0.27	63 ± 2	0.154 ± 0.015	−35 ± 30	48 ± 10
0.40	120 ± 16	0.102 ± 0.025	−13 ± 23	18 ± 6

[a] Data for 0.2 mol/L MPTS taken from Table 1.

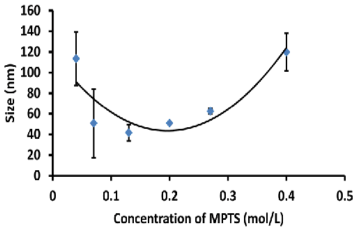

Figure 2. Mean ± SD, DLS sizes of particles prepared using various concentrations of MPTS compared to the standard protocol using 0.2 mol/L MPTS (0.04 mol/L, $P < 0.05$, 0.27 mol/L, $P < 0.01$, 0.4 mol/L, $P < 0.01$).

yields (18−50%), and wide polydispersities (0.640−0.360) were seen at lower MPTS concentrations.

Nakamura et al. used different concentrations of MPTS, (3-mercaptopropyl)triethoxysilane, and (3-mercaptopropyl)-methyldimethoxysilane to prepare silica nanoparticles, alongside TEOS. The nanoparticles were synthesized by the Stöber method using 65% ethanol with water and either 2 or 27% ammonium hydroxide. Their results showed that using 27% NH_4OH was optimal for thiol-organosilica nanoparticle synthesis when compared to TEOS and that particle size increased with increasing the concentration of the thiol-organosilica source. However, the time for complete formation of the nanoparticles varied (between 1 and 3 days) and was dependent on the synthetic conditions and concentration of the monomer and catalyst.[2,3] In our case, we report a similar increase in particle size with increasing monomer concentration, from 0.13; 0.2; 0.27 to 0.4 mol/L of MPTS in DMSO. However, our data also show that there is a lower limit to the size-related effects of the silica source concentration and that with very low concentrations of MPTS (0.04; 0.07 mol/L), particle size decreases with the increasing monomer concentration.

Effect of Solvent. Our standard protocol synthesizes nanoparticles from DMSO.[5] Here, we additionally used various organic aprotic solvents with different dielectric constants to determine the influence on resultant particle sizes, charge, and thiol content. Although aprotic solvents were reported to not "formally" take part in sol−gel reactions, they may influence the reaction kinetics by increasing the strength of nucleophiles or decreasing the strength of electrophiles. Additionally, aprotic solvents were reported to promote base-catalyzed condensation as they hydrogen bond to electrophilic protonated silanols.[27] The growth of the primary particles, their aggregation, and the size of secondary particles are all dependent on the thermodynamic parameters of the system which control the colloidal stability.[34] The general characteristics of the organosilica nanoparticles synthesized in different organic solvents, with other reaction conditions fixed, are shown in Table 3.

With all seven solvents, the resultant particles gave invariant and, as expected, negative zeta-potentials because of the presence of the negatively charged Si−O^- and S^- groups on their surface. Thiol contents when synthesized from DMSO, DMF, and NMP were also invariant though preparing particles from AcN gave lower thiol content; yields from other solvents were too low to allow analysis. It was reported that dielectric constant affects particle size at the nucleation stage; higher dielectric constants provide greater static repulsive force between the particles than the van der Waals attractive force, preventing gathering of the nuclei and thus resulting in smaller particle formation.[35] Our data accord with this and show that particle size is strongly dependent on the dielectric constant of the solvent; the higher the dielectric constant, the smaller the particle size, as illustrated in Figure 3.

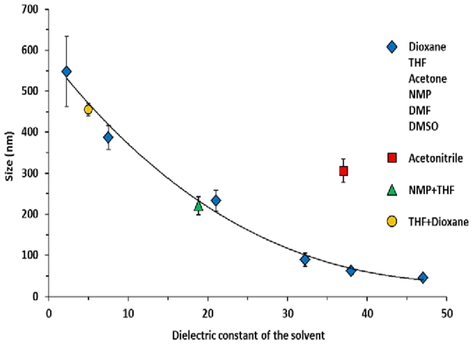

Figure 3. DLS size of organosilica nanoparticles synthesized in different organic solvents as a function of the solvent's dielectric constant; solvents from left to right: dioxane, THF, acetone, NMP, DMF, and DMSO; $y = -0.0015x^3 + 0.3508x^2 - 24.8x + 585.35$; $R^2 = 0.9894$.

Further, the veracity of the relationship in Figure 3 was explored to determine if particle size could be rationally designed by selecting the dielectric constant of the aprotic solvent. Dielectric constants were selected by mixing NMP with THF and THF with dioxane, calculated by

$$d(x + y) = \frac{md(x) + nd(y)}{m + n} \qquad (1)$$

Table 3. Characterization of Organosilica Nanoparticles Synthesized in Different Organic Solvents (20 mL), 0.2 mol/L MPTS, and 0.5 mL of 0.5 mol/L NaOH with Continuous Stirring and Air Bubbling

solvent	solvent's dielectric constant	size (DLS), nm	PDI	ξ-potential, mV	Yield, w/w %	SH content, μmol/g
DMSO	47.00	45 ± 3	0.181	−55 ± 7	58.6 ± 0.4	249 ± 30
DMF	38.00	62 ± 8	0.513	−53 ± 6	27.1 ± 2.6	227 ± 60
AcN	37.00	306 ± 28	0.108	−60 ± 13	10.7 ± 4.2	68 ± 16
NMP	32.20	99 ± 16	0.552	−63 ± 4	22.0 ± 1.5	203 ± 122
acetone	21.00	233 ± 25	0.120	−53 ± 6	3.0 ± 1.5	[a]
THF	7.50	387 ±± 29	0.219	−64 ± 5	5.6 ± 1.5	[a]
dioxane	2.25	548 ± 86	0.120	−64 ± 13	7.3 ± 5.5	[a]

[a] Ellman's assay was not performed because of very low yields.

where d is the dielectric constant of a solvent; x and y are solvents 1 and 2; and m and n are the number of moles of solvents 1 and 2, respectively. The ratio of the solvents was 1:1 (v/v), and the total volume was 20 mL. The dielectric constant of 1:1 THF/dioxane was 4.94, which according to the relationship in Figure 3 was expected to provide particles of 471 nm; experimental results provided the material with a diameter of 455 ± 16 nm. The NMP/THF mixture, with a dielectric constant of 18.8 was predicted to generate materials of 233 nm with the experimental data in accord at 221 ± 22 nm. Further details can be found in Table S3.

As with the thiol content, preparing particles from AcN appears as an outlier and does not fit with the trend of smaller particles resulting from solvents with higher dielectric constants. AcN can be hydrolyzed in the presence of a strong aqueous base such as sodium hydroxide, essentially changing the dielectric constant of the solvent and, importantly, reducing the effective catalyst concentration; larger particles were formed with lower NaOH concentrations as shown in Table 1.[36]

In addition, AcN containing 0.1 mol/L tetra-*n*-butylammonium perchlorate was shown to impact on molecular oxygen diffusivity and did not follow the Stokes−Einstein relationship because of the smaller size of molecular oxygen compared to the solvent molecules.[37] Moreover, AcN was reported to be a poor anion-solvating medium compared to DMSO.[38] As oxygen is necessary for our nanoparticle production, these findings may also partially explain the larger-than-predicted particle sizes from this solvent.

von Storp et al. reported that using solvents with higher dielectric constants led to smaller protein nanoparticles. Although other processing conditions such as stirring rate and continuous addition of the desolating agent affected the human serum albumin nanoparticles, the authors showed that particle size could be predicted from the dielectric constant of the desolvation medium.[39] Although the mechanisms of nanoparticle production vary between our organosilica materials and protein-based nanoparticles, both are determined by the solvent dielectric constant and generate materials with lower sizes in the region of 50 nm.

It has been reported that using an aprotic cosolvent formed spherical silica nanoparticles (Figure 4b).[13] TEM images showed that our thiolated nanoparticles tend to self-assemble into chains and clusters because of the formation of disulfide bridges (Figure 4a).

Effect of Temperature. Reaction temperature affects the size and dispersity of nanoparticles.[34] Synthesis was performed using our "standard" protocol (20 mL DMSO, 0.2 mol/L MPTS, and 0.5 mL of 0.5 mol/L NaOH with continuous stirring and air bubbling) but at 50 °C with the resultant particles significantly larger and more polydisperse [70 ± 1 nm, polydispersity index (PDI) 0.188 ± 0.029] than particles prepared at room temperature (50 ± 1 nm, PDI 0.134 ± 0.010). Similarly, Möller et al., using TEOS as the silica precursor and TEA as the catalyst, reported a doubling in particle diameter when the reaction temperature was raised from 60 to 80 °C.[6,11] Nakamura et al. also reported the dependence of particle size on the reaction temperature, alongside other factors such as monomer concentration as described above; larger particles were formed with higher concentrations of MPTS when temperature was increased.[2,3] However, a decrease in the size of particles produced by the Stöber method was reported as the temperature increased to 60 °C, beyond which temperature−size dependence was lost. This effect can be related to the production of a smaller number of nuclei at lower temperatures due to the change in hydrolysis rate. It was reported that varying the reaction temperature may change the viscosity and evaporation of ammonia or alcohol from the reaction mixture at an elevated temperature.[34,40]

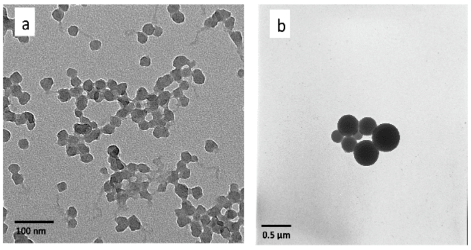

Figure 4. TEM images for organosilica nanoparticles synthesized in DMSO (a) and AcN (b).

Effect of Air Bubbling. Our particles are typically prepared in the presence of atmospheric oxygen to facilitate the oxidation of some thiol groups and formation of disulfide bridges. In addition, oxygen promotes the nucleation of primary particles and allows the particles to reach the stop-growth phase in a shorter time; turbidity increased when the reaction mixture was bubbled with air, indicating the formation of colloidal particles.[5] Here, two batches of particles were prepared with serial concentrations of NaOH with and without air bubbling. Characterization of these particles is summarized in Table S2. When the reaction mixture was bubbled with air, smaller particles resulted with higher concentrations of the catalyst (i.e., ≥0.3 mol/L) compared to lower catalyst concentrations, as described previously. Without air bubbling, when the catalyst concentration was >0.3 mol/L (shown above to generate small and invariant particle sizes, Table 1), larger particles tended to form in the absence of oxygen, as shown in Figure 5. In addition to the role played by air bubbling in facilitating oxidation and formation of disulfide bridges, it may also provide more efficient stirring of the reaction mixture.

Given the anomalous particles produced from AcN discussed above and solvents' effects on oxygen diffusivity, particles were prepared in AcN in the presence and absence of air bubbling. Again, larger particles were produced in the absence of oxygen (416 ± 13 nm) compared to those formed in the presence of air bubbling (306 ± 28 nm).

Further, as bubbling the reaction mixture with atmospheric air decreases particle size, bubbling with an oxygen-enriched gas (95%:5%) O_2/CO_2 was evaluated. Surprisingly, upon dialysis of the resultant product, a gel formed (Figure S3), probably from the aggregation of the nanoparticles due to excessive formation of disulfide bridges.

■ CONCLUSION

The effects of synthetic conditions on the characteristics of thiol-organosilica particles were studied. Different catalysts produce particles with variable size ranges with smallest particles obtained when NaOH was selected. Increasing either the monomer concentration or reaction temperature increased the resultant particle size. Solvents with higher dielectric constants produced smaller particles, and the experimental

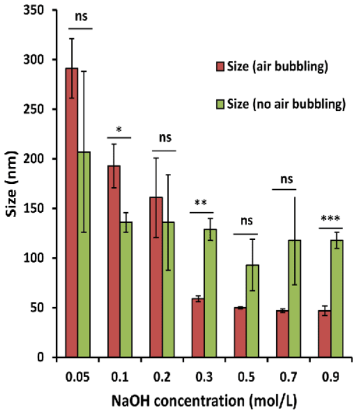

Figure 5. DLS size of particles prepared using serial concentrations of NaOH, 0.2 mol/L MPTS, with continuous stirring, with and without air bubbling at room temperature.

relationship was validated to demonstrate that specified particle sizes can be produced by manipulating the dielectric constant of the solvent with other conditions fixed. DMSO was selected as the base solvent as particles produced had the appropriate and consistent size, polydispersity, and thiol content. Using this, bubbling the reaction mixture with atmospheric air promoted nucleation of primary particles and allowed the particles to reach the stop-growth phase in a shorter time, resulting in the formation of smaller particles. Further enrichment of the reaction media with oxygen generated a gel due to excessive cross-linking. Our results demonstrate that, by selection and manipulation of reaction conditions including monomer concentration, catalyst type and concentration, reaction temperature and oxygenation, and thiolated organosilica particles can be designed with a defined particle size. Studies into the internal structure of the nanoparticles synthesized under various synthetic conditions will be of interest in the future.

■ ASSOCIATED CONTENT

Ⓢ Supporting Information

The Supporting Information is available free of charge on the ACS Publications website at DOI: 10.1021/acs.langmuir.8b01556.

Calibration curve for Ellman's assay; TEM images for nanoparticles prepared by varying the concentration of NaOH; DLS distributions for particles prepared using 0.04 and 0.07 mol/L of MPTS, 0.5 mol/L NaOH, and DMSO; tables with the values of sizes, zeta-potentials, yields, and thiol content for particles prepared using different catalysts and different concentrations of NaOH; characteristics of organic solvent mixtures and size (calculated vs actual) of organosilica nanoparticles synthesized in those mixtures; and images of gels formed when the reaction mixture was bubbled with 95%:5% O_2/CO_2 (PDF)

■ AUTHOR INFORMATION

Corresponding Author

*E-mail: v.khutoryanskiy@reading.ac.uk. Phone: +44(0)118 378 6119. Fax: +44(0)118 378 4644.

ORCID

Vitaliy V. Khutoryanskiy: 0000-0002-7221-2630

Notes

The authors declare no competing financial interest.

■ REFERENCES

(1) Nakamura, M.; Ishimura, K. Synthesis and Characterization of Organosilica Nanoparticles Prepared from 3-Mercaptopropyltrimethoxysilane as the Single Silica Source. *J. Phys. Chem. C* **2007**, *111*, 18892−18898.

(2) Nakamura, M.; Ishimura, K. One-Pot Synthesis and Characterization of Three Kinds of Thiol−Organosilica Nanoparticles. *Langmuir* **2008**, *24*, 5099−5108.

(3) Nakamura, M.; Ozaki, S.; Abe, M.; Doi, H.; Matsumoto, T.; Ishimura, K. Size-controlled synthesis, surface functionalization, and biological applications of thiol-organosilica particles. *Colloids Surf., B* **2010**, *79*, 19−26.

(4) Wang, L.; Zhao, W.; Tan, W. Bioconjugated silica nanoparticles: development and applications. *Nano Research* **2008**, *1*, 99.

(5) Irmukhametova, G. S.; Mun, G. A.; Khutoryanskiy, V. V. Thiolated Mucoadhesive and PEGylated Nonmucoadhesive Organosilica Nanoparticles from 3-Mercaptopropyltrimethoxysilane. *Langmuir* **2011**, *27*, 9551−9556.

(6) Tang, F.; Li, L.; Chen, D. Mesoporous Silica Nanoparticles: Synthesis, Biocompatibility and Drug Delivery. *Adv. Mater.* **2012**, *24*, 1504−1534.

(7) Schulz, A.; McDonagh, C. Intracellular sensing and cell diagnostics using fluorescent silica nanoparticles. *Soft Matter* **2012**, *8*, 2579−2585.

(8) Vivero-Escoto, J. L.; Huxford-Phillips, R. C.; Lin, W. Silica-based nanoprobes for biomedical imaging and theranostic applications. *Chem. Soc. Rev.* **2012**, *41*, 2673−2685.

(9) Rahman, I. A.; Padavettan, V. Synthesis of silica nanoparticles by sol-gel: Size-dependent properties, surface modification, and applications in silica-polymer nanocomposites - a review. *J. Nanomater.* **2012**, *2012*, 132424.

(10) Yamada, H.; Urata, C.; Ujiie, H.; Yamauchi, Y.; Kuroda, K. Preparation of aqueous colloidal mesostructured and mesoporous silica nanoparticles with controlled particle size in a very wide range from 20 nm to 700 nm. *Nanoscale* **2013**, *5*, 6145−6153.

(11) Möller, K.; Kobler, J.; Bein, T. Colloidal Suspensions of Nanometer-Sized Mesoporous Silica. *Adv. Funct. Mater.* **2007**, *17*, 605−612.

(12) Slowing, I. I.; Vivero-Escoto, J. L.; Trewyn, B. G.; Lin, V. S.-Y. Mesoporous silica nanoparticles: structural design and applications. *J. Mater. Chem.* **2010**, *20*, 7924−7937.

(13) Wu, S.-H.; Mou, C.-Y.; Lin, H.-P. Synthesis of mesoporous silica nanoparticles. *Chem. Soc. Rev.* **2013**, *42*, 3862−3875.

(14) Yamamoto, E.; Kuroda, K. Colloidal Mesoporous Silica Nanoparticles. *Bull. Chem. Soc. Jpn.* **2016**, *89*, 501−539.

(15) Li, L.; Liang, R.; Li, Y.; Liu, H.; Feng, S. Hybrid thiol-ene network nanocomposites based on multi(meth)acrylate POSS. *J. Colloid Interface Sci.* **2013**, *406*, 30−36.

(16) Li, L.; Liu, H. Rapid Preparation of Silsesquioxane-Based Ionic Liquids. *Chem.—Eur. J.* **2016**, *22*, 4713−4716.

(17) Nakamura, M.; Miyamoto, K.; Hayashi, K.; Awaad, A.; Ochiai, M.; Ishimura, K. Time-lapse fluorescence imaging and quantitative single cell and endosomal analysis of peritoneal macrophages using fluorescent organosilica nanoparticles. *Nanomedicine* **2013**, *9*, 274−283.

(18) Irmukhametova, G. S.; Fraser, B. J.; Keddie, J. L.; Mun, G. A.; Khutoryanskiy, V. V. Hydrogen-bonding-driven self-assembly of PEGylated organosilica nanoparticles with poly(acrylic acid) in

aqueous solutions and in layer-by-layer deposition at solid surfaces. *Langmuir* **2012**, *28*, 299−306.

(19) Štorha, A.; Mun, E. A.; Khutoryanskiy, V. V. Synthesis of thiolated and acrylated nanoparticles using thiol-ene click chemistry: towards novel mucoadhesive materials for drug delivery. *RSC Adv.* **2013**, *3*, 12275−12279.

(20) Mansfield, E. D. H.; de la Rosa, V. R.; Kowalczyk, R. M.; Grillo, I.; Hoogenboom, R.; Sillence, K.; Hole, P.; Williams, A. C.; Khutoryanskiy, V. V. Side chain variations radically alter the diffusion of poly(2-alkyl-2-oxazoline) functionalised nanoparticles through a mucosal barrier. *Biomater. Sci.* **2016**, *4*, 1318−1327.

(21) Mun, E. A.; Morrison, P. W. J.; Williams, A. C.; Khutoryanskiy, V. V. On the barrier properties of the cornea: a microscopy study of the penetration of fluorescently labeled nanoparticles, polymers, and sodium fluorescein. *Mol. Pharm.* **2014**, *11*, 3556−3564.

(22) Mun, E. A.; Williams, A. C.; Khutoryanskiy, V. V. Adhesion of thiolated silica nanoparticles to urinary bladder mucosa: Effects of PEGylation, thiol content and particle size. *Int. J. Pharm.* **2016**, *512*, 32−38.

(23) Bernkop-Schnurch, A. Thiomers: a new generation of mucoadhesive polymers. *Adv. Drug Delivery Rev.* **2005**, *57*, 1569−1582.

(24) Dingsøyr, E.; Christy, A. A. Effect of reaction variables on the formation of silica particles by hydrolysis of tetraethyl orthosilicate using sodium hydroxide as a basic catalyst. *Prog. Colloid Polym. Sci.* **2000**, *116*, 67−73.

(25) Chen, Y.; Chen, H.-R.; Shi, J.-L. Construction of Homogenous/Heterogeneous Hollow Mesoporous Silica Nanostructures by Silica-Etching Chemistry: Principles, Synthesis, and Applications. *Acc. Chem. Res.* **2014**, *47*, 125−137.

(26) Bhakta, S.; Dixit, C. K.; Bist, I.; Jalil, K. A.; Suib, S. L.; Rusling, J. F. Sodium hydroxide catalyzed monodispersed high surface area silica nanoparticles. *Mater. Res. Express* **2016**, *3*, 075025.

(27) Brinker, C. J.; Scherer, G. W. Hydrolysis and condensation II: Silicates. *Sol−Gel Science: The Physics and Chemistry of Sol−Gel Processing*; Academic Press Limited: London, 1990; p 908.

(28) Dixit, C. K.; Bhakta, S.; Kumar, A.; Suib, S. L.; Rusling, J. F. Fast nucleation for silica nanoparticle synthesis using a sol-gel method. *Nanoscale* **2016**, *8*, 19662−19667.

(29) Ding, T.; Yao, L.; Liu, C. Kinetically-controlled synthesis of ultra-small silica nanoparticles and ultra-thin coatings. *Nanoscale* **2016**, *8*, 4623−4627.

(30) Carcouët, C. C. M. C.; van de Put, M. W. P.; Mezari, B.; Magusin, P. C. M. M.; Laven, J.; Bomans, P. H. H.; Friedrich, H.; Esteves, A. C. C.; Sommerdijk, N. A. J. M.; van Benthem, R. A. T. M.; de With, G. Nucleation and growth of monodisperse silica nanoparticles. *Nano Lett.* **2014**, *14*, 1433−1438.

(31) Thanh, N. T. K.; Maclean, N.; Mahiddine, S. Mechanisms of Nucleation and Growth of Nanoparticles in Solution. *Chem. Rev.* **2014**, *114*, 7610−7630.

(32) Pontoni, D.; Narayanan, T.; Rennie, A. R. Time-Resolved SAXS Study of Nucleation and Growth of Silica Colloids. *Langmuir* **2002**, *18*, 56−59.

(33) Green, D. L.; Lin, J. S.; Lam, Y.-F.; Hu, M. Z.-C.; Schaefer, D. W.; Harris, M. T. Size, volume fraction, and nucleation of Stober silica nanoparticles. *J. Colloid Interface Sci.* **2003**, *266*, 346−358.

(34) Plumeré, N.; Ruff, A.; Speiser, B.; Feldmann, V.; Mayer, H. A. Stöber silica particles as basis for redox modifications: Particle shape, size, polydispersity, and porosity. *J. Colloid Interface Sci.* **2012**, *368*, 208−219.

(35) Wang, H.-C.; Wu, C.-Y.; Chung, C.-C.; Lai, M.-H.; Chung, T.-W. Analysis of Parameters and Interaction between Parameters in Preparation of Uniform Silicon Dioxide Nanoparticles Using Response Surface Methodology. *Ind. Eng. Chem. Res.* **2006**, *45*, 8043−8048.

(36) Wang, Z.; Richter, S. M.; Rozema, M. J.; Schellinger, A.; Smith, K.; Napolitano, J. G. Potential Safety Hazards Associated with Using Acetonitrile and a Strong Aqueous Base. *Org. Process Res. Dev.* **2017**, *21*, 1501−1508.

(37) Li, Q.; Batchelor-McAuley, C.; Lawrence, N. S.; Hartshorne, R. S.; Compton, R. G. Anomalous solubility of oxygen in acetonitrile/water mixture containing tetra-n-butylammonium perchlorate supporting electrolyte; the solubility and diffusion coefficient of oxygen in anhydrous acetonitrile and aqueous mixtures. *J. Electroanal. Chem.* **2013**, *688*, 328−335.

(38) Vasudevan, D.; Wendt, H. Electroreduction of oxygen in aprotic media. *J. Electroanal. Chem.* **1995**, *392*, 69−74.

(39) von Storp, B.; Engel, A.; Boeker, A.; Ploeger, M.; Langer, K. Albumin nanoparticles with predictable size by desolvation procedure. *J. Microencapsulation* **2012**, *29*, 138−146.

(40) Tan, C. G.; Bowen, B. D.; Epstein, N. Production of monodisperse colloidal silica spheres: Effect of temperature. *J. Colloid Interface Sci.* **1987**, *118*, 290−293.

Supporting information

Controlling the size of thiolated organosilica nanoparticles

*Jamila H. Al Mahrooqi, Ellina A. Mun, Adrian C. Williams, Vitaliy V. Khutoryanskiy**

Reading School of Pharmacy, University of Reading, Reading, RG6 6AD, United Kingdom

Corresponding author: v.khutoryanksiy@reading.ac.uk

Figures: 4
Tables: 3

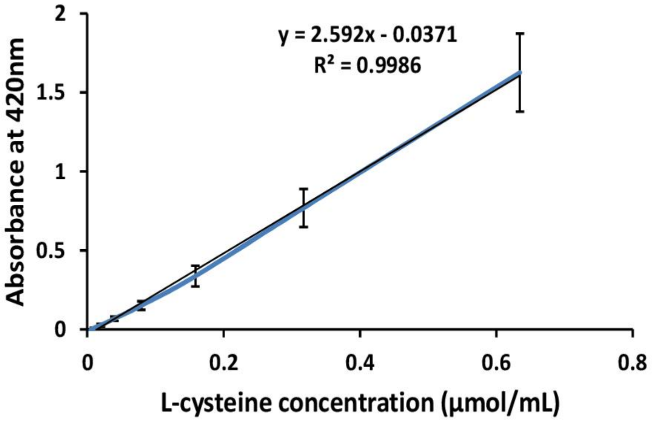

Figure S1: Calibration curve for Ellman's assay, performed with L-cysteine hydrochloride solution.

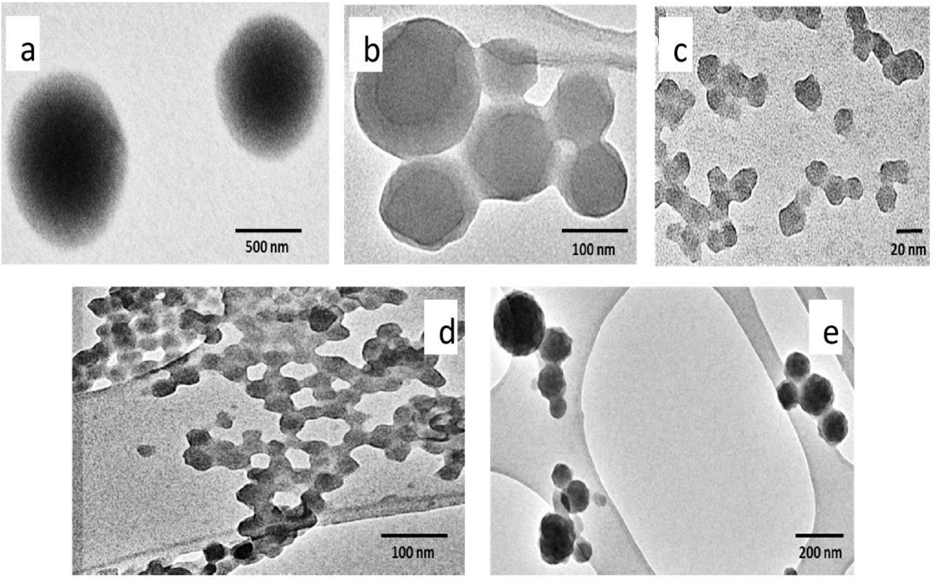

Figure S2: TEM images for nanoparticles prepared by varying the concentration of NaOH (a) 0.05 (b) 0.1 (c) 0.5 (d) 0.3 (e) 0.2 mol/L.

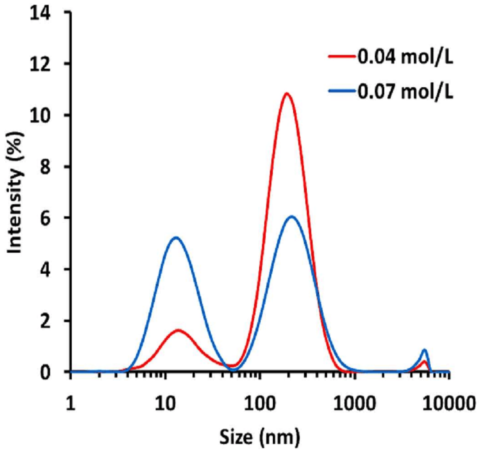

Figure S3: Dynamic light scattering distribution for particles prepared using 0.04 and 0.07 mol/L of MPTS, 0.5 mol/L NaOH and DMSO.

Table S1: Characterization of particles obtained using different catalysts, 0.2 mol/L MPTS and DMSO.

Catalyst, mol/L	Size, nm	PDI	ξ-Potential, mV
HCl 0.1	1184± 484	0.536± 0.322	-37± 6
HCl 0.3	5309± 10260	0.750± 0.290	-13± 13
HCl 0.5	10460± 19497	0.829± 0.306	-48± 14
$C_4H_{11}N$ 0.2	246 ± 23	0.355± 0.031	-44 ± 4
$C_6H_{15}N$ 0.2	243 ± 90	0.371± 0.067	-22 ± 14

Table S2: Characterization of nanoparticles prepared using serial concentrations of NaOH, 0.2 mol/L MPTS and DMSO without air bubbling.

Concentration of NaOH, mol/L	Size (DLS), nm	PDI	ξ-Potential, mV	SH content, µmol/g	Yield, w/w %
0.05	207± 81	0.144±0.073	-33± 5	-	9± 6
0.1	136± 10	0.031±0.016	-33± 1	-	29± 15
0.2	136± 48	0.080±0.037	-40± 5	62 ± 33	60± 28
0.3	129± 11	0.072±0.019	-36± 2	63 ± 35	58± 22
0.5	93± 26	0.136±0.069	-34± 3	110 ± 116	25± 17
0.7	118± 45	0.108±0.041	-35± 2	71 ± 40	48± 12
0.9	118± 8	0.113±0.019	-33± 2	67 ± 35	51± 8

Table S3: Characteristics of organic solvent mixtures and size (calculated vs. actual) of organosilica nanoparticles synthesised in those mixtures.

Solvent mixture	Molecular weight (MW), g/mol		Density (ρ), g/mL		Number of moles (v), mol		Dielectric constant		Dielectric constant of solvent mixture	Predicted (calculated) size. nm	Actual size ± SD, nm
	Solvent 1	Solvent 2	Solvent 1	Solvent 2	Solvent 1	Solvent 2	Solvent 1	Solvent 2			
NMP+THF	99	72	1.028	0.889	0.104	0.123	32.2	7.5	18.8	233	221±22
THF +Dioxane	72	88	0.889	1.033	0.123	0.117	7.5	2.25	4.94	471	455±16

Figure S4: Gel formation when reaction mixture was bubbled with 95%:5% O2: CO2.

Chapter 3

Thiolated and PEGylated silica nanoparticle delivery to hair follicles

Thiolated silica nanoparticles were modified with PEG 750 Da and 5000 Da. The penetration of thiolated and PEGylated nanoparticles into the hair follicles is discussed in this chapter.

This chapter was published as Al Mahrooqi, J., Khutoryanskiy, V. and Williams, A., (2021). Thiolated and PEGylated silica nanoparticle delivery to hair follicles. *International Journal of Pharmaceutics*, 593, p.120130.

International Journal of Pharmaceutics 593 (2021) 120130

Contents lists available at ScienceDirect

International Journal of Pharmaceutics

journal homepage: www.elsevier.com/locate/ijpharm

Thiolated and PEGylated silica nanoparticle delivery to hair follicles

Jamila H. Al Mahrooqi, Vitaliy V. Khutoryanskiy, Adrian C. Williams*

Reading School of Pharmacy, University of Reading, Reading RG6 6AD, UK

A R T I C L E I N F O

Keywords:
Follicular targeting
Nanoparticles
Silica
PEGylation
Skin

A B S T R A C T

Targeting drug delivery to hair follicles is valuable to treat conditions such as alopecia's and acne, and this shunt route may also allow drug delivery to deeper skin layers and the systemic circulation by avoiding the intact stratum corneum. Here, we investigated the effects of nanoparticle surface chemistry on their delivery into hair follicles by synthesizing fluorescent thiolated silica nanoparticles and functionalizing with 750 Da and 5000 Da methoxypolyethylene glycol maleimide (PEG). The stability of the nanoparticles in skin homogenate was verified before tape stripping of porcine-dosed tissue showed the distribution of the free fluorescent dye and different nanoparticles in the skin. Analysis of microscopic images of the skin sections revealed penetration of nanoparticles functionalized with PEG into the appendages whereas thiolated nanoparticles stayed on the surface of the skin and were removed by tape stripping. Nanoparticles functionalized with PEG 5000 Da penetrated deeper into the hair follicles compared to counterparts functionalized with PEG 750 Da. PEGylation can thus enhance targeted delivery of nanoparticulates into hair follicles.

1. Introduction

The remarkable barrier properties of human skin are largely attributed to the outermost layer of the epidermis, the stratum corneum (Brown and Williams, 2019; Labouta and Schneider, 2013). Appendages including the hair follicles and eccrine glands cross the epidermis and originate in the underlying dermis. Given the stratum corneum barrier, it is well established that typically only relatively small molecular weight and lipophilic drugs are able to be delivered effectively via the transdermal route to clinically efficacious levels, though some recent studies have shown that macromolecules such as aptamers may be able to enter the tissue (Lenn et al., 2018). However, the use of nanoparticles for drug delivery into or through the skin has also been studied using quantum dots, carbon nanotubes, metal and metal oxide nanoparticles, dendrimers, and lipid based nanoparticles (Jensen et al., 2011; Kraeling et al., 2018; Küchler et al., 2009).

Nanoparticulate dosing of skin tends to focus on two mechanisms of delivery. Firstly, the potential delivery of the nanosystem into intact stratum corneum (and deeper epidermal layers) with studies exploring the effects of physicochemical properties of the nanosystems including their size, shape, charges and surface properties (Labouta et al., 2011a; Labouta and Schneider, 2013; Lademann et al., 2011). Other factors considered include the nanoparticle vehicle and the disease state of the skin or stratum corneum barrier impairment (for example during wound healing) (Brown and Williams, 2019; Larese et al., 2009; Vogt et al., 2016; Wu et al., 2009). Secondly, the nanoparticles may be delivered into the appendages (pilosebaceous unit and eccrine and apocrine ducts). Though varying from site to site (Otberg et al., 2004) the appendage openings represent approximately 0.1% of the skin surface area and provides a shunt route to the lower layers of the skin by circumventing the intact surface stratum corneum (Brown and Williams, 2019; Raber et al., 2014). The follicles have been targeted with nanoparticles to treat conditions such as alopecia and acne, and alternatively to deposit a reservoir of a drug to permeate into deeper skin layers or the systemic circulation.

Particle deposition into a hair follicle is usually stimulated *in vivo* by hair movement and (as with *in vitro* studies) by massage. Further, the cuticles on the surface of the hair shaft form a zigzag structure which acts as a geared pump that, with hair movement, can push nanoparticles deeper into the hair follicles. Clearance of nanoparticles from the follicle depends primarily on sebum production and hair growth, both relatively slow processes allowing the follicle to serve as a reservoir; when particles were applied, their clearance from the hair follicle was over a period of 10 days (Knorr et al., 2009; Lademann et al., 2009; Raber et al., 2014). More specifically within the hair follicle, the infundibulum generally provides the reservoir compartment whereas sebaceous glands are associated with acne and androgenetic alopecia and the bulge region holds a reservoir for keratinocyte stem cells (Knorr et al., 2009; Patzelt

---

* Corresponding author.
E-mail address: a.c.williams@reading.ac.uk (A.C. Williams).

https://doi.org/10.1016/j.ijpharm.2020.120130
Received 6 October 2020; Received in revised form 23 November 2020; Accepted 25 November 2020

et al., 2011).

However, the optimal nanoparticle properties for deposition into hair follicles are unclear and variations are also seen with delivery vehicle; Mathes et al. reported greater follicular deposition of particles from aqueous dispersions compared to when suspended in a hydrogel and that follicular uptake can thus be controlled by the choice of vehicle or carrier used to deliver a drug (Mathes et al., 2016). Patzelt et al. (2011) compared the depth of penetration into hair follicles of different sizes (122, 230, 300, 470, 643, and 860 nm) of two types of nanoparticles, PLGA (poly-lactide-*co*-glycolid) and silica. Both types showed similar size-dependent penetration, increasing in depth as size rose to 643 nm, but the silica nanoparticles penetrated deeper than the PLGA particles. It had been proposed that the geared pump effect from hair shaft movement is optimal when the particles are similar size to the hair cuticles – in the region of 500 nm (Lademann et al., 2009; Patzelt et al., 2011). However, Vogt et al. reported deeper penetration of 40 nm nanoparticles along the follicular duct of human vellus hair and through the follicular epithelium, whereas 750 and 1500 nm nanoparticles aggregated in the infundibulum with no penetration to deeper layers or through viable epidermis (Vogt et al., 2006).

Varied nano-particulate systems have been evaluated for controlled drug delivery within hair follicles, ranging from liposomes and polymersomes to solid lipid nanoparticles and nano-vesicles. Commonly seeking to treat alopecias, examples include oleic acid and phosphatidylcholine nano-vesicles containing minoxidil which increased deposition of the drug in the follicles 10-fold compared to a gel formulation (Kumar et al., 2018). Minoxidil has also been incorporated into liposomes (e.g. Jain et al., 2010), solid lipid nanoparticles (Padois et al., 2011) and into nanoparticles formed from PLGA (Takeuchi et al., 2018) – as has finasteride (Roque et al. 2017). The use of nano-sized delivery systems to target hair follicles in alopecia, along with consideration of the anatomy and pathophysiology of the condition, has recently been reviewed (Salim and Kamalasanan, 2020). Nanocarriers have also been used for glucocorticoids such as clobetasol propionate for inflammatory scalp conditions. To mitigate both systemic and local adverse effects when applied topically, a range of clobetasol-loaded polymeric nanocarriers were evaluated (nanospheres, nanocapsules, lipid-core nanocapsules) to balance drug release, interfollicular permeation and follicular uptake (Schiedel et al., 2015). Significantly greater levels of drug were found in the follicles from the nanocarriers compared to application of the free drug and, importantly, the study demonstrated that not only was the carrier important but also that massaging the tissue resulted in greater follicular uptake, in agreement with the above.

PEGylation is widely used to improve stability, tolerance and delivery to various tissues including eyes, urinary bladder, and nasal tissue (Porfiryeva et al., 2020). We have previously shown that PEGylation of nanoparticles reduces their mucoadhesion and improves their diffusivity (Irmukhametova et al., 2011; Mun et al., 2014b; Mun et al., 2016; Ways et al., 2018). However, nanoparticles with thiol groups on their surface are expected to stay bound to the skin surface and hair as they are rich in keratin. Polyacrylic acid was modified with sulfhydryl moieties to improve its binding to the skin, resulting in a 15-fold increase in adhesion compared to unmodified polymer (Laffleur and Bernkop-Schnürch, 2018). Likewise, thiolation of silicone oil enhanced adhesion to skin in comparison to commonly used silicone oils (Partenhauser et al., 2016). Here, we used tape striping to study the follicular deposition of two types of silica nanoparticles with different surface chemistry and sizes, thiolated and PEGylated (750 and 5000 Da) silica nanoparticles. The particles were fluorescently labelled with 5-iodoacetamido fluorescein and follicular uptake was investigated *in vitro* using pig flank skin.

2. Material and methods

2.1. Materials

3-mercaptopropyltrimethoxysilane (MPTS 95%), maleimide terminated methoxy poly(ethylene glycol) (PEG molecular weight 750 & 5000 Da), sodium phosphate dibasic (≥99%), sodium phosphate monobasic dihydrate (≥99%), 5- (iodoacetamido)fluorescein, sodium fluorescein, and 5,5′-dithiobis(2- nitrobenzoic acid) (DTNB, ≥98% TLC), were purchased from Sigma-Aldrich (UK). DMSO, sodium hydroxide pellets and Slide-A-Lyzer minidialysis devices, 3.5 kDa MWCO, were purchased from Fisher Scientific (UK). L-Cysteine hydrochloride anhydrous (98%) was purchased from Alfa Aesar (UK). Dialysis membrane with a molecular weight cut-off 12–14 kDa was purchased from Medicell International Ltd. (UK). D-Squame Standard Sampling Discs and D-Squame® disc applicator was purchased from Clinical and Derm (USA). All materials were used as received. Fresh newborn (<1 month old) pig flank skin was obtained from the Pirbright Institute (UK) and was frozen immediately after collection until use.

2.2. Synthesis and characterization of thiolated silica nanoparticles:

Thiolated silica nanoparticles were synthesised according to a previously published method (Irmukhametova et al., 2011). Briefly, 20 mL DMSO and 0.5 mL of 0.5 M NaOH solution were added to 0.75 mL MPTS. The mixture was stirred continuously with air bubbling for 24 h at room temperature. The nanoparticles were purified by dialysis against deionized water (5 L, eight changes of water) using dialysis membrane. The purified aqueous dispersions of the nanoparticles were stored at 4 °C.

2.3. Synthesis of fluorescently-labelled thiolated silica nanoparticles:

Thiolated silica nanoparticles were labelled with 5-(iodoacetamido) fluorescein (5-IAF) by adding 3 mg of 5-IAF to 12 mL aqueous dispersions of thiolated nanoparticles. The amount of fluorophore used was calculated with respect to molar ratio so that 5 μmol of fluorophore is added to 50 μmol of sulfhydryl groups of nanoparticles. The reaction mixture was stirred for 16 h at room temperature protected from light. Fluorescently-labelled nanoparticles were then purified by dialysis against deionized water in the dark (5 L, eight changes of water), according to the above protocol (Irmukhametova et al., 2011).

2.4. Pegylation of fluorescently-labelled nanoparticles

5 mL aqueous dispersions of fluorescently-labelled nanoparticles were mixed with 100 mg of methoxypolyethylene glycol maleimide of two molecular weights (750 or 5000 Da). The reaction mixture was stirred for 16 h at room temperature protected from light, resulting in the formation of PEGylated silica nanoparticles. PEGylated nanoparticles were purified by dialysis in the dark as above (Mun et al., 2014b).

3. Characterization of nanoparticles

DLS and ζ-potential measurements were conducted with dilute dispersions of nanoparticles at 25 °C using a Nano-S Zetasizer (Malvern Instruments, UK). Each batch of nanoparticles was synthesized in triplicate, and the analysis was carried out three times for each sample. The mean and standard deviation of particle size, polydispersity, and ζ-potential were calculated. The thiol group content in nanoparticles was determined by Ellman's assay according to a previously published method (Al Mahrooqi et al., 2018).

3.1. Stability study

The stability of the fluorescent label on the nanoparticles for use in skin studies was evaluated by adding the nanoparticles to skin homogenate and dialysing against phosphate buffered saline (PBS) to assess the release of free dye. Briefly, 2 g of pig skin was cut into small pieces and homogenised in 15 mL of PBS at 6500 rpm for 1 min in an ice bath using

Table 1

Characterization of thiolated and PEGylated silica nanoparticles, n = 3, values presented as mean ± standard deviation. *The calibration curve used to calculate free thiol content is shown in Figure S2.

Nanoparticle	Size (nm)	PDI	ζ-potential (mV)	Concentration (mg/mL)	Free thiol content (μmol/g)*
Thiolated	62 ± 3	0.207 ± 0.015	−47 ± 3	15 ± 1	289 ± 14
PEGylated 750 Da	79 ± 1	0.214 ± 0.011	−42 ± 3	12 ± 1	144 ± 21
PEGylated 5000 Da	89 ± 1	0.169 ± 0.010	−30 ± 2	20 ± 2	142 ± 2

an Ultra Turrax T18 high speed homogenizer (Lau et al., 2013). Four different samples were prepared by mixing 1.5 mL of the labelled nanoparticles, unlabelled nanoparticles, sodium fluorescein and homogenate respectively with 1.5 mL of homogenate (total 3 mL) and dialysed against PBS. The samples were placed on a rolling plate with continuous shaking at 37 °C to ensure continuous mixing and movement of the dialysate. The fluorescence intensity of the dialysate was assessed using a fluorescent spectrophotometer after 1, 6, 24, 48, and 72 h of incubation. The experiment was performed in triplicate and data were analysed using GraphPad Prism 8 software.

3.2. *Tape stripping study*

Pig flank skin was thawed at room temperature and hair was carefully shaved to avoid damaging the stratum corneum before use. Test areas were demarked using a permanent marker around a 2.5 × 2.5 cm polyethylene template. A finite dose of fluorescently labelled nanoparticles (50 μL, so 8 μL cm^{-2}) was applied and the area gently massaged in a circular movement for one minute using a gloved fingertip. The dosed tissue was then left for 2 h at room temperature, protected from light. D-Squame® adhesive discs were used for tape stripping; each disc was pressed firmly against the skin using a D- Squame® disc applicator with a constant pressure of 225 g/cm^2 for 5 sec. The marked area was stripped sequentially twenty times with the direction of stripping alternating for each strip. After each strip, both the adhesive disc containing the removed layer of stratum corneum and the remaining skin sample were analysed using a Leica MZ10 F stereomicroscope (Leica Microsystems, UK) with an ET-GFP filter to quantify the presence of fluorescent nanoparticles and show their distribution. All images were taken with an exposure time of 80 mS, gain 2, gamma 1 and wavelength 520 nm. Images were further analysed using ImageJ software (National Institutes of Health, USA) and normalised with the following equation:

$$\text{Fluorescenceintensity} = \frac{I - I_b}{I_0 - I_b} \times 100$$

where I is the fluorescence intensity of the nanoparticle-dosed skin sample or disc after each tape stripping and I_o is the initial fluorescence intensity of the sample following dosing, massage and incubation but prior to any tape stripping. I_b is the background fluorescence intensity of the disc or skin; to allow each individual tissue sample to act as its own background fluorescence control (Ways et al., 2018), and recognising that this may change the sequential removal of the stratum corneum, background fluorescence was measured after each tape stripping of non-dosed skin samples using the same protocol as above.

In addition, each adhesive disc was weighed before and after tape stripping in order to determine the fraction of the barrier removed or relative depth (x/L); where x is the thickness removed divided by the total stratum corneum thickness (L) and so relative depth within the stratum corneum varies between 0 (at the skin surface) to 1 at the interface with the viable epidermis (Russell and Guy, 2012). Each disc was then centrifuged in 5 mL PBS at 3500 rpm for 10 min before the fluorescence intensity of the extract was assayed using a fluorescence spectrophotometer (Cary Eclipse, Varian Inc., US) at 494 nm excitation and an emission spectral range of 500–600 nm.

The tape stripped skin area was then excised and placed on a weighing boat with the epidermis facing upwards and fully covered with OCT embedding medium and placed in dry ice. The frozen sample was stored at −80 °C before tissue cross sectioning at −20 °C using a Bright 5040 cryostat microtome (Bright Instruments Ltd., Luton, UK). Tissue was placed perpendicularly to the cutting blade (i.e. tissue cut from dermis to outer surface) to avoid dislocation of the nanoparticles from outside into deeper skin layer (Labouta et al., 2011a, 2011b). Cross-sections (10 μm) were placed on microscopic slides and imaged using a Zeiss Axio Imager fluorescence microscope (Carl Zeiss, Jena, Germany). The samples were excited with a 488 nm filter in order to locate the labelled nanoparticles and with a DAPI filter to view the tissue. The two images were merged using Carl Zeiss software and analysed by ImageJ software.

4. Results and discussion

4.1. *Synthesis and characterization*

Thiolated silica nanoparticle were synthesized by hydrolysis and self-condensation of 3-mercaptopropyltrimethoxysilane (MPTS) in the aprotic solvent dimethyl sulfoxide (DMSO) in contact with air, with NaOH as the catalyst. Sub-100 nm cross-linked nanoparticles are formed through Si-O-Si and disulfide bonds. The nanoparticles were labelled with 5-IAF, where the iodoacetamide moiety of the fluorophore reacts with the sulfhydryl group in the nanoparticles. Fluorescently labelled nanoparticles were then PEGylated and both labelled thiolated and PEGylated silica nanoparticles were used in all experiments. It has been reported that a high grafting density of lower molecular weight PEG and decorating particles with PEG 5000 Da provide rapid mucus penetrating properties, whereas, nanoparticles became mucoadhesive when coated with PEG 10000 Da (Wang et al., 2008). Therefore, PEG 750 and 5000 Da were chosen for our experiments.

The resulting nanoparticles significantly ($P < 0.05$) increased in size in the order thiolated < PEGylated 750 Da < PEGylated 5000 Da and they all had a narrow polydispersity index (PDI; Table 1 and Figure S1) and negative ζ-potential values due to the presence of thiol groups at their surface. Following PEGylation, the nanoparticles' ζ-potential values reduced due to the polymer coupling with some of the free thiol on the surface of the nanoparticles, with the greater decrease seen for the larger molecular weight PEG also partially attributed to some charge shielding effects. Indeed, the Ellman's assay showed a statistically significant ($P < 0.005$) difference in free thiol content between thiolated and the PEGylated nanoparticles, and no significant difference between PEGylated 750 and 5000 Da particles. The reduction in thiol content and increase in particle size indicates successful PEGylation of the nanoparticles (Table 1), but clearly these particles retain some free thiol groups at their surface – approximately 50% of those seen in the parent thiolated material. Nanoparticle concentrations were determined by freeze-drying 1 mL of nanoparticle suspensions and determining the weight of the solid residue. This concentration was used to calculate free thiol content before and after PEGylation.

4.2. *Stability of nanoparticles in skin homogenate*

The skin possesses both enzymatic and non-enzymatic detoxification systems including glutathione (GSH) as an antioxidant (Connor and Wheeler, 1987) which acts as a direct free radical scavenger and

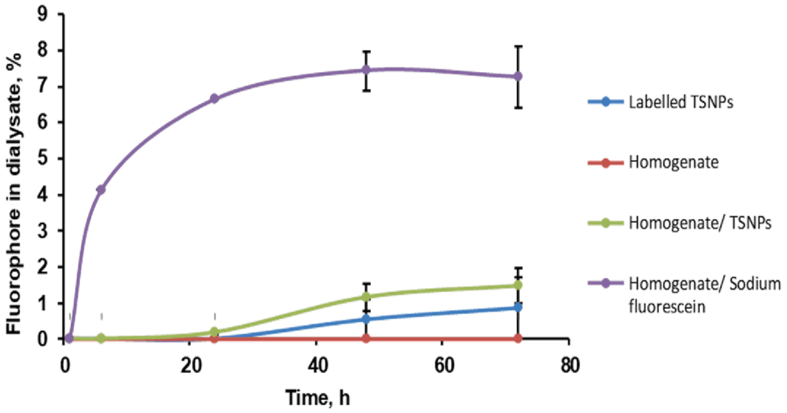

Fig. 1. The release of fluorescent dye across the dialysis membrane. Labelled TSNP = fluorophore release from labelled silica nanoparticles in buffer; Homogenate = homogenate alone to test for autofluorescence; Homogenate/ TSNP's = fluorophore release from labelled silica nanoparticles in skin homogenate; Homogenate/Sodium fluorescein is the positive control of the fluorescent dye with homogenate. Study at 37 °C, samples taken at 1, 6, 24, 48, 72 h, n = 3, values are presented as mean ± standard error of mean.

quenches radicals by hydrogen atom donation resulting in the formation of glutathione disulphide (GSSG). However, as the reduced form of GSH is essential for cutaneous photo-protection, GSSG is recycled to GSH by GSH-reductase with hydrogen donation by nicotinamide adenine dinucleotide phosphate (NADPH). This process is extremely fast due to the high activity of the enzyme and it takes less than one minute to restore all cutaneous GSH (Connor and Wheeler, 1987). It was anticipated that nanomaterials with disulfide bonds are susceptible to degradation by GSH (Cui et al., 2012; Hayashi et al., 2016; Prasetyanto et al., 2016; Yang et al., 2016; Zhang et al., 2012; Zhou et al., 2017), and so the stability of the fluorescent label attached to the nanoparticle core before further decoration with PEG was investigated in skin homogenate. The release of fluorescent dye from the fluorescent thiolated silica nanoparticles was examined in the phosphate buffer ("labelled TSNP's") and in skin homogenate, alongside assays of sodium fluorescein with skin homogenate as a positive control and the homogenate alone to detect auto-fluorescence; the homogenate showed no detectable auto- fluorescence during the study. The release of the fluorophore was measured over time (Fig. 1) and sodium fluorescein was detected in the dialysate at 6 h (4%) and reached (11%) at 72 h. The labelled particles showed a similar release profile when incubated in either buffer of skin homogenate with very low fluorescence first detected after 24 h and no significant differences in release in these two media ($p > 0.05$). Release of sodium fluorescein across the dialysis membrane from the positive control was significantly greater than release from the nanoparticles ($p < 0.05$).

Doura et al. (2019) demonstrated that MPTS nanoparticles were resistant to GSH-induced degradation and retained their spherical shape. In their experiments, they prepared various hybrid thiol-organosilica nanoparticles from different proportions of 3-mercaptopropyltrimethoxysilane (MPTS) and 3- mercaptopropyldimethoxymethylsilane (MPDMS) and detected the ratio of disulphide bonds to thiol groups in each sample by Raman spectroscopy. They investigated the degradability of the nanoparticles in 10 and 40 mM of GSH, compared with nanoparticles prepared from MPTS or MPDMS alone. They found that increasing the ratio of MPDMS increased the susceptibility to degradation by GSH. They also found that the introduction of MPDMS into nanoparticles prepared from MPTS induced the formation of disulfide bonds which was proportional to the ratio of MPDMS constituent (Doura et al., 2019). In our study, the particles produced from MPTS likewise showed no significant degradation in the skin homogenate. Further, both labeled and unlabeled nanoparticles were stored for up to 6 months and no flocculation or aggregation was observed, again in agreement with previous studies using similar nanoparticles (Ways et al., 2018).

4.3. Tape stripping study

Eq. (1) was used to quantify the fluorescence intensity of the skin and tape strips, and relies on subtraction of background fluorescence (I_b). Prior to dosing, we investigated the effects or tape stripping skin on the background fluorescence of the tissue. The experiments (in triplicate) showed a gradual reduction in the background intensity with tape stripping such that after 20 strips, the background intensity had fallen by a mean of 12%. These values were used for the background intensities in subsequent dosed studies.

Tape stripping is increasingly used for bioavailability and bioequivalence studies (Herkenne et al., 2008; Pensado et al., 2019). However, specific study protocols vary, for example in cutting or shortening the hair prior to experimentation (Jensen et al., 2011; Klang et al., 2011; Nagelreiter et al., 2015; Patzelt et al., 2011). Here, the hair was shaved since preliminary studies showed that our nanoparticles bound strongly to shortened hair bristles even after 20 tape stripping (Figure S3 a) but binding was reduced with PEGylated nanoparticles (Figure S3 b &c). Keratin is rich in disulfide bonds and thiolated silica nanoparticles interact covalently with hair keratin (Bragulla and Homberger, 2009; Cruz et al., 2017a, 2017b; Gniadecka et al., 1998; Williams et al., 1994). PEGylation of the thiolated particles reduces the free thiol groups in the particle shell by about 50% (Table1) and may also screen remaining thiol groups on the particle surface. A similar trend with mucoadhesion to different tissues was reported where mucoadhesive properties of the thiolated silica nanoparticles were significantly decreased by PEGylation and penetration was improved (Irmukhametova et al., 2011; Mun et al., 2014b; Ways et al., 2018).

Significant reductions ($P < 0.05$) in fluorescence intensity of all tested nanoparticles and sodium fluorescein was evident after 2 h of incubation on the skin surface and prior to tape stripping. The fluorescence intensity reduced to 12, 52, 7 and 10% for sodium fluorescein, TSNPs, PEGylated 750 Da and PEGylated 5000 Da TSNPs respectively which could be attributed to quenching of fluorescein (Glasgow, 2016; Song et al., 1995) and penetration into the follicles. Teichmann et al. reported recovery of 95% of sodium fluorescein dye from stratum corneum and 5% from follicular infundibula after differential stripping (Teichmann et al., 2005). The penetration of sodium fluorescein solution into stratum corneum has also been compared with that when loaded into PEGylated lipid nanocarriers (Rangsimawong et al., 2016). In another study, Zhang et al. used transmission electron microscopy to study PEG-coated quantum dots applied to skin and reported localization within the lipid bilayers of the stratum corneum. This was attributed to the soft coating of PEG which enabled the quantum dots to enter the intercellular lipid matrix of the stratum corneum although this is unlikely the case for our larger PEGylated nanoparticles (Zhang et al., 2008). It is notable that a far larger proportion of the fluorescence

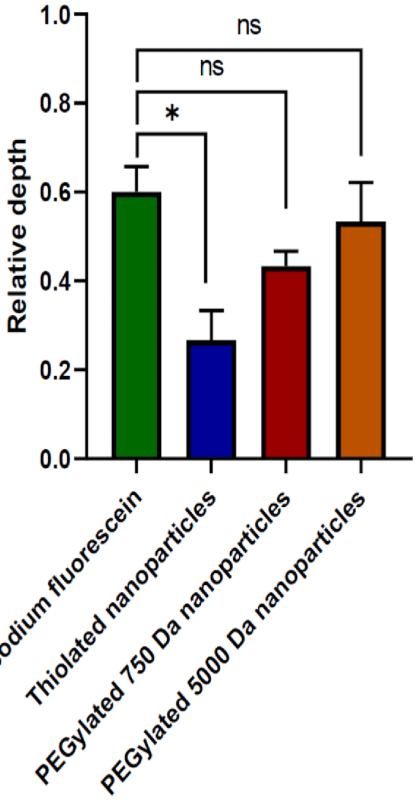

Fig. 2. Penetration depth of sodium fluorescein, TSNPs, PEGylated (750 & 5000 Da) TSNPs into the removed stratum corneum layers, n = 3, $P < 0.05$, values are presented mean ± standard error of mean calculated using one-way ANOVA and Bonferroni post-hoc tests.

remained at the skin surface 2 h post-dosing of the thiolated silica nanoparticles (prior to tape stripping). Fourier transform Raman and infrared vibrational analysis of the stratum corneum demonstrated the presence of disulphide bonds in proteins (Barry et al., 1992; Gniadecka et al., 1998) and the keratins that form the stratum corneum are relatively soft and contain little cysteine compared to hair (Williams et al., 1994). Retention of the thiolated silica nanoparticles on the skin surface is thus likely attributable to the formation of disulphide bonds with the outer hair shaft and, to a lesser extent, stratum corneum keratins.

We used spectroscopic and gravimetric analysis to generate nanoparticle distribution profiles as a function of stratum corneum depth (Figure S4). By assuming that the density of stratum corneum and area stripped are constant and knowing the weight of stratum corneum removed, the mass of sample removed can be related to tissue depth (Higo et al., 1993). The distribution profiles only showed significant differences between thiolated silica nanoparticles and sodium fluorescein ($p < 0.05$) and no significant differences between either of the PEGylated particles or the thiolated material (Fig. 2). Sodium fluorescein has been reported to readily penetrate into the stratum corneum but less well into the deeper layers of the epidermis (Rangsimawong et al., 2016). Here, we see a reproducible penetration gradient down to approximately 60% of the stratum corneum thickness for the free dye (Fig. 2). In contrast, there is no strong evidence for penetration of any of the nanoparticles into the intact stratum corneum with almost all particles removed by the second tape strip. Some fluorescence was seen but is attributed to particles remaining bound to the surface of the skin, held in skin furrows or adhered to the upper hair follicle and so were not removed by tape strips (Figure S4).

Fluorescent microscope images of skin sections were taken to visualize the location of nanoparticles and clearly demonstrated their binding to hair follicles (Fig. 3). The thiolated silica nanoparticles (Fig. 3a) can be seen to adhere to the skin surface and external surface of the hair follicle as well as reside in a skin furrow. The images show no evidence for penetration into the deeper skin layers, in agreement with the results obtained from the tape strips. Sodium fluorescein penetrated into the hair follicles and analysis of the skin section images revealed a mean maximal penetration depth of 700 μm (Fig. 3b). PEGylated nanoparticles penetrated into the hair follicles to a mean maximal depth of 450 μm and 1400 μm for PEGylated 750 Da (Fig. 3c) and 5000 Da (Fig. 3d) nanoparticles respectively.

Analysis of the images (12 images for each sample with three measurements for each image) revealed significant differences in particle penetration into the hair follicles with PEGylated 5000 Da nanoparticles penetrating deepest followed by sodium fluorescein, PEGylated 750 Da nanoparticles and the fully thiolated materials penetrated least into the follicle ($p < 0.0005$) (Fig. 4).

Sodium fluorescein is a low molecular weight compound (376 Da) that was shown above to penetrate into the stratum corneum, in accord with literature reports. This water-soluble dye was also reproducibly seen at a depth of 700 μm within the follicles, in the infundibulum and in the region of the sebaceous gland; Knorr et al. and Patzelt et al. reported that the sebaceous gland is located ~ 600 μm to 900 μm deep within the terminal hair follicle (Knorr et al., 2009; Patzelt et al., 2011). As expected, the thiolated particles penetrated least well into the follicles, again attributed to their binding to keratin of the hair. PEGylation of these particles enhanced their deposition into the follicles compared to the parent thiolated materials with the PEG 750 nanoparticles penetrating to a mean maximal depth of 450 μm, again in the infundibulum above the sebaceous gland. However, the particles decorated with larger molecular weight PEG penetrated deeper, to 1400 μm and close to the bulge region of the hair follicle (Vogt et al., 2007).

Others have similarly demonstrated the value of PEGylation for enhancing drug delivery. A silica core/PEG shell nanocomposite promoted uptake into MCF-7 breast cancer cells (Slowing et al., 2007). Liposomes loaded with calcipotriol were coated with variable concentrations of PEG to enhance their stability and increased penetration into the skin in comparison to non-PEGylated counterparts. Whilst PEG increased hydration of the stratum corneum by binding to water molecules resulting in enhanced permeability of the stratum corneum, variability in penetration of PEG coated calcipotriol liposomes was also attributed to the PEG conformation on the liposome surface (Knudsen et al., 2012). Deposition of gold nanorods decorated with PEG has also been studied in skin (Mahmoud, 2017) and were shown to penetrate into the follicular compartments but to a lesser extent than hydrophobic gold nanorods. However, after 24 h, accumulation of PEGylated gold nanorods in deeper skin layers was significantly higher than for other gold nanorod systems with the authors suggesting that *trans*-follicular diffusion was facilitated by the polymers hydrophilic properties.

Our results illustrate that deposition into hair follicles is not solely by passive diffusion. Both the free dye and the PEGylated particles are hydrophilic and so diffusion theory would predict that the small molecular weight free drug would diffuse considerably faster than the nanoparticles. Penetration of the particles into the hair follicles is stimulated by movement of the hair, achieved by massaging the tissue in this study. The geared pump effect from hair shaft movement, described earlier, can carry particles deep within the follicle and it is notable that our largest nanoparticles, with PEG 5000 (89 nm diameter), penetrated deeper than the smaller PEG 750 material (79 nm diameter); it was suggested that particles closest in size to the hair cuticles ~ 500 nm) would be driven deepest into the follicles (Lademann et al., 2009; Patzelt et al., 2011). Further, upwards flow of sebum secreted from sebaceous gland can act as both a physical and chemical barrier for nanoparticle diffusion (Knorr et al., 2009; Lademann et al., 2009). Though this study

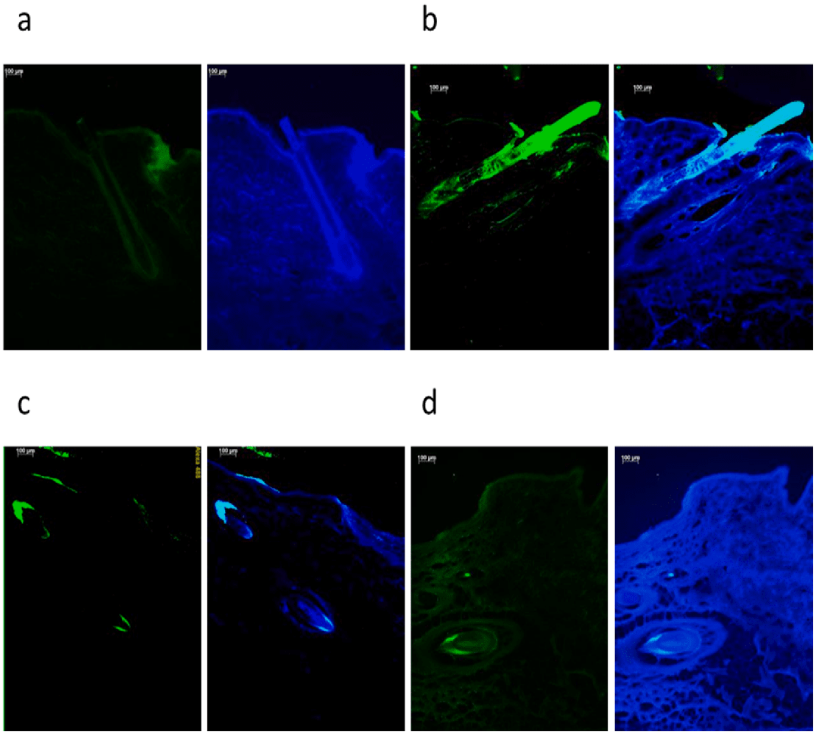

Fig. 3. Exemplar fluorescence microscope images of tape stripped pig skin sections (10 µm thick) after application of thiolated nanoparticles (a), sodium fluorescein (b), PEGylated 750 Da nanoparticles (c) and PEGylated 5000 Da nanoparticles (d). For each set, the first image uses an Alexa 488 nm (green) filter to show only the nanoparticles and the second image merges this with a DAPI (blue) filter to visualise the nanoparticles with the skin background. Scale bar 100 µm. (For interpretation of the references to colour in this figure legend, the reader is referred to the web version of this article.)

used excised skin, it is likely that residual sebum within the follicle provided an additional hydrophobic barrier to penetration of the dye and particles.

The significantly different penetration depths of the two PEGylated particles are unlikely to result solely from the differences in their sizes. We have previously studied the diffusion of these nanoparticles in aqueous polymer solutions and water (Mun et al., 2014a). As expected, factors affecting diffusion of the nanoparticles were their size, the medium viscosity and the presence of interactions between the nanoparticles and the medium components. PEGylating nanoparticles enhanced their diffusivity in pure water, despite the size increase caused by functionalization, and this was attributed to the lubricating effect of PEG shell. PEGylation also reduced nanoparticle mucoadhesion to various tissues including the eye, the urinary bladder and nasal mucosa, again due a reduction in the exposed thiol groups on the particle surface which reduced binding, as seen here (Irmukhametova et al., 2011; Mun et al., 2014b; Ways et al., 2018). With reduced binding capacity, these particles also penetrated deeper in tissue. It was reported that PEG < 2000 Da forms short chains with loss of flexibility compared to when molecular weight is > 2000 Da (Owens and Peppas, 2006). In our studies, PEG forms a soft shell on the surface of the nanoparticles which reduces the number of thiol groups exposed to bind with keratin and so facilitates particle penetration into the hair follicles. Moreover, deeper penetration into the follicles of the PEGylated 5000 Da nanoparticles compared to 750 Da PEG particles is due to the greater flexibility and length of PEG chains which can further enclose and shield the thiol groups of the silica nanoparticles.

5. Conclusions

This study has demonstrated that nanoparticles can be designed to penetrate to defined depths within hair follicles. Thiolated nanoparticles bind to keratin and are localized on the skin surface and near to the skin surface in the hair follicle. When decorated with polyethylene glycol, approximately half the thiol groups are removed from the particle surface and so binding to keratin is greatly reduced. Nanoparticles functionalized with higher molecular weight PEG (5000 Da) penetrated deeper into the follicles, to near the bulge region, than those with lower molecular weight PEG (750 Da) on their surface. The longer PAG chains are more flexible than their shorter counterparts and are better able to shield the remaining thiol groups on the particle surface and so allows deeper penetration by reducing particle-tissue binding. By manipulating the length of the PEG chain, it is feasible to targeted drug delivery to regions of the hair follicle.

CRediT authorship contribution statement

Jamila H. Al Mahrooqi: Conceptualization, Resources, Writing - review & editing, Supervision. **Vitaliy V. Khutoryanskiy:** Validation, Formal analysis, Investigation, Writing - original draft, Funding acquisition. **Adrian C. Williams:** Conceptualization, Methodology, Resources, Writing - review & editing, Supervision, Project administration.

Declaration of Competing Interest

The authors declare that they have no known competing financial interests or personal relationships that could have appeared to influence the work reported in this paper.

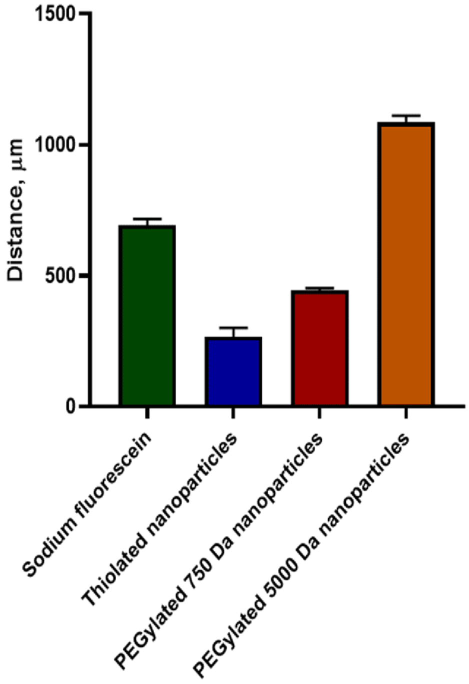

Fig. 4. Depth of penetration into the hair follicles, n = 12, all results are significantly different from each other ($P < 0.0005$), values are presented mean ± standard error of mean calculated using one-way ANOVA and Bonferroni post-hoc tests.

Acknowledgements

We are thankful to Ministry of Higher Education, Research and Innovation, Sultanate of Oman, for a PhD scholarship for Jamila Al Mahrooqi. We acknowledge the assistance of staff at Chemical Analysis Facility (CAF) and SBS Research Microscopy Facilities, University of Reading in fluorescence spectroscopy and fluorescence microscopy. We are grateful to Dr. Mark Henstock, The Pirbright Institute for providing pig skin used in this research.

Appendix A. Supplementary material

Supplementary data to this article can be found online at https://doi.org/10.1016/j.ijpharm.2020.120130.

References:

Al Mahrooqi, J.H., Mun, E.A., Williams, A.C., Khutoryanskiy, V.V., 2018. Controlling the size of thiolated organosilica nanoparticles. Langmuir. 34, 8347–8354. https://doi.org/10.1021/acs.langmuir.8b01556.

Barry, B.W., Edwards, H.G.M., Williams, A.C., 1992. Fourier transform Raman and infrared vibrational study of human skin: Assignment of spectral bands. J. Raman Spectrosc. 23, 641–645. https://doi.org/10.1002/jrs.1250231113.

Bragulla, H.H., Homberger, D.G., 2009. Structure and functions of keratin proteins in simple, stratified, keratinized and cornified epithelia. J. Anat. 214, 516–559. https://doi.org/10.1111/j.1469-7580.2009.01066.x.

Brown, M.B., Williams, A.C., 2019. The Art and Science of Dermal Formulation Development. CRC Press, Florida.

Connor, M.J., Wheeler, L.A., 1987. Depletion of cutaneous glutathione by ultraviolet radiation. Photochem. Photobiol. 46, 239–245. https://doi.org/10.1111/j.1751-1097.1987.tb04762.x.

Cruz, C.F., Martins, M., Egipto, J., Osório, H., Ribeiro, A., Cavaco-Paulo, A., 2017.

Cruz, C.F., Martins, M., Egipto, J., Osório, H., Ribeiro, A., Cavaco-Paulo, A., 2017b. Changing the shape of hair with keratin peptides. RSC Adv. 7 (81), 51581–51592. https://doi.org/10.1039/C7RA10461H.

Cui, Y., Dong, H., Cai, X., Wang, D., Li, Y., 2012. Mesoporous silica nanoparticles capped with disulfide-linked PEG gatekeepers for glutathione-mediated controlled release. ACS Appl. Mater. Interfaces. 4, 3177–3183. https://doi.org/10.1021/am3005225.

Doura, T., Nishio, T., Tamanoi, F., Nakamura, M., 2019. Relationship between the glutathione-responsive degradability of thiol-organosilica nanoparticles and the chemical structures. J. Mater. Res. 34, 1266–1278. https://doi.org/10.1557/jmr.2018.501.

Glasgow, B.J., 2016. Fluorescence lifetime imaging microscopy reveals quenching of fluorescein within corneal epithelium. Exp. Eye Res. 147, 12–19. https://doi.org/10.1016/j.exer.2016.04.008.

Gniadecka, M., Nielsen, O.F., Christensen, D.H., Wulf, H.C., 1998. Structure of water, proteins, and lipids in intact human skin, hair, and nail. J. Invest.

Hayashi, K., Maruhashi, T., Nakamura, M., Sakamoto, W., Yogo, T., 2016. One-pot synthesis of dual stimulus-responsive degradable hollow hybrid nanoparticles for image-guided trimodal therapy. Adv. Funct. Mater. 26, 8613–8622. https://doi.org/10.1002/adfm.201603394.

Herkenne, C., Alberti, I., Naik, A., Kalia, Y.N., Mathy, F.X., Préat, V., Guy, R.H., 2008. In vivo methods for the assessment of topical drug bioavailability. Pharm. Res. 25, 87–103. https://doi.org/10.1007/s11095-007-9429-7.

Higo, N., Naik, A., Bommannan, D.B., Potts, R.O., Guy, R.H., 1993. Validation of reflectance infrared spectroscopy as a quantitative method to measure percutaneous absorption in vivo. Pharm. Res. 10, 1500–1506. https://doi.org/10.1023/A:1018987612155.

Irmukhametova, G.S., Mun, G.A., Khutoryanskiy, V.V., 2011. Thiolated mucoadhesive and PEGylated nonmucoadhesive organosilica nanoparticles from 3-mercaptopropyltrimethoxysilane. Langmuir. 27, 9551–9556. https://doi.org/10.1021/la201385h.

Jain, B., Singh, B., Katare, O.P., Vyas, S.P., 2010. Development and characterization of minoxidil-loaded liposomal system for delivery to pilosebaceous units. J. Liposome Res. 20, 105–114. https://doi.org/10.1080/08982100903161449.

Jensen, L.B., Petersson, K., Nielsen, H.M., 2011. In vitro penetration properties of solid lipid nanoparticles in intact and barrier-impaired skin. Eur. J. Pharm. Biopharm., 79, 68-75. 10.1016/j.ejpb.2011.05.012.

Klang, V., Schwarz, J.C., Hartl, A., Valenta, C., 2011. Facilitating in vitro tape stripping: Application of infrared densitometry for quantification of porcine stratum corneum proteins. Skin Pharmacol. Physiol. 24, 256–268. https://doi.org/10.1159/000326072.

Knorr, F., Lademann, J., Patzelt, A., Sterry, W., Blume-Peytavi, U., Vogt, A., 2009. Follicular transport route - Research progress and future perspectives. Eur. J. Pharm. Biopharm. 71, 173–180. https://doi.org/10.1016/j.ejpb.2008.11.001.

Knudsen, N.Ø., Rønholt, S., Salte, R.D., Jorgensen, L., Thormann, T., Basse, L.H., Hansen, J., Frokjaer, S., Foged, C., 2012. Calcipotriol delivery into the skin with PEGylated liposomes. Eur. J. Pharm. Biopharm. 81, 532–539. https://doi.org/10.1016/j.ejpb.2012.04.005.

Kraeling, M.E.K., Topping, V.D., Keltner, Z.M., Belgrave, K.R., Bailey, K.D., Gao, X., Yourick, J.J., 2018. In vitro percutaneous penetration of silver nanoparticles in pig and human skin. Regul. Toxicol. Pharmacol. 95, 314–322. https://doi.org/10.1016/j.yrtph.2018.04.006.

Küchler, S., Abdel-Mottaleb, M., Lamprecht, A., Radowski, M.R., Haag, R., Schäfer-Korting, M., 2009. Influence of nanocarrier type and size on skin delivery of hydrophilic agents. Int. J. Pharm. 377, 169–172. https://doi.org/10.1016/j.ijpharm.2009.04.046.

Kumar, P., Singh, S., Handa, V., Kathuria, H., 2018. Oleic acid nanovesicles of minoxidil for enhanced follicular delivery. Medicines. 5, 103–118. https://doi.org/10.3390/medicines5030103.

Labouta, H.I., El-Khordagui, L.K., Kraus, T., Schneider, M., 2011a. Mechanism and determinants of nanoparticle penetration through human skin. Nanoscale. 3, 4989–4999. https://doi.org/10.1039/c1nr11109d.

Labouta, H.I., Kraus, T., El-Khordagui, L.K., Schneider, M., 2011b. Combined multiphoton imaging-pixel analysis for semiquantitation of skin penetration of gold nanoparticles. Int. J. Pharm. 413, 279–282. https://doi.org/10.1016/j.ijpharm.2011.03.067.

Labouta, H.I., Schneider, M., 2013. Interaction of inorganic nanoparticles with the skin barrier: Current status and critical review. Nanomed. Nanotechnol. Biol. Med. 9, 39–54. https://doi.org/10.1016/j.nano.2012.04.004.

Lademann, J., Patzelt, A., Richter, H., Antoniou, C., Sterry, W., Knorr, F., 2009. Determination of the cuticula thickness of human and porcine hairs and their potential influence on the penetration of nanoparticles into the hair follicles. J. Biomed. Opt. 14, 021014 https://doi.org/10.1117/1.3078813.

Lademann, J., Richter, H., Schanzer, S., Knorr, F., Meinke, M., Sterry, W., Patzelt, A., 2011. Penetration and storage of particles in human skin: Perspectives and safety aspects. Eur. J. Pharm. Biopharm. 77, 465–468. https://doi.org/10.1016/j.ejpb.2010.10.015.

Laffleur, F., Bernkop-Schnürch, A., 2018. Evaluation of dermal adhesive formulations for topical application. Eur. J. Pharm. Biopharm. 124, 89–94. https://doi.org/10.1016/j.ejpb.2017.12.010.

Larese, F.F., D'Agostin, F., Crosera, M., Adami, G., Renzi, N., Bovenzi, M., Maina, G., 2009. Human skin penetration of silver nanoparticles through intact and damaged skin. Toxicology. 255, 33–37. https://doi.org/10.1016/j.tox.2008.09.025.

Lau, W.M., Heard, C.M., White, A.W., 2013. Design, synthesis and in vitro degradation of a novel co-drug for the treatment of psoriasis. Pharmaceutics. 5, 232–245. https://doi.org/10.3390/pharmaceutics5020232.

Lenn, J.D., Neil, J., Donahue, C., Demock, K., Tibbetts, C.V., Cote-Sierra, J., Smith, S.H., Rubenstein, D., Therrien, J.P., Pendergrast, P.S., Killough, J., Brown, M.B., Williams, A.C., 2018. RNA Aptamer Delivery through Intact Human Skin. J. Invest. Dermatol. 138, 282-290. 10.1016/j.jid.2017.07.851.

Mahmoud, N.N., Alkilany, A.M., Dietrich, D., Karst, U., Al-Bakri, A.G., Khalil, E.A., 2017. Preferential accumulation of gold nanorods into human skin hair follicles: Effect of nanoparticle surface chemistry. J. Colloid Interface Sci. 503, 95-102. 10.1016/j.jcis.2017.05.011.

Mathes, C., Melero, A., Conrad, P., Vogt, T., Rigo, L., Selzer, D., Prado, W.A., De Rossi, C., Garrigues, T.M., Hansen, S., Guterres, S.S., Pohlmann, A.R., Beck, R.C.R., Lehr, C.M., Schaefer, U.F., 2016. Nanocarriers for optimizing the balance between interfollicular permeation and follicular uptake of topically applied clobetasol to minimize adverse effects. J. Control. Release. 223, 207–214. https://doi.org/10.1016/j.jconrel.2015.12.010.

Mun, E.A., Hannell, C., Rogers, S.E., Hole, P., Williams, A.C., Khutoryanskiy, V.V., 2014a. On the role of specific interactions in the diffusion of nanoparticles in aqueous polymer solutions. Langmuir. 30, 308–317. https://doi.org/10.1021/la4029035.

Mun, E.A., Morrison, P.W.J., Williams, A.C., Khutoryanskiy, V.V., 2014b. On the barrier properties of the cornea: A microscopy study of the penetration of fluorescently labeled nanoparticles, polymers, and sodium fluorescein. Mol. Pharm. 11, 3556–3564. https://doi.org/10.1021/mp500332m.

Mun, E.A., Williams, A.C., Khutoryanskiy, V.V., 2016. Adhesion of thiolated silica nanoparticles to urinary bladder mucosa: Effects of PEGylation, thiol content and particle size. Int. J. Pharm. 512, 32–38. https://doi.org/10.1016/j.ijpharm.2016.08.026.

Nagelreiter, C., Mahrhauser, D., Wiatschka, K., Skipiol, S., Valenta, C., 2015. Importance of a suitable working protocol for tape stripping experiments on porcine ear skin: Influence of lipophilic formulations and strip adhesion impairment. Int. J. Pharm. 491, 162–169. https://doi.org/10.1016/j.ijpharm.2015.06.031.

Otberg, N., Richter, H., Schaefer, H., Blume-Peytavi, U., Sterry, W., Lademann, J., 2004. Variations of hair follicle size and distribution in different body sites. J. Invest. Dermatol. 122, 14–19. https://doi.org/10.1046/j.0022-202X.2003.22110.x.

Owens, D.E., Peppas, N.A., 2006. Opsonization, biodistribution, and pharmacokinetics of polymeric nanoparticles. Int. J. Pharm. 307, 93–102. https://doi.org/10.1016/j.ijpharm.2005.10.010.

Padois, K., Cantiéni, C., Bertholle, V., Bardel, C., Pirot, F., Falson, F., 2011. Solid lipid nanoparticles suspension versus commercial solutions for dermal delivery of minoxidil. Int. J. Pharm. 416, 300–304. https://doi.org/10.1016/j.ijpharm.2011.06.014.

Partenhauser, A., Zupančič, O., Rohrer, J., Bonengel, S., Bernkop-Schnürch, A., 2016. Thiolated silicone oils as adhesive skin protectants for improved barrier function. Int. J. Cosmet. Sci. 38, 257–265. https://doi.org/10.1111/ics.12284.

Patzelt, A., Richter, H., Knorr, F., Schäfer, U., Lehr, C.M., Dähne, L., Sterry, W., Lademann, J., 2011. Selective follicular targeting by modification of the particle sizes. J. Control. Release. 150, 45–48. https://doi.org/10.1016/j.jconrel.2010.11.015.

Pensado, A., Chiu, W.S., Cordery, S.F., Rantou, E., Bunge, A.L., Delgado-Charro, M.B., Guy, R.H., 2019. Stratum corneum sampling to assess bioequivalence between topical acyclovir products. Pharm. Res. 36, 180–196. https://doi.org/10.1007/s11095-019-2707-3.

Porfiryeva, N.N., Moustafine, R.I., Khutoryanskiy, V.V., 2020. PEGylated systems in pharmaceutics. Polym. Sci. Ser. C. 62, 62–74. https://doi.org/10.1134/S181123822001004X.

Prasetyanto, E.A., Bertucci, A., Septiadi, D., Corradini, R., Castro-Hartmann, P., De Cola, L., 2016. Breakable hybrid organosilica nanocapsules for protein delivery. Angew. Chemie Int. Ed. 55, 3323–3327. https://doi.org/10.1002/anie.201508288.

Raber, A.S., Mittal, A., Schäfer, J., Bakowsky, U., Reichrath, J., Vogt, T., Schaefer, U.F., Hansen, S., Lehr, C.M., 2014. Quantification of nanoparticle uptake into hair follicles in pig ear and human forearm. J. Control. Release. 179, 25–32. https://doi.org/10.1016/j.jconrel.2014.01.018.

Rangsimawong, W., Opanasopit, P., Rojanarata, T., Duangjit, S., Ngawhirunpat, T., 2016. Skin transport of hydrophilic compound-loaded PEGylated lipid nanocarriers: Comparative study of liposomes, niosomes, and solid lipid nanoparticles. Biol. Pharm. Bull. 39, 1254–1262. https://doi.org/10.1248/bpb.b15-00981.

Roque, L.V., Dias, I.S., Cruz, N., Rebelo, A., Roberto, A., Rijo, P., Reis, C.P., Design of finasteride-loaded nanoparticles for potential treatment of alopecia. Skin Pharmacol. Physiol., 30, 197-204. 10.1159/000475473.

Russell, L.M., Guy, R.H., 2012. Novel imaging method to quantify stratum corneum in dermatopharmacokinetic studies: Proof-of-concept with acyclovir formulations. Pharm. Res. 29, 3362–3372. https://doi.org/10.1007/s11095-012-0831-4.

Salim, S., Kamalasanan, K., 2020. Controlled drug delivery for alopecia: A review. J. Control. Release. 325, 84–99. https://doi.org/10.1016/j.jconrel.2020.06.019.

Schiedel, C., Melero, A., Conrad, P., Vogt, T., Rigo, L., Selzer, D., Prado, W.A., De Rossi, C., Garrigues, T., Hansen, S., Guterres, S.S., Pohlmann, A., Beck, R., Lehr, C.-M., Schaefer, U., 2015. Nanocarriers for optimizing the balance between interfollicular permeation and follicular uptake of topically applied clobetasol to minimize adverse effects. J. Control. Release. 223, 207–214. https://doi.org/10.1016/j.jconrel.2015.12.010.

Slowing, I.I., Trewyn, B.G., Giri, S., Lin, V.S.Y., 2007. Mesoporous silica nanoparticles for drug delivery and biosensing applications. Adv. Funct. Mater. 17, 1225–1236. https://doi.org/10.1002/adfm.200601191.

Song, L., Hennink, E.J., Young, I.T., Tanke, H.J., 1995. Photobleaching kinetics of fluorescein in quantitative fluorescence microscopy. Biophys. J. 68, 2588–2600. https://doi.org/10.1016/S0006-3495(95)80442-X.

Takeuchi, I., Hida, Y., Makino, K., 2018. Minoxidil-encapsulated poly(L-lactide-co-glycolide) nanoparticles with hair follicle delivery properties prepared using W/O/W solvent evaporation and sonication. Biomed. Mater. Eng. 29, 217–228. https://doi.org/10.3233/BME-171724.

Teichmann, A., Jacobi, U., Ossadnik, M., Richter, H., Koch, S., Sterry, W., Lademann, J., 2005. Differential stripping: Determination of the amount of topically applied substances penetrated into the hair follicles. J. Invest. Dermatol. 125, 264-269. 10.1111/j.0022-202X.2005.23779.x.

Vogt, A., Combadiere, B., Hadam, S., Stieler, K.M., Lademann, J., Schaefer, H., Autran, B., Sterry, W., Blume-Peytavi, U., 2006. 40 nm, but not 750 or 1,500 nm, nanoparticles enter epidermal CD1a+ cells after transcutaneous application on human skin. J. Invest. Dermatol. 126, 1316–1322. https://doi.org/10.1038/sj.jid.5700226.

Vogt, A., Hadam, S., Heiderhoff, M., Audring, H., Lademann, J., Sterry, W., Blume-Peytavi, U., 2007. Morphometry of human terminal and vellus hair follicles. Exp. Dermatol. 16, 946–950. https://doi.org/10.1111/j.1600-0625.2007.00602.x.

Vogt, A., Wischke, C., Neffe, A.T., Ma, N., Alexiev, U., Lendlein, A., 2016. Nanocarriers for drug delivery into and through the skin — Do existing technologies match clinical challenges? J. Control. Release. 242, 3–15. https://doi.org/10.1016/j.jconrel.2016.07.027.

Wang, Y.Y., Lai, S.K., Suk, J.S., Pace, A., Cone, R., Hanes, J., 2008. Addressing the PEG mucoadhesivity paradox to engineer nanoparticles that “slip” through the human mucus barrier. Angew. Chemie Int. Ed. 47, 9726–9729. https://doi.org/10.1002/anie.200803526.

Ways, T.M.M., Lau, W.M., Ng, K.W., Khutoryanskiy, V.V., 2018. Synthesis of thiolated, PEGylated and POZylated silica nanoparticles and evaluation of their retention on rat intestinal mucosa in vitro. Eur. J. Pharm. Sci. 122, 230–238. https://doi.org/10.1016/J.EJPS.2018.06.032.

Williams, A.C., Edwards, H.G.M., Barry, B.W., 1994. Raman spectra of human keratotic biopolymers: Skin, callus, hair and nail. J. Raman Spectrosc. 25, 95–98. https://doi.org/10.1002/jrs.1250250113.

Wu, X., Biatry, B., Cazeneuve, C., Guy, R.H., 2009. Drug delivery to the skin from sub-micron polymeric particle formulations: Influence of particle size and polymer hydrophobicity. Pharm. Res. 26, 1995–2001. https://doi.org/10.1007/s11095-009-9915-1.

Yang, Y., Wan, J., Niu, Y., Gu, Z., Zhang, J., Yu, M., Yu, C., 2016. Structure- Dependent and glutathione-responsive biodegradable dendritic mesoporous organosilica nanoparticles for safe protein delivery. Chem. Mater. 28, 9008–9016. https://doi.org/10.1021/acs.chemmater.6b03896.

Zhang, L.W., Yu, W.W., Colvin, V.L., Monteiro-Riviere, N.A., 2008. Biological interactions of quantum dot nanoparticles in skin and in human epidermal keratinocytes. Toxicol. Appl. Pharmacol. 228, 200–211. https://doi.org/10.1016/j.taap.2007.12.022.

Zhang, Q., Liu, F., Nguyen, K.T., Ma, X., Wang, X., Xing, B., Zhao, Y., 2012. Multifunctional mesoporous silica nanoparticles for cancer-targeted and controlled drug delivery. Adv. Funct. Mater. 22, 5144–5156. https://doi.org/10.1002/adfm.201201316.

Zhou, M., Du, X., Li, W., Li, X., Huang, H., Liao, Q., Shi, B., Zhang, X., Zhang, M., 2017. One-pot synthesis of redox-triggered biodegradable hybrid nanocapsules with a disulfide-bridged silsesquioxane framework for promising drug delivery. J. Mater. Chem. B. 5, 4455–4469. https://doi.org/10.1039/c6tb03368g.

Thiolated and PEGylated silica nanoparticles as a model for drug delivery to the hair follicles

Jamila H. Al Mahrooqi, Vitaliy V. Khutoryanskiy, Adrian C. Williams*

Reading School of Pharmacy, University of Reading, Reading RG6 6AD, U.K.

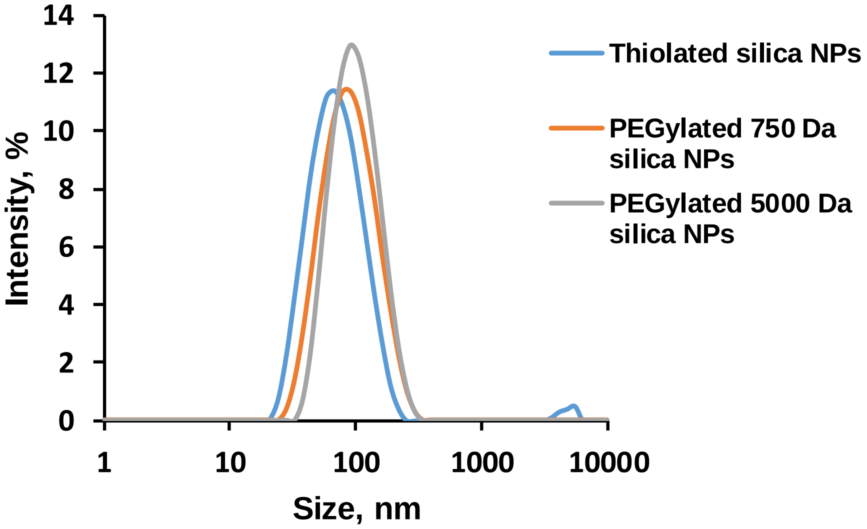

Figure S 5: Dynamic light scattering size distribution of thiolated, PEGylated 750 and 5000 Da silica nanoparticles.

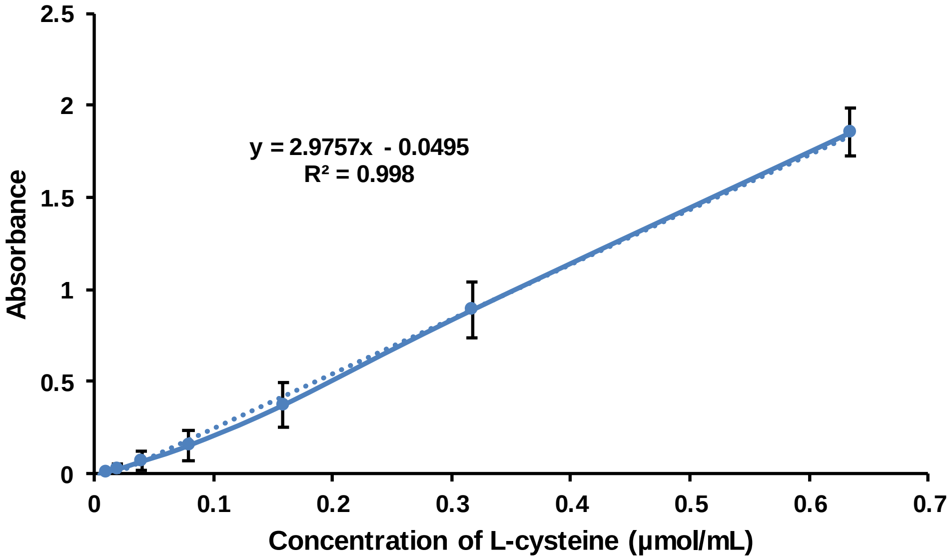

Figure S 6: L-cysteine calibration curve used for calculation of free thiol content in TSNPs and PEGylated TSNPs (n=3, mean ± SD).

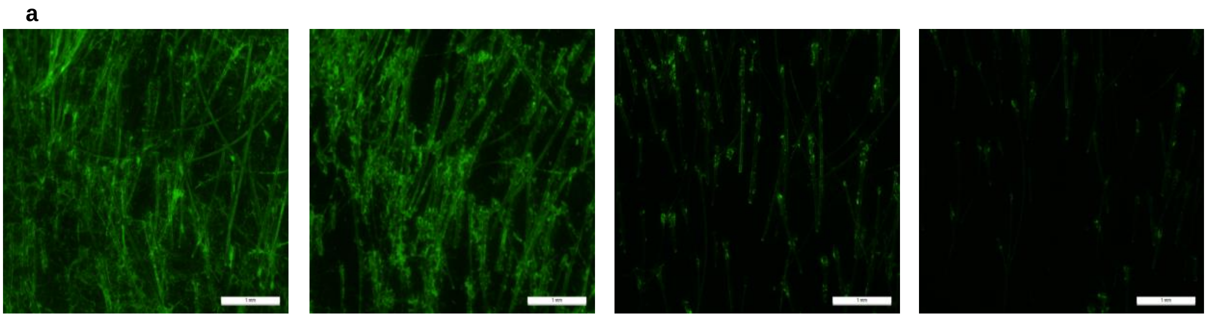

Before ts & incubation 1 ts 10 ts 20 ts

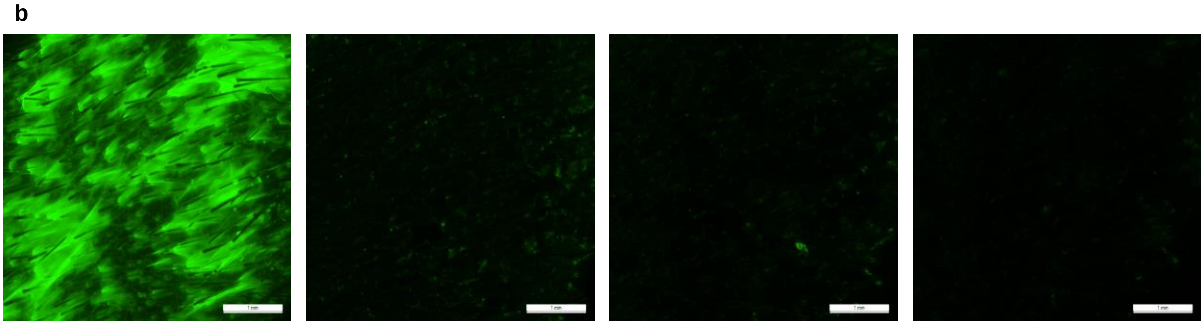

Before ts & incubation 1 ts 20 ts

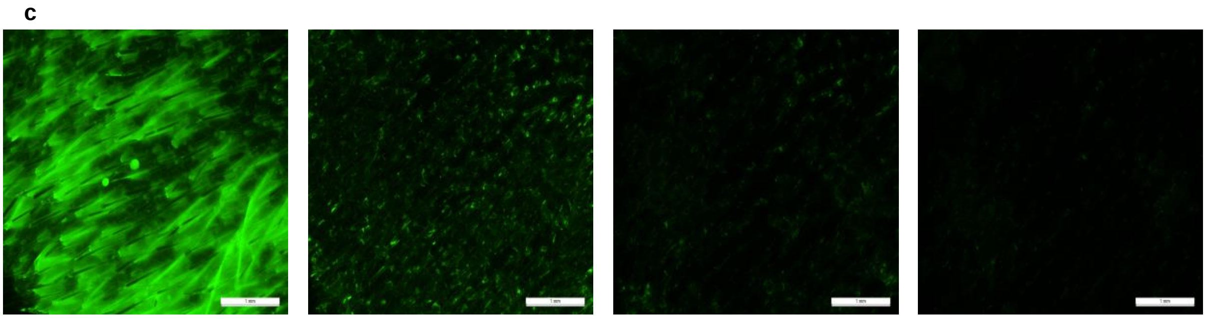

Before ts & incubation 1 ts 10 ts 20 ts

Figure S 7: Microscopic images of unshaved whole flank pig skin after application of thiolated nanoparticles (a), PEGylated 750 (b) and 5000 Da (c) nanoparticles, after the first tape stripping (1 ts), 10 tape stripping (10 ts) and 20 tape stripping (20 ts).

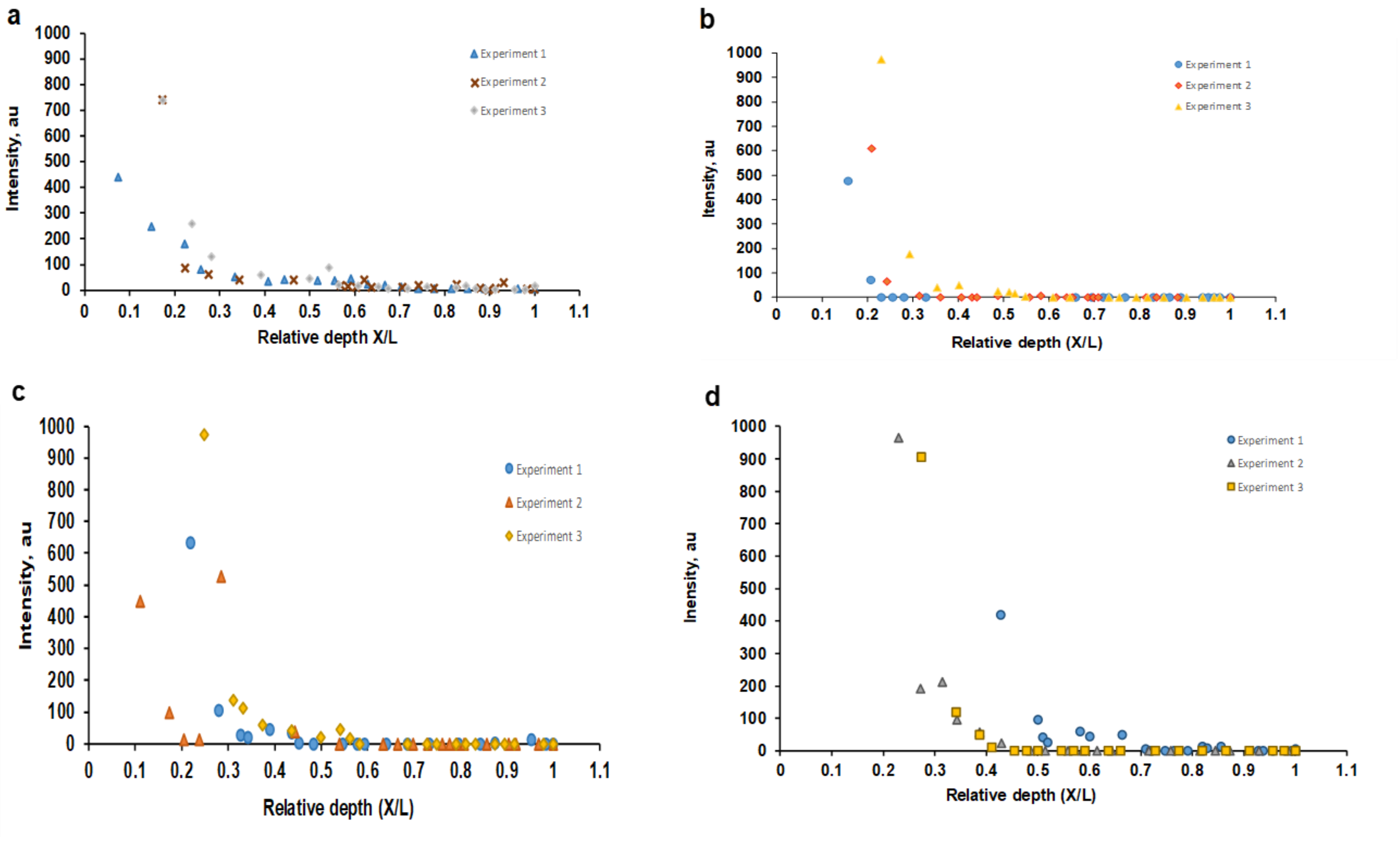

Figure S 8: Nanoparticles distribution profiles as a function of cumulative stratum corneum weight removed (a: sodium fluorescein, b: thiolated nanoparticles, c: PEGylated 750 Da nanoparticles, c: PEGylated 5000 Da nanoparticles)

Chapter 4

Diffusion of thiolated and PEGylated silica nanoparticles in the vitreous humour

In this chapter, the diffusion of thiolated and PEGylated (750, 5000, 10000 Da) nanoparticles in the vitreous humour was investigated. PEGylation enhanced the diffusion of the nanoparticles.

This manuscript is under final review before submission.

Diffusion of thiolated and PEGylated silica nanoparticles in the vitreous humour

Jamila H. Al Mahrooqi[a, b], *Adrian C. Williams*[a], *Vitaliy V. Khutoryanskiy*[a]*

[a] Reading School of Pharmacy, University of Reading, Reading RG6 6AD, U.K.

[b] Oman College of Health Sciences, P.O.Box 1928, 114, Muttrah, Oman.

KEYWORDS

Vitreous humour, nanoparticles, diffusion, PEGylation, grafting density, intravitreal injection.

ABSTRACT

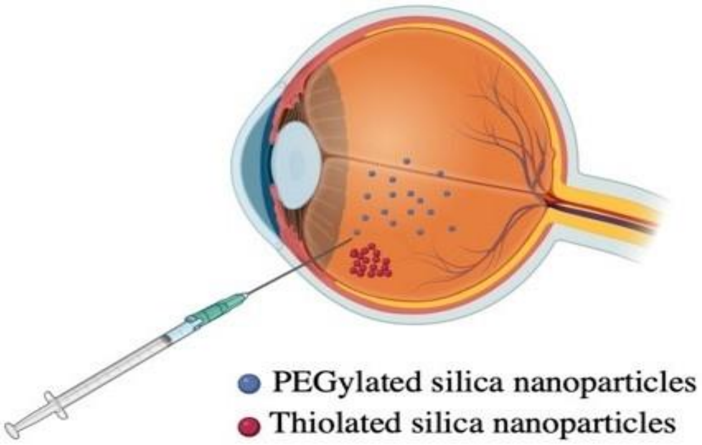

Intravitreal injection is commonly used to deliver drugs to the retina and requires molecular diffusion in the vitreous humour to reach the target site. The vitreous humour has a gel structure composed mainly of water (> 98%), hyaluronan and collagen. Current research is exploring the use of nanoparticles as carriers for delivery of drugs and proteins to the retina and the surface chemistry of the nanoparticles, size and stability are crucial for optimal delivery. Our aim was to design and test nanoparticle PEGylation to enhance diffusion through the vitreous humour, and to relate grafting density and conformation to permeation properties. Fluorescently-labelled thiolated and PEGylated (750, 5000 and 10000 Da) silica nanoparticles were synthesized and their size and zeta potential measured. As expected, PEGylation decreased the free thiol groups on the particle surfaces and increased particle size. Grafting density was determined by thermogravimetric analysis and decreased with increasing molecular weight of the PEG, from ~11 chains per nm^2 when decorated with PEG 750 Da to ~2 chain per nm^2 with the PEG 10000 coating. Nanoparticle diffusion in the vitreous humour was compared to that of sodium fluorescein using a novel *in vitro* fluorescence-based method. Diffusion of thiolated nanoparticles through the vitreous humour within 24 hours was limited, whereas PEGylated nanoparticles and sodium fluorescein readily diffused through this medium. Our results show that, despite the increase in particle size, PEGylation promotes diffusion through the vitreous humour by reducing the free thiol groups (and negative charge) on the particle surface with the formation of flexible soft corona that enhanced permeation.

INTRODUCTION

The eye presents various natural protection mechanisms that limit topical drug delivery to the posterior chamber. Anatomical and physiological barriers include blinking, poor permeability of corneal and conjunctival membranes, tear production and nasolacrimal drainage. Additionally, blood-aqueous and blood-retinal barriers present challenges for drug delivery to the eye[1–4]. Topical application of eye drops is the preferred route of drug administration for patient convenience and allows self-administration. However, when applied topically, only a small fraction of the dose reaches the posterior chamber of the eye. Attempts to overcome these limitations include the use of mucoadhesive formulations that improve retention on the ocular surfaces or formulations with permeability enhancement effects that facilitate drug penetration through the corneal and conjunctival membranes. Research is ongoing to develop drug carriers such as, nanoparticles, nanosuspensions, liposomes and niosomes for prolonged drug release[1,3–8]. The use of penetration enhancers could also provide opportunities for efficient drug delivery to the eye[1,5].

Intravitreal injections are used to deliver therapeutic agents to the retina; following administration, molecules have to diffuse through the vitreous humour which is a gelatinous cell free structure composed mainly of water (> 98%), hyaluronan and collagen[1,2,5,9]. This therapeutic approach is commonly used for treating patients suffering from age-related macular degeneration where it remains the only clinically effective route for administration of anti-vascular endothelial growth factor[2,4]. Injections are typically every month or two months which can result in poor compliance and exposes patients to risks of infections, vitreous haemorrhage, cataract and elevation of intraocular pressure[2,5]. However, this approach is effective and provides therapeutically effective drug levels, minimises systemic side effects from oral dosing and is widely considered the most successful method to deliver drugs to the retina[9]. Additional challenges to delivering drugs to the vitreous humour include aggregation, insufficient distribution and rapid clearance[10,11].

It has been reported that the movement of liquid through the vitreous body is by convection and/or diffusion. A spherical model of the vitreous body and mathematical equations for both flow and diffusion were used to explain some experimental observations. The total flux was obtained by summing the fluxes due to diffusion and convection. It was reported that the flux per unit concentration of small dissolved species, such as sodium ions, is drawn mainly by diffusion as the flux per unit concentration difference due to diffusion was around eight times the flux due to convection. This agreed with reported experimental observation where a tracer was injected into the vitreous body *in vivo* and distributed into the interior chamber, counter to the convective flow direction[12,13]. However, these equations are not valid for large particles as their diffusion coefficient is low, and they therefore travel as a front with the convective flow rather than by passive diffusion. Large particles were reported to move posteriorly and deposit on the retina after retrolental deposition in the vitreous body of the living eye[12,14]. It is also important to consider the mesh size of the vitreous humour, in addition to surface chemistry, and nanoparticles should be smaller than the mesh size of the gel network to facilitate their movement. Wu et al.[15] studied the propulsion of magnetic helical micropropellers coated with liquid perfluorocarbon through the vitreous humour and found that movement was facilitated by both their size, which was comparable to the mesh size of porcine vitreous humour, and the coating which minimized their adsorption to the vitreous humour. Using optical coherence tomography to monitor movement of the micropropellers confirmed their arrival at the retina and they reported a speed of propulsion in the porcine vitreous humour of ~ 10 μm/s compared to 1.5 μm/s in the case of nanosized helical propellers. Xu et al.[16] reported that the mobility of cationic particles in the vitreous humour is inhibited by electrostatic interactions with hyaluronic acid molecules independent of their size (181 nm) whereas anionic particles sized 227 nm diffused freely in the vitreous at rate close to their diffusion in water. Tavakoli et al.[17] studied diffusion of a wide range of lipid-based nanoparticles in the vitreous humour with single-particle tracking and reported restricted movement of cationic nanoparticles, and mobility of anionic nanoparticles of all sizes used and of neutral nanoparticles below 200 nm. PEGylation did not affect the behaviour of the anionic and small neutral nanoparticles, however, it improved the movement of both large neutral and cationic nanoparticles. They concluded that convection had a significant role in the pharmacokinetics of the nanoparticles.

Here, we synthesized 45 ± 1 nm thiolated silica nanoparticles and functionalized them with 750, 5000 and 10000 Da polyethylene glycol (PEG). These nanoparticles were fluorescently-labelled and a new fluorescent approach was developed to study the diffusion of these nanoparticles through *ex vivo* bovine vitreous humour.

EXPERIMENTAL SECTION

Materials. 3-mercaptopropyltrimethoxysilane (MPTS 95%), maleimide terminated methoxy poly(ethylene glycol) (PEG molecular weight 750, 5000 & 10000 Da), sodium phosphate dibasic (≥99%), sodium phosphate monobasic dihydrate (≥99%), 5-(iodoacetamido)fluorescein, sodium fluorescein, and 5,5′-dithiobis(2-nitrobenzoic acid) (Ellman's reagent, DTNB, ≥98% TLC), were purchased from Sigma-Aldrich (UK). DMSO, sodium hydroxide pellets and plastic disposable UV grade cuvettes (transparent four walls) were purchased from Fisher Scientific (UK). L-Cysteine hydrochloride anhydrous (98%) was purchased from Alfa Aesar (UK). Dialysis membrane with molecular cut-off 12–14 kDa was purchased from Medicell International Ltd. (UK).

Synthesis of thiolated silica nanoparticles (TSNPs). Thiolated silica nanoparticles were synthesised according to a previously published method [18]. Briefly, 20 mL DMSO and 0.5 mL of 0.5 M NaOH solution were added to 0.75 mL MPTS. The mixture was stirred continuously with air bubbling for 24 h at room temperature. The nanoparticles were purified by dialysis against deionized water (5 L, eight changes of water) using dialysis membrane. The purified aqueous dispersions of the nanoparticles were stored at 4 °C.

Ellman's assay. The thiol group content in nanoparticles was determined by Ellman's assay according to a previously published method [19]. Briefly, thiolated and PEGylated nanoparticles were freeze dried using a Heto Power Dry LL 3000 freeze-dryer (Thermo Electron Corporation) prior to analysis. Nanoparticle dispersions (10 mL at 0.3 mg/mL) were prepared in phosphate buffer (0.5 mol/L, pH 8) and allowed to hydrate for 1 h. In the meantime, 3 mg of Ellman's reagent (DTNB) was dissolved in 10 mL of 0.5 mol/L phosphate buffer solution at pH 8. After particle hydration, 500 µL of the DTNB solution were added to 500 µL aliquots of the nanoparticles dispersion and incubated in the dark for 90 min. Then, dispersions were centrifuged for 10 min at 13,000 rpm (Sanyo, MSE Micro Centaur), before 200 µL samples of the supernatant were placed in a 96-well microtiter plate and absorbance measured at 420 nm with a plate reader (Epoch, BioTek). A stock standard solution of cysteine hydrochloride (5 mg/mL) was used to prepare a series of solutions under the same conditions from 0.004 to 0.634 µmol/mL for a calibration curve to calculate nanoparticle thiol concentration (Supplementary information, Figure S1).

Synthesis of fluorescently labelled thiolated silica nanoparticles. Thiolated silica nanoparticles were labelled with 5-(iodoacetamido) fluorescein (5-IAF) by adding 3 mg of 5-IAF to 12 mL aqueous dispersions of thiolated nanoparticles. The amount of fluorophore used was calculated with respect to molar ratio so that 5 µmol of fluorophore was added to 50 µmol of sulfhydryl groups of the nanoparticles. The reaction mixture was stirred for 16 h at room temperature protected from light. Fluorescently-labelled nanoparticles were purified by dialysis against deionized water in the dark (5 L, eight changes of water) [18]. Sodium fluorescein was prepared by dissolving 0.5 mg of the fluorophore in 10 mL of deionised water and left at room temperature in the dark for 5 hours under constant stirring [20].

PEGylation of fluorescently labelled nanoparticles. 5 mL aqueous dispersions of fluorescently labelled nanoparticles were mixed with 100 mg of methoxypolyethylene glycol maleimide of three molecular weights (750, 5000 or 10000 Da). The reaction mixture was stirred for 16 h at room temperature protected from light, resulting in the formation of PEGylated silica nanoparticles. PEGylated nanoparticles were purified by dialysis in the dark as above [20].

Dynamic Light Scattering (DLS). Size and ʒ-potential measurements were conducted with dilute dispersions of thiolated and PEGylated nanoparticles at 25 °C using a Nano-S Zetasizer

(Malvern Instruments, UK). Each batch of nanoparticles was synthesized in triplicate, and the analysis was carried out three times for each sample. The mean and standard deviation of particle size, polydispersity, and ʒ-potential were calculated.

Thermogravimetric analysis (TGA). The thermal decomposition of thiolated and PEGylated silica nanoparticles was studied using a Q50 thermogravimetric analyser (TA Instruments, UK). Briefly, 2 mg of freeze-dryed thiolated or PEGylated silica nanoparticles were placed on DSC aluminium pan and heated from 25 to 600 ºC at 5 ºC/min under nitrogen at 20 mL/min. The residual mass at 593 ºC, representing the bare nanoparticles was determined from which the mass of a single nanoparticle was calculated using the density of silicon dioxide (2.3 g/cm^3) and the volume of the sphere (average size of nanoparticles measured using DLS is 45 nm):

$$\text{Mass of one nanoparticle} = \text{density} \times \text{volume} \qquad \text{Equation (1)}$$

$$\text{Number of nanoparticles} = \frac{\text{mass of sample}}{\text{mass of a single nanoparticle}} \qquad \text{Equation (2)}$$

Using the mass of PEG lost on heating the number of PEG molecules in the sample and per nanoparticle was calculated according to:

$$\text{Number of PEG molecues in sample} = \frac{\text{mass of PEG}\times\text{Avogadro number}}{\text{molecular weight of PEG}} \qquad \text{Equation (3)}$$

$$\text{Number of PEG molecules/particle} = \frac{\text{number of PEG molecules in sample}}{\text{number of nanoparticles in sample}} \qquad \text{Equation (4)}$$

From this, the number of PEG chains/nm^2 was determined by dividing the number of PEG molecules per nanoparticle by the surface area of the nanoparticles (detailed calculations for all polymers are in supplementary information).

Diffusion studies. Freshly extracted bovine eyes were obtained from P.C. Turner Abattoir (Northcamp, UK). The posterior pole of the bovine eyeball was dissected to gain access to the vitreous body. The vitreous humour was decanted from the back of the eyeball into a plastic cuvette and covered before placing in an incubator (37 ºC) for 10 minutes to warm to body temperature. Then, 50 µL of fluorescently-labelled sample (either thiolated, PEGylated 750 Da, 5000 Da, 10000 Da nanoparticles or sodium fluorescein 0.05mg/mL[20]) was applied on the top of the vitreous humour[16,21]. The cuvette was placed in a black box equipped with a UV lamp and images were taken at 0, 0.5, 1, 1.5, 2, 3, 4, 5, 6, and 24 hours. The cuvette was wrapped with aluminium foil and placed back in the incubator after recording each image. All experiments were conducted in triplicate and images were analysed using ImageJ software to measure the distance that the nanoparticles travelled over time. Data were analysed using GraphPad Prism 8 with statistical significance determined using two-way analysis of variance (ANOVA) with the least significant difference post-hoc test.

RESULTS AND DISCUSSION

Synthesis and characterization of thiolated and PEGylated nanoparticles. Synthesis and formation of sub-100 nm thiolated silica nanoparticles using 3-mercaptopropyltrimethoxysilane (MPTS) as the silica precursor in dimethyl sulfoxide (DMSO) in contact with air, with NaOH as the catalyst was previously reported by Irmukhametova et al.[18,22]. The cross-linked nanoparticles are formed through Si-O-Si and disulfide bonds. The nanoparticles were labelled with 5-IAF, where the iodoacetamide moiety of the fluorophore reacts with the sulfhydryl group in the nanoparticles. Fluorescently labelled nanoparticles were then PEGylated, and both labelled thiolated and PEGylated silica nanoparticles were used in all experiments.

DLS sizing showed an increase in size with PEGylation with narrow polydispersity and negative ʒ-potential values due to the presence of thiol groups at their surface (Table 1). Multiple t-test comparison showed significant differences in size between all the four types of nanoparticles ($p < 0.05$). Generally, PEGylation increases the size of the nanoparticles due to the formation of a PEG shell. The size of nanoparticles increased in the order TSNPs < PEGylated 10000 Da < PEGylated 750 Da < PEGylated 5000 Da nanoparticles; the largest molecular weight PEG did not generate the largest nanoparticles due grafting density and conformation of the polymer on the nanoparticle as discussed below. In addition, Ellman’s assay showed statistically significant differences in free thiol content between TSNPs and all PEGylated counterparts. Among PEGylated nanoparticles, there was a statistically significant difference in thiol content between PEGylated 10000 Da nanoparticles and both PEGylated 750 Da and 5000 Da nanoparticles. The reduction in thiol content and increase in particle size after PEGylation indicates successful PEGylation of the nanoparticles (Table 1). The calibration curve used to calculate free thiol content is shown in Figure S1 (Supplementary information). The concentration of the nanoparticles was determined by freeze-drying 1 mL of nanoparticles suspension and determining the weight of the solid residue. This concentration was used to calculate free thiol content before and after PEGylation.

Table 1: Characterization of thiolated and PEGylated silica nanoparticles (n=3, values presented as mean ± standard deviation)

Type of nanoparticles	Size (nm)	PDI	ζ-potential (mV)	Grafting density (chain/nm^2)	Concentration of nanoparticles (mg/mL)	Free thiol content (µmol/g)
Thiolated	45 ± 1	0.170 ± 0.018	-44 ± 5	-	12 ± 1	289 ± 14
PEGylated 750 Da	79 ± 1	0.214 ± 0.011	-42 ± 3	10.6 ± 1.4	12 ± 1	144 ± 21
PEGylated 5000 Da	89 ± 1	0.169 ± 0.010	-30 ± 2	3.2 ± 0.4	20 ± 2	142 ± 2
PEGylated 10000 Da	73 ± 1	0.170 ± 0.021	-29 ± 2	1.9 ± 0.1	14 ± 2	174 ± 32

The increase in size after PEGylation and the size variation among PEGylated nanoparticles can be explained in the terms of the conformation of PEG shell around the core of the nanoparticles. PEG was reported to form either a brush or a mushroom conformation on nanoparticle surfaces; the mushroom conformation is characterised by low packing densities and random polymer orientations whereas the brush is typified by extended weakly aligned chains with ~ 10-fold greater packing densities than the mushroom conformation [23–29]. The grafting density, in chain/nm^2, of the polymers are in Table 1 and were calculated from the TGA data (Figure 1). Grafting densities can be calculated from nanoparticle volumes (see Supplemetary information, Table S1), but this assumes perfect packing of the nanoparticles in the sample with no void space and so is prone to error; here, we used sample and polymer masses to determine the grafting density (Supplementary information, Table S2 and method).

Grafting densities were 10.6, 3.2 and 1.9 chain/nm^2 for PEGylated (750 Da, 5000 Da and 10000 Da) nanoparticles, respectively. In general, higher grafting density values are reported for lower molecular weight PEG in comparison to those for higher molecular weights of the polymer[30]. Mansfield et al.[31] grafted thiolated silica nanoparticles with poly(N-isopropyl acrylamide) (PNIPAM), and poly(2-n-propyl-2-oxazoline) (PNPOZ) 5000 Da and reported densities of 1.2 and 1 chain/nm^2, respectively. Shui et al.[30] modified silica nanoparticles with N-(2-aminoethy)-3-aminopropylmethyldimethoxysilane and grafted them with methoxypolyethylene glycol of molecular weights 750, 2000 and 4000 Da reporting grafting densities of 2.8, 1.47 and 0.76

chains/nm^2 respectively. Further, gold nanoparticles were grafted with PEG 1000, 2000, 5000, 10000 and 20000 Da and the grafting density was measured using TGA, analytical ultracentrifugation and total organic carbon analysis. The calculated grafting densities from the different methods were consistent with minor variations and again a reduction in grafting density was reported with increasing chain length of the polymer[24]. Similar trend was reported by Xia et al. who grafted gold nanoparticles with PEG 3000, 5000 and 20000 Da at densities of 2.21, 1.33 and 0.21 chain/nm^2, respectively. The study also attached PEG 5000 Da to different sized gold nanoparticles and reported an increase in grafting density with increasing nanoparticle diameter; particles of 30, 50 and 60 nm diameters had grafting densities of 0.61, 0.85 and 1.36 chain/nm^2, respectively[32]. The grafting densities determined in the present study are consistent with those in the literature with a reduction in values as the molecular weight of the polymer increases.

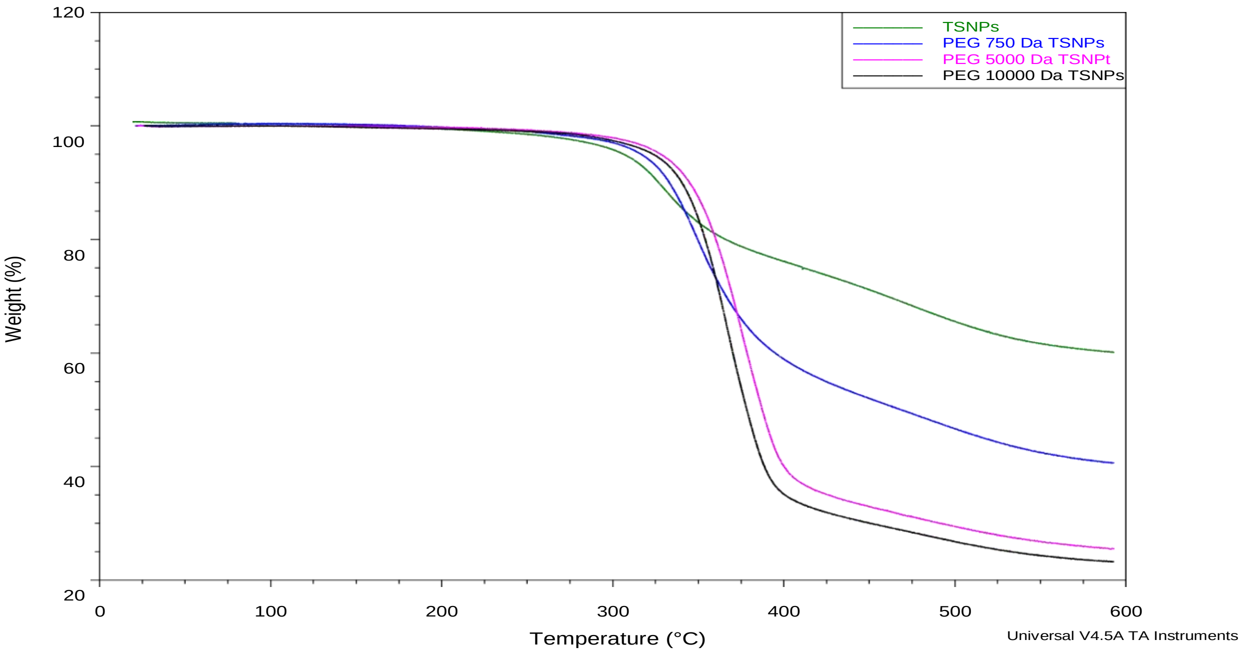

Figure 1: Thermogravimetric analysis of thiolated and PEGylated (750 Da, 5000 Da and 10000 Da) silica nanoparticles

To determine the conformation of the PEG chains on the nanoparticle surface, the Flory radius (R_f) was calculated using equation 5 and distance between grafting sites (D) was calculated using equation 6. Results are summarised in (Table 2):

$R_f \cong N^{3/5}\alpha$ equation (5)[23]

$\mathrm{D} = \alpha\,\sigma^{-1/2}$ equation (6)[33]

where N is the number of repeating units per polymer chain, α is the length of the repeating unit (3.5 Å for PEG) and σ is the grafting density[23,33].

Table 2: Polymer brush characterisation and distance between the grafted sites on nanoparticles grafted with PEG 750, 5000 and 10000 Da.

Type of nanoparticles	**Flory radius, R_f (nm)**	**Radius of gyration, R_g (nm)**	**Brush thickness (nm)**	**Distance between the grafted sites, D (nm)**
PEGylated 750 Da	2	0.6	34	0.1
PEGylated 5000 Da	6	1.5	44	0.25
PEGylated 10000 Da	9	2.1	28	0.37

It has been reported that the grafted chains a take brush conformation if $R_f > D$; with all our PEG molecular weights, the Flory radius was greater than the distance between grafted sites[34]. In addition, the brush thickness was calculated from DLS measurements (the difference of hydrodynamic radius of the polymer grafted particles and the core particles) and the radius of gyration was calculated using equation 7 (Table 2).

$\mathrm{R_g} = \alpha\sqrt{\frac{\mathrm{N}}{6}}$ equation (7)

When the grafting density is lower than $1/\mathrm{R_g^2}$, or if the molecular weight of the polymer is low, the chains form mushroom-like conformation on the surface due to the lack of interaction between them. The chains begin to overlap and behave as brushes when the brush thickness ≈ $2\mathrm{R_g}$. This behaviour is seen with low-to-intermediate grafting densities and is termed a semi-dilute polymer brush (SDPB) when the inter-monomer interaction is between pairs of polymer chains. Concentrated polymer brushes (CPB) form at higher grafting densities and an increase in brush thickness is evident, commonly seen with short chains high grafting densities where $\mathrm{h} \propto \mathrm{N}^{3/5}$. When long chain polymers are grafted onto a spherical nanoparticle, the brushes display mixed behaviour with a CPB domain close to the core particle and SDPB with more relaxed chains at a distance r_c from the centre of the nanoparticle (Figure 2)[29].

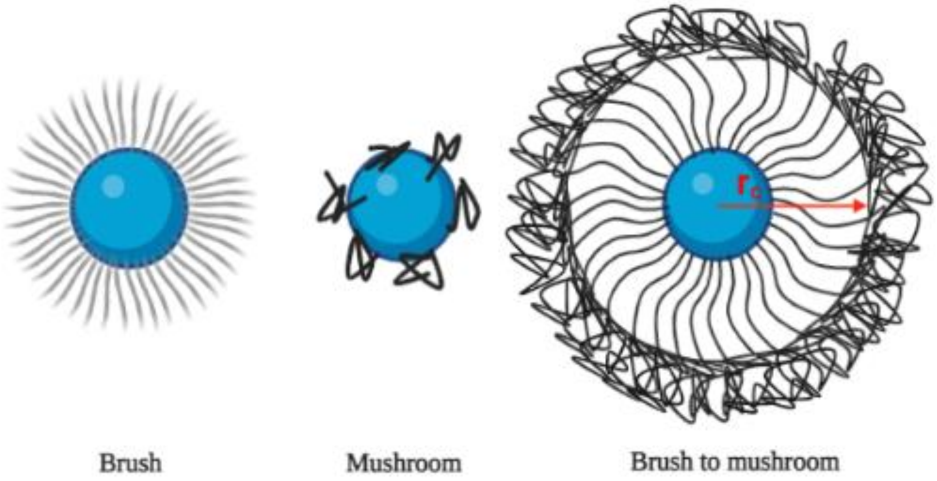

Figure 2: Different possible conformations of polymer brushes grafted on spherical nanoparticles. Polymers with short chains and high grafting density form brush conformation. At low grafting densities polymers form the mushroom conformation. Polymers with long chains form a brush conformation close to the core particle and a mushroom conformation at a distance from the centre of the nanoparticle

Our PEGylated 750 Da nanoparticles with grafting density of 10.6 chain/nm^2 and brush thickness almost 57 times greater than radius of gyration are likely to display a brush conformation (CPB regime). PEGylated 5000 and 10000 Da particles, with grafting densities of 3.2 and 1.9 chain/nm^2 respectively and brush thicknesses 29 and 14 times greater than radius of gyration may form brushes with SDPB behaviour [29]. However, with these longer polymer chains, it is likely that CPD brushes will initially form up to a distance r_c from the centre of the nanoparticle with the outermost chains transitioning to an SDPB conformation (Figure 2). This transition results from the increase in shell volume available for the chains which increases with distance from the spherical particle core and as a result the packing constrains near the surface relaxes [29]. This conformational change may explain the reduction in brush thickness of PEG 10000 Da compared to PEG 750 and 5000 Da brushes.

Diffusion studies. For drug delivery it is important to understand the factors that affect the diffusion of nanoparticles in non-Newtonian fluids where the Stokes-Einstein equation may not be applicable[35]. Enhancing nanomaterials diffusivity in viscous biological fluids such as gels and mucous tends to improve drug delivery[36]. The vitreous humour is mainly composed of water >98% W/W, collagen fibres (types II and IX) and glycosaminoglycans such as hyaluronic acid[5,37,38]. Drug permeation in the vitreous humour occurs mainly by diffusion and drug size and charge are important controlling factors since the vitreous humour consists of a negatively charged polymer network [39]. Several methods have been used to study the diffusivity of materials in the vitreous humour following intravitreal injection including transmission electron microscopy, fluorescence microscopy and confocal scanning laser microscopy[16,37,40,41]. Laud et al.[11] reported that intravitreal injection of particles forms a "pocket" similar to that formed when injected into the vitreous humour in a cuvette. Here, we developed a new simple and rapid *ex vivo* method to study the diffusion of the thiolated and PEGylated (750, 5000 and 10000 Da) nanoparticles in the vitreous humour and compared their diffusive properties with sodium fluorescein as a positive control. Nanoparticles were deposited (rather than injected) onto the vitreous humour to assess the influence of surface chemistry on diffusivity (Figure 3).

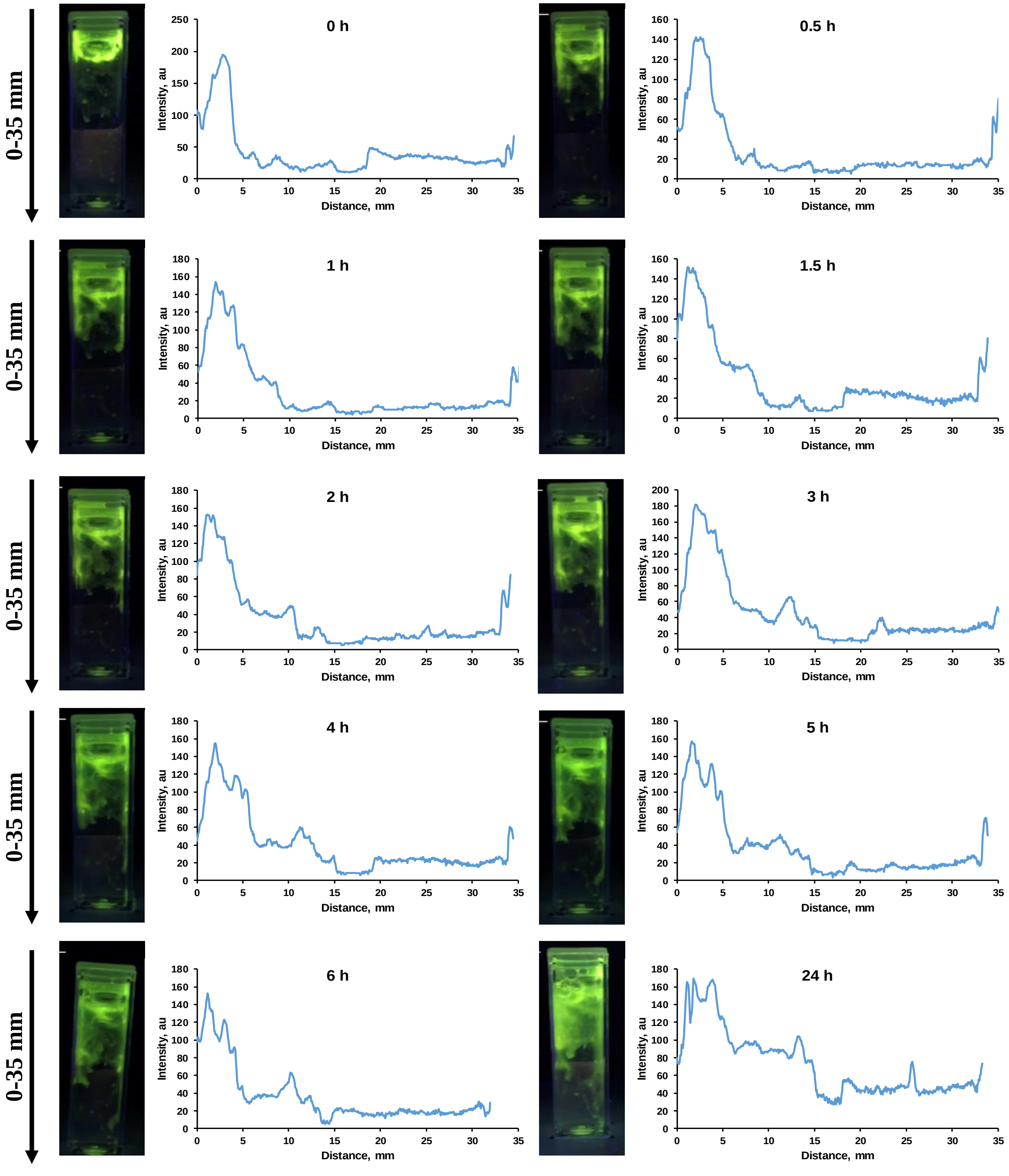

Figure 3: Exemplar images showing the diffusion of PEGylated 5000 Da nanoparticles over time in vitreous humour in a cuvette. The plot adjacent to each image is from image analysis of the fluorescence intensity of a single measurement (a line was drawn from top to bottom in the centre of the cuvette)

It was reported that diffusivity of solutes is largely based on electrostatic interaction mediated by glycosaminoglycans, collagen and heparin sulfate with anionic nanoparticles diffuse in the vitreous humour whereas cationic nanoparticles movement is hindered[37,38]. Thus, we expect that our nanoparticles will diffuse freely as they are negatively charged and smaller than (i.e. <90 nm) the mesh size of the bovine vitreous humour (~ 550 ± 50 nm[16]). However, our thiolated nanoparticles were immobile and remained bound to the surface of the vitreous humour after 24 hours incubation, though they carry a negative charge (Supplementary information, Figure S2, a). The ʒ-potential measured for the thiolated particles was -44 mV but was not significantly different ($p>0.05$) than that measured of the freely diffusing PEG 750 nanoparticles (-42 mV), demonstrating that the restricted movement of the thiolated materials was not attributable to the relatively high surface charge. It was reported that Type II collagen exists in two splice variants with one coding for 69 cysteine-rich domain amino acids and cysteine is also one of the non-enzymatic vitreous anti-oxidant system [42,43]. Ansari et al.[44] used smart sensors based on silver nanoparticles to determine time of death by quantification of vitreous humour L-cystine, which results from oxidation of cysteine, and reported an increase in cystine concentration (up to 96 hours) post-mortem. This likely explains the behaviour of the thiolated nanoparticles as they are rich in thiol groups on their surface (approximately twice that of the PEGylated materials) and cysteine is highly reactive with thiols which trapped the nanoparticles on the surface of the vitreous humour.

Contrarily, PEGylated nanoparticles diffused rapidly after deposition although the images are heterogenous (Supplementary information, Figure S2, b-d), which could be related to the inhomogeneous distribution of biopolymers within the vitreous, whereas free sodium fluorescein, neutral small molecule, movement was more uniform (Supplementary information, Figure S2, e)[37]. Generally, image analysis of the fluorescence intensity showed greater values at the top of the vitreous humour which decreases over time and appears as a broadening in the fluorescence intensity peak and can be taken as an indication of diffusion (Figure 3). Although the vitreous humour is composed of >98% water, small molecules can diffuse freely across the network but slower than in water and large molecules movement is restricted by the fibrillar structure of the vitreous humour[9]. We used sodium fluorescein (376 Da) as it is an example of low molecular weight compounds which are not restricted to diffuse through the vitreous humour meshwork[39,45]. Whilst the rheological behaviour of bovine vitreous humour is similar to that from the human eye, the steady state flux and diffusion coefficient of fluoresceine in human vitreous humour was reported to be approximately twice that in bovine media[45]. In a study by Tan et al.[46], compounds with different molecular weights were used as model for the assessment of their movement in the partially liquefied vitreous after intravitreal injection and sodium fluorescein was used as a representative compound to intravitreal antimicrobials and steroids used to treat ocular infection and inflammation. The random flow and diffusion of PEGylated nanoparticles in the vitreous humour can be clearly seen from the images (Supplementary information, Figures S2, b-d). Jongebloed et al.[9,47] reported the presence of cisterns which are internal spaces in the vitreous humour which may explain the diffusion behaviour of PEGylated nanoparticles. It was noted that the cisternal structure of vitreous humour was preserved even when it is placed into a cuvette. The dimension of the cistern was reported to vary regionally which was observed after injecting a mixture of red ink particles (0.1-0.25 μm) and white ink particles (0.25-0.5 μm). The red ink penetrated deeper where the cistern meshwork was tighter, whereas white ink remained adhered to the superficial layer of the cisternal wall[47,48]. It seems that PEGylated nanoparticles diffuse through these spaces before other parts of the vitreous humour[48]. By comparing the distance travelled by these nanoparticles over time, measured using imageJ software, there was statistically significant difference in the diffusion between thiolated and PEGylated 10000 Da nanoparticles after one hour of application and between thiolated nanoparticles and sodium fluorescein, PEGylated 750, 5000 and 10000 Da nanoparticles after 24 hours of application ($p < 0.05$) (Figure 4). Despite the statistical insignificance in other time points, all PEGylated nanoparticles diffused into the vitreous humour over time as they are negatively charged with size range below 100 nm and reduced thiol content. They also diffused faster than sodium fluorescein as PEG forms a soft shell on the surface of the nanoparticles which has a lubricating effect which enhances the diffusion[36]. The insignificance can be related to the variations in viscosity between samples as one eye was used for a single tested compound and all samples were kept in an incubator set at 37 ºC. Additionally, the data in figure 4 is based on distance travelled and should be linked to the images in figure S2 , based on the assumption that PEGylated nanoparticles diffused first to the cisterns, PEGylated 750 and 10000 Da nanoparticles diffused faster through the cisterns as they are smaller than PEGylated 5000 Da nanoparticles. This random diffusion and leaking through these spaces give raise in the variation of distance travelled by different PEGylated nanoparticles in different areas of the cuvette and can lead to statistical insignificance. In fact, this represents the scenario in real life where liquefaction of the vitreous humour in the elderly can cause huge variation in diffusion compared to adolescent[47].

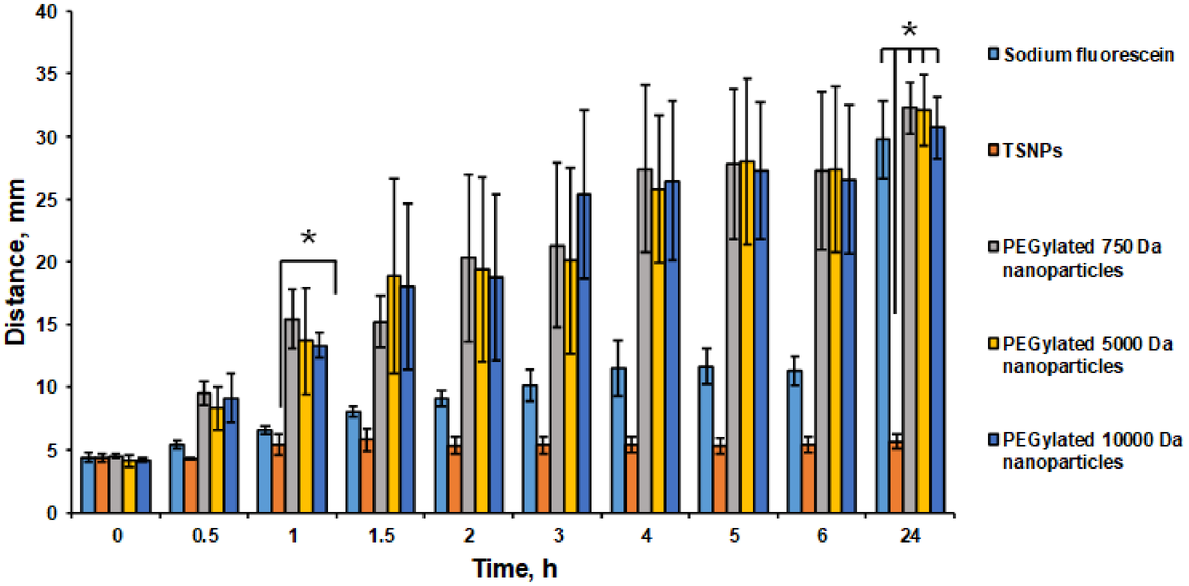

Figure 4: Distance travelled over time over time of thiolated, PEGylated (750, 5000, 10000 Da) nanoparticles and sodium fluorescein (n=3, mean ± SEM), values calculated using two-way ANOVA and Tukey's multiple comparisons test

Previously, the diffusion of these nanoparticles was studied in solutions of water-soluble polymers poly(acrylic acid) (PAA), poly(N-vinylpyrrolidone) (PVP), poly(ethylene oxide) (PEO), and hydroxyethylcellulose (HEC)[36]. The diffusion of the thiolated nanoparticles was in the following order HEC > PAA > PVP > PEO and for PEGylated nanoparticles it was PEO > HEC = PVP > PAA. Greater diffusivity of thiolated nanoparticles was related to the absence of the interaction with polymer and a low value was related to strong hydrogen bonding between the silanol group on the surface of the nanoparticle and oxygen in PVP and PEO. However, PEGylation enhanced the diffusion of the nanoparticles with variable degrees but exhibited different diffusivity in comparison to the thiolated counterparts. In case of vitreous humour, size and surface charge were reported as factors that can facilitate or hinder nanoparticles diffusion[9,16]. Similar to PVP, a possible hydrogen bonding formation between silanol groups in the nanoparticles and oxygen in hyaluronan in the vitreous humour which could be another reason for restriction of the diffusion of the bare nanoparticles. Shafai et al.[45] developed a vitreous mimic composed of hyaluronic acid (4.5 mg/mL) with complex viscosity of 0.3 ± 0.01 Pa which was demonstrated as a better mimic to human vitreous humour than bovine, ovine and porcine vitreous humour in terms of rheological properties and the the diffusion of sodium fluorescein. This human vitreous mimic can be a candidate to study and compare the diffusion of different tested drugs to vitreous humour models obtained from different animals using our method.

Positively charged polystyrene nanoparticles were reported to stay hindered after intravitreal injection to bovine eyes despite of their size, whereas, negatively charged counterparts diffused in variable degrees depending on the size. Nanoparticles functionalized with -COOH with size ranging from 100 to 1000 nm were used, with only 1000 nm nanoparticles did not diffuse. However, diffusion was achieved for 1000 nm nanoparticles when modified by PEGylation[16]. Although our thiolated silica nanoparticles are negatively charged, they stayed hindered on the surface of the vitreous humour due to the interaction with cysteine and formation of disulphide bonds and hydrogen bond formation between silanol groups and hyaluronan. Mun et al.[20] investigated the penetration of these nanoparticles through intact, de-epithelialized cornea and tissue pre-treated with cyclodextrin. They reported binding of the thiolated nanoparticles to the corneal surface and penetration of only PEGylated 5000 Da nanoparticles into the stroma in case of de-epithelialized cornea. PEGylation reduced the free thiol content to almost 50% and the formation of PEG shell on the surface of the nanoparticles reduces the number of thiol groups exposed to react with cysteine.

Generally, PEGylation was reported to improve diffusion viscous biological fluids and variation in chain length and grafting density has an effect on its flexibility and diffusion[40,49–53]. Variation of molecular weight and grafting density of PEG was reported to penetrate within brain tissue and to have a role on the mucoadhesion and mucopenetration of nanoparticles to human mucus and human cervicovaginal mucus[40,50–52]. The vitreous humour was reported as a barrier for nonviral ocular gene delivery due to aggregation of the formulation after intravitreal injection and this was avoided by PEGylation[53]. Sanders et al. prepared PEGylated (4 and 17% mol) and unmodified non-viral nucleic acid liposomes and injected into bovine vitreous humour and visualized using confocal scanning laser microscopy. They reported immediate aggregation of the unmodified liposomes after intravitreal injection whereas PEGylated liposomes with 4 % mol bound to fibrillar structure in the vitreous humour and liposomes with higher percentage of PEGylation were fully mobile in the vitreous humour[40].

It was also reported that increasing polymer grafting density decreases the mobility of its chains[54]. Polymers with short chains are less flexible and to achieve longer half-life high grafting density is required[55]. Nanoparticles with different sizes (80, 170 and 240 nm) were loaded with recombinant human tumour necrosis factor-α (rHuTNF-α) and grafted with three different molecular weights (2000, 5000 and 10000 Da) of methoxypolyethyleneglycol. A reduction in phagocytic uptake was observed in smaller particles grafted with higher molecular weight of PEG[55,56]. Yang et al. used computational investigation to study the effect of PEG chain length grafted on nanoparticles on the interaction between the nanoparticle and a biomembrane. They used coarse grained molecular dynamics simulations and found that long PEG chains undergo structural variations and dynamic behaviours which improves the elasticity of the PEGylated nanoparticles and supress the bending of the membrane. PEG chains form a soft elastic layer around the nanoparticle which can accommodate being flattened by the deformation of the membrane which is not the case with short PEG chains due to loss in flexibility[57]. Here, all our PEGylated nanoparticles carried a negative net charge which contributed to their diffusion. Additionally, PEGylated 750 Da nanoparticles, with the lowest molecular weight used formed brush conformation, had the highest grafting density and which contributed to its diffusion. PEGylated 5000 and 10000 Da nanoparticles formed longer brushes but with lower grafting densities. This brush length improved the elasticity and flexibility of the nanoparticles and facilitated their diffusion. Generally, PEGylation reduced the number of exposed thiol groups on the surface of the nanoparticles and formed a soft corona around the nanoparticles which facilitated their diffusion.

CONCLUSIONS

The diffusion of thiolated and PEGylated 750, 5000 and 10000 Da through the vitreous humour was exploited using a fast and simple experiment. This methodology can be used as a quick screening when choosing candidates in the process of developing of formulations to use for intravitreal injections. Although it was reported that small negatively charged nanoparticles can diffuse easily, our thiolated nanoparticles stayed hampered on the surface of the vitreous humour which was related to the surface chemistry of the nanoparticles. PEGylation reduced the number of exposed thiol and silanol groups and facilitated the diffusion of the nanoparticles through the vitreous humour. Additionally, PEG chain formed brush conformation with variable grafting densities which facilitated the diffusion of the modified nanoparticles.

Funding Sources

We acknowledge European Union's Horizon 2020 research and innovation programme under the Marie Skłodowska-Curie grant agreement Nanopol 823883.

ACKNOWLEDGMENT

We are thankful to Ministry of Higher Education, Research and Innovation, Sultanate of Oman, for a PhD scholarship for Jamila Al Mahrooqi. We acknowledge the assistance of Roman Moiseev in training me in sectioning bovine eyes and help in developing the protocol. We are grateful to staff in P.C. Turner Abattoir (Northcamp, UK) for providing bovine eyes used in this research.

REFERENCES

(1) Diebold, Y.; Calonge, M. Applications of Nanoparticles in Ophthalmology. *Prog. Retin. Eye Res.* **2010**, *29*, 596–609.

(2) Del Amo, E. M.; Rimpelä, A. K.; Heikkinen, E.; Kari, O. K.; Ramsay, E.; Lajunen, T.; Schmitt, M.; Pelkonen, L.; Bhattacharya, M.; Richardson, D.; Subrizi, A.; Turunen, T.; Reinisalo, M.; Itkonen, J.; Toropainen, E.; Casteleijn, M.; Kidron, H.; Antopolsky, M.; Vellonen, K. S.; Ruponen, M.; Urtti, A. Pharmacokinetic Aspects of Retinal Drug Delivery. *Prog. Retin. Eye Res.* **2017**, *57*, 134–185.

(3) Nagarwal, R. C.; Kant, S.; Singh, P. N.; Maiti, P.; Pandit, J. K. Polymeric Nanoparticulate System: A Potential Approach for Ocular Drug Delivery. *J. Control. Release* **2009**, *136*, 2–13.

(4) Sahoo, S. K.; Dilnawaz, F.; Krishnakumar, S. Nanotechnology in Ocular Drug Delivery. *Drug Discov. Today* **2008**, *13*, 144–151.

(5) Moiseev, R. V.; Morrison, P. W. J.; Steele, F.; Khutoryanskiy, V. V. Penetration Enhancers in Ocular Drug Delivery. *Pharmaceutics* **2019**, *11*, 1–33.

(6) Liu, S.; Dozois, M. D.; Chang, C. N.; Ahmad, A.; Ng, D. L. T.; Hileeto, D.; Liang, H.; Reyad, M. M.; Boyd, S.; Jones, L. W.; Gu, F. X. Prolonged Ocular Retention of Mucoadhesive Nanoparticle Eye Drop Formulation Enables Treatment of Eye Diseases Using Significantly Reduced Dosage. *Mol. Pharm.* **2016**, *13*, 2897–2905.

(7) Liu, S.; Jones, L.; Gu, F. X. Nanomaterials for Ocular Drug Delivery. *Macromol. Biosci.* **2012**, *12*, 608–620.

(8) Morrison, P. W. J.; Khutoryanskiy, V. V. Advances in Ophthalmic Drug Delivery. *Ther. Deliv.* **2014**, *5*, 1297–1315.

(9) Wilson, C. G.; Tan, L. E.; Mains, J. Principles of Retinal Drug Delivery from Within the Vitreous. In *Drug Product Development for the Back of the Eye*; Kompella, U. B., Edelhauser, H. F., Eds.; Springer, 2011; pp 125–158.

(10) Huang, X.; Chau, Y. Intravitreal Nanoparticles for Retinal Delivery. *Drug Discov. Today* **2019**, *24*, 1510–1523.

(11) Laude, A.; Tan, L. E.; Wilson, C. G.; Lascaratos, G.; Elashry, M.; Aslam, T.; Patton, N.; Dhillon, B. Intravitreal Therapy for Neovascular Age-Related Macular Degeneration and Inter-Individual Variations in Vitreous Pharmacokinetics. *Prog. Retin. Eye Res.* **2010**, *29*, 466–475.

(12) Fatt, I. Flow and Diffusion in the Vitreous Body of the Eye. *Bull. Math. Biol.* **1975**, *37* (1), 85–90.

(13) Maurice, B. D. M.; Street, J. Council, Ophthalmological. **1957**, 110–125.

(14) Fowlks, W. L. Meridional Flow from the Corona Ciliaris through the Pararetinal Zone of the Rabbit Vitreous. *Invest. Ophthalmol.* **1963**, *2*, 63–71.

(15) Wu, Z.; Troll, J.; Jeong, H. H.; Wei, Q.; Stang, M.; Ziemssen, F.; Wang, Z.; Dong, M.; Schnichels, S.; Qiu, T.; Fischer, P. A Swarm of Slippery Micropropellers Penetrates the Vitreous Body of the Eye. *Sci. Adv.* **2018**, *4*, 1–11.

(16) Xu, Q.; Boylan, N. J.; Suk, J. S.; Wang, Y. Y.; Nance, E. A.; Yang, J. C.; McDonnell, P. J.; Cone, R. A.; Duh, E. J.; Hanes, J. Nanoparticle Diffusion in, and Microrheology of, the Bovine Vitreous Ex Vivo. *J. Control. Release* **2013**, *167*, 76–84.

(17) Tavakoli, S.; Kari, O. K.; Turunen, T.; Lajunen, T.; Schmitt, M.; Lehtinen, J.; Tasaka, F.; Parkkila, P.; Ndika, J.; Viitala, T.; Alenius, H.; Urtti, A.; Subrizi, A. Diffusion and Protein Corona Formation of Lipid-Based Nanoparticles in the Vitreous Humor: Profiling and Pharmacokinetic Considerations. *Mol. Pharm.* **2021**, *18*, 699–713.

(18) Irmukhametova, G. S.; Mun, G. A.; Khutoryanskiy, V. V. Thiolated Mucoadhesive and PEGylated Nonmucoadhesive Organosilica Nanoparticles from 3-Mercaptopropyltrimethoxysilane. *Langmuir* **2011**, *27*, 9551–9556.

(19) Al Mahrooqi, J. H.; Mun, E. A.; Williams, A. C.; Khutoryanskiy, V. V. Controlling the Size of Thiolated Organosilica Nanoparticles. *Langmuir* **2018**, *34*, 8347–8354.

(20) Mun, E. A.; Morrison, P. W. J.; Williams, A. C.; Khutoryanskiy, V. V. On the Barrier Properties of the Cornea: A Microscopy Study of the Penetration of Fluorescently Labeled Nanoparticles, Polymers, and Sodium Fluorescein. *Mol. Pharm.* **2014**, *11*, 3556–3564.

(21) Henein, C.; Awwad, S.; Ibeanu, N.; Vlatakis, S.; Brocchini, S.; Khaw, P. T.; Bouremel, Y. Hydrodynamics of Intravitreal Injections into Liquid Vitreous Substitutes. *Pharmaceutics* **2019**, *11*, 1–19.

(22) Irmukhametova, G. S.; Fraser, B. J.; Keddie, J. L.; Mun, G. A.; Khutoryanskiy, V. V. Hydrogen-Bonding-Driven Self-Assembly of PEGylated Organosilica Nanoparticles with Poly(Acrylic Acid) in Aqueous Solutions and in Layer-by-Layer Deposition at Solid Surfaces. *Langmuir* **2012**, *28*, 299–306.

(23) Jokerst, J. V.; Lobovkina, T.; Zare, R. N.; Gambhir, S. S. Nanoparticle PEGylation for Imaging and Therapy. *Nanomedicine* **2011**, *6*, 715–728.

(24) Benoit, D. N.; Zhu, H.; Lilierose, M. H.; Verm, R. A.; Ali, N.; Morrison, A. N.; Fortner, J. D.; Avendano, C.; Colvin, V. L. Measuring the Grafting Density of Nanoparticles in Solution by Analytical Ultracentrifugation and Total Organic Carbon Analysis. *Anal. Chem.* **2012**, *84*, 9238–9245.

(25) Levin, C. S.; Bishnoi, S. W.; Grady, N. K.; Halas, N. J. Determining the Conformation of Thiolated Poly(Ethylene Glycol) on Au Nanoshells by Surface-Enhanced Raman Scattering Spectroscopic Assay. *Anal. Chem.* **2006**, *78*, 3277–3281.

(26) Marsh, D.; Bartucci, R.; Sportelli, L. Lipid Membranes with Grafted Polymers: Physicochemical Aspects. *Biochim. Biophys. Acta - Biomembr.* **2003**, *1615*, 33–59.

(27) Ways, T. M. M.; Lau, W. M.; Ng, K. W.; Khutoryanskiy, V. V. Synthesis of Thiolated, PEGylated and POZylated Silica Nanoparticles and Evaluation of Their Retention on Rat Intestinal Mucosa in Vitro. *Eur. J. Pharm. Sci.* **2018**, *122*, 230–238.

(28) Owens, D. E.; Peppas, N. A. Opsonization, Biodistribution, and Pharmacokinetics of Polymeric Nanoparticles. *Int. J. Pharm.* **2006**, *307*, 93–102.

(29) Dukes, D.; Li, Y.; Lewis, S.; Benicewicz, B.; Schadler, L.; Kumar, S. K. Conformational Transitions of Spherical Polymer Brushes: Synthesis, Characterization, and Theory. *Macromolecules* **2010**, *43*, 1564–1570.

(30) Shui, Y.; Su, Y.; Kuang, X.; Zhao, W.; Cai, Y.; Wang, D. Facile and Controllable Synthesis of Hybrid Silica Nanoparticles Densely Grafted with Poly(Ethylene Glycol). *Polym. Int.* **2017**, *66*, 1395–1401.

(31) Mansfield, E. D. H.; Filippov, S. K.; De, V. R.; Cook, M. T.; Grillo, I.; Hoogenboom, R.; Williams, A. C.; Khutoryanskiy, V. V. Understanding the Temperature Induced Aggregation of Silica Nanoparticles Decorated with Temperature-Responsive Polymers : Can a Small Step in the Chemical Structure Make a Giant Leap for a Phase Transition ? *J. Colloid Interface Sci.* **2021**, *590*, 249–259.

(32) Xia, X.; Yang, M.; Wang, Y.; Zheng, Y.; Li, Q.; Chen, J.; Xia, Y. Quantifying the Coverage Density of Poly(Ethylene Glycol) Chains on the Surface of Gold Nanostructures. *ACS Nano* **2012**, *6*, 512–522.

(33) de Gennes, P. G. Conformations of Polymers Attached to an Interface. *Macromolecules* **1980**, *13*, 1069–1075.

(34) Choi, C. H. J.; Zuckerman, J. E.; Webster, P.; Davis, M. E. Targeting Kidney Mesangium by Nanoparticles of Defined Size. *Proc. Natl. Acad. Sci. U. S. A.* **2011**, *108*, 6656–6661.

(35) Squires, T. M.; Mason, T. G. Fluid Mechanics of Microrheology. *Annu. Rev. Fluid Mech.* **2010**, *42*, 413–438.

(36) Mun, E. A.; Hannell, C.; Rogers, S. E.; Hole, P.; Williams, A. C.; Khutoryanskiy, V. V. On the Role of Specific Interactions in the Diffusion of Nanoparticles in Aqueous Polymer Solutions. *Langmuir* **2014**, *30*, 308–317.

(37) Käsdorf, B. T.; Arends, F.; Lieleg, O. Diffusion Regulation in the Vitreous Humor. *Biophys. J.* **2015**, *109*, 2171–2181.

(38) Mains, J.; Wilson, C. G. The Vitreous Humor as a Barrier to Nanoparticle Distribution. *J. Ocul. Pharmacol. Ther.* **2013**, *29*, 143–150.

(39) Varela-Fernández, R.; Díaz-Tomé, V.; Luaces-Rodríguez, A.; Conde-Penedo, A.; García-Otero, X.; Luzardo-álvarez, A.; Fernández-Ferreiro, A.; Otero-Espinar, F. J. Drug Delivery to the Posterior Segment of the Eye: Biopharmaceutic and Pharmacokinetic Considerations. *Pharmaceutics* **2020**, *12*, 1–39.

(40) Sanders, N. N.; Peeters, L.; Lentacker, I.; Demeester, J.; De Smedt, S. C. Wanted and Unwanted Properties of Surface PEGylated Nucleic Acid Nanoparticles in Ocular Gene Transfer. *J. Control. Release* **2007**, *122*, 226–235.

(41) Koo, H.; Moon, H.; Han, H.; Na, J. H.; Huh, M. S.; Park, J. H.; Woo, S. J.; Park, K. H.; Chan Kwon, I.; Kim, K.; Kim, H. The Movement of Self-Assembled Amphiphilic Polymeric Nanoparticles in the Vitreous and Retina after Intravitreal Injection. *Biomaterials* **2012**, *33*, 3485–3493.

(42) Von der Mark, K. Structure, Biosynthesis and Gene Regulation of Collagens in Cartilage and Bone. In *Dynamics of Bone and Cartilage Metabolism*; Seibel, M., Robins, S., Bilezikian, J., Eds.; Academic Press, 2006; pp 3–40.

(43) Ankamah, E.; Sebag, J.; Ng, E.; Nolan, J. M. Vitreous Antioxidants, Degeneration, and Vitreo-Retinopathy: Exploring the Links. *Antioxidants* **2020**, *9*, 1–20.

(44) Ansari, N.; Lodha, A.; Menon, S. K. Smart Platform for the Time since Death Determination from Vitreous Humor Cystine. *Biosens. Bioelectron.* **2016**, *86*, 115–121.

(45) Shafaie, S.; Hutter, V.; Brown, M. B.; Cook, M. T.; Chau, D. Y. S. Diffusion through the Ex Vivo Vitreal Body – Bovine, Porcine, and Ovine Models Are Poor Surrogates for the Human Vitreous. *Int. J. Pharm.* **2018**, *550*, 207–215.

(46) Tan, L. E.; Orilla, W.; Hughes, P. M.; Tsai, S.; Burke, J. A.; Wilson, C. G. Effects of Vitreous Liquefaction on the Intravitreal Distribution of Sodium Fluorescein, Fluorescein Dextran, and Fluorescent Microparticles. *Invest. Ophthalmol. Vis. Sci.* **2011**, *52*, 1111–1118.

(47) Wilson*, C. G.; Tan, L. E. Nanostructures Overcoming the Ocular Barrier: Physiological Considerations and Mechanistic Issues. In *Nanostructured Biomaterials for Overcoming Biological Barriers*; The Royal Society of Chemistry, 2012; pp 173–189.

(48) Jongebloed, W. L.; Worst, J. F. G. The Cisternal Anatomy of the Vitreous Body. *Doc. Ophthalmol.* **1987**, *67*, 183–196.

(49) Brittain, W. J.; Minko, S. A Structural Definition of Polymer Brushes. *J. Polym. Sci. Part A Polym. Chem.* **2007**, *45*, 3505–3512.

(50) Nance, E. A.; Woodworth, G. F.; Sailor, K. A.; Shih, T. Y.; Xu, Q.; Swaminathan, G.; Xiang, D.; Eberhart, C.; Hanes, J. A Dense Poly(Ethylene Glycol) Coating Improves Penetration of Large Polymeric Nanoparticles within Brain Tissue. *Sci. Transl. Med.* **2012**, *4*, 1–8.

(51) Lai, S. K.; O'Hanlon, D. E.; Harrold, S.; Man, S. T.; Wang, Y. Y.; Cone, R.; Hanes, J. Rapid Transport of Large Polymeric Nanoparticles in Fresh Undiluted Human Mucus. *Proc. Natl. Acad. Sci. U. S. A.* **2007**, *104*, 1482–1487.

(52) Wang, Y.-Y.; Lai, S. K.; Suk, J. S.; Pace, A.; Cone, R.; Hanes, J. Addressing the PEG Mucoadhesivity Paradox to Engineer Nanoparticles That "Slip" through the Human Mucus Barrier. *Angew. Chemie - Int. Ed.* **2008**, *47*, 9726–9729.

(53) Peeters, L.; Sanders, N. N.; Braeckmans, K.; Boussery, K.; Van De Voorde, J.; De Smedt, S. C.; Demeester, J. Vitreous: A Barrier to Nonviral Ocular Gene Therapy. *Investig. Ophthalmol. Vis. Sci.* **2005**, *46*, 3553–3561.

(54) Storm, G.; Belliot, S. O.; Daemen, T.; Lasic, D. D. Surface Modification of Nanoparticles to Oppose Uptake by the Mononuclear Phagocyte System. *Adv. Drug Deliv. Rev.* **1995**, *17*, 31–48.

(55) Fam, S. Y.; Chee, C. F.; Yong, C. Y.; Ho, K. L.; Mariatulqabtiah, A. R.; Tan, W. S. Stealth Coating of Nanoparticles in Drug-Delivery Systems. *Nanomaterials* **2020**, *10*, 1–18.

(56) Fang, C.; Shi, B.; Pei, Y. Y.; Hong, M. H.; Wu, J.; Chen, H. Z. In Vivo Tumor Targeting of Tumor Necrosis Factor-α-Loaded Stealth Nanoparticles: Effect of MePEG Molecular Weight and Particle Size. *Eur. J. Pharm. Sci.* **2006**, *27*, 27–36.

(57) Li, Y.; Hu, Y. Computational Investigation of the Influence of Chain Length on the Shielding Effect of PEGylated Nanoparticles. *RSC Adv.* **2014**, *4*, 51022–51031.

Diffusion of thiolated and PEGylated silica nanoparticles into vitreous humour

Jamila H. Al Mahrooqi[a,b], *Adrian C. Williams*[a], *Vitaliy V. Khutoryanskiy*[a]*

[a] Reading School of Pharmacy, University of Reading, Reading RG6 6AD, U.K.

[b] Oman College of Health Sciences, P.O.Box 1928, 114, Muttrah, Oman.

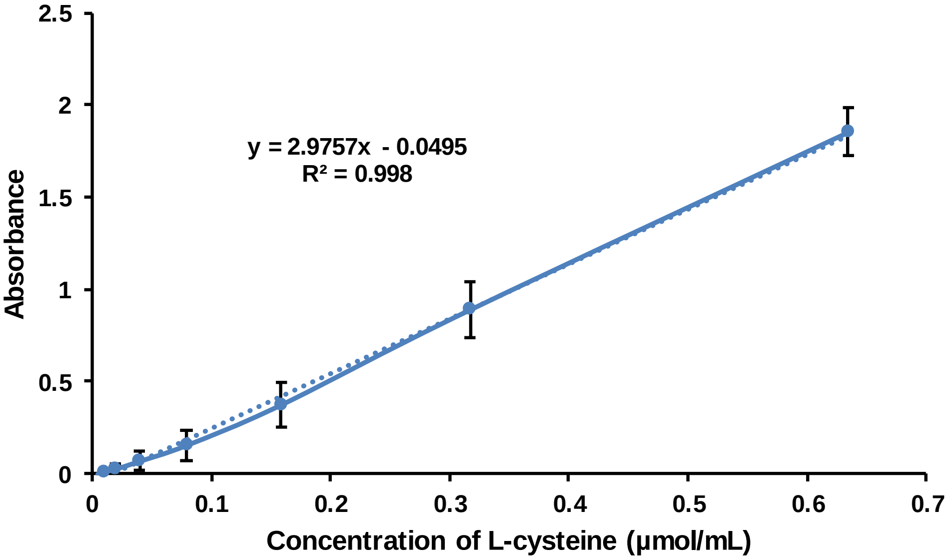

Figure S 1: L-cysteien calibration curve used for calculation of free thiol content in TSNPs and PEGylated TSNPs (n=3, mean ± SD).

Calculation of grafting density:

Grafting density was calculated using volume at different temperatures and the following values were obtained in chain/nm^2:

Table S1: Calculated PEG 750, 5000 and 10000 Da grafting density values, using volume, of nanoparticles in chain/nm^2 at different temperatures.

	450° C	500° C	550° C	593° C	Average
PEG 750 Da	15	13	11.2	11.2	12.6 ±1.8
PEG 5000 Da	2.9	2	2	2	2.2 ± 0.45
PEG 10000 Da	1	1	0.97	0.9	0.97 ± 0.05

When mass was used for the calculations, the error was less in comparison to calculations based on volume and the following values in chain/nm^2 were obtained:

Table S2: Calculated PEG 750, 5000 and 10000 Da grafting density values, using mass, of nanoparticles in chain/nm^2 at different temperatures.

	450^o C	500^o C	550^o C	593^o C	Average
PEG 750 Da	8.9	10.3	11.4	12	10.6 ±1.4
PEG 5000 Da	2.69	3.3	3.5	3.6	3.2 ± 0.4
PEG 10000 Da	1.7	2	2	2	1.9 ± 0.1

Details of calculations using mass are below:

Density of SiO_2 = 2.3 g/cm^3, volume of one nanoparticle = 47712.94 nm^3, area of one nanoparticle = 6362 nm^2

$$\text{Mass of one nanoparticle} = \text{density } \times \text{volume}$$

$$2.3\ \text{g/cm}^3 \times\ 10^{-21}\ \text{nm}^3\ \times 47712.94\ \text{nm}^3\ = 1.097\ \times 10^{-16}\ \text{g}$$

Residual weight of bare nanoparticles at 593^{o}C = 0.00139 g

$$\text{Number of nanoparticles} = \frac{\text{total mass of sample}}{\text{mass of a single nanoparticle}}$$

$$= \frac{0.00139\ \text{g}}{1.097\ \times 10^{-16}\ \text{g}} = 1.27\ \times 10^{13}$$

Residual weight of PEGylated 750 Da nanoparticles = 0.891 mg

Weight loss at 593^o C of PEGylated 750 nanoparticles = 2.197 – 0.891 = 1.306 mg

Weight of PEG 750 = 1.306 – (1.306 X 41%) = 1.306 – 0.53546 = 0.77054 mg

$$\text{Number of nanoparticles in sample} = \frac{0.891\ \text{mg}}{1.097\ \times 10^{-13}\ \text{mg}} = 8\ \times 10^{12}\ \text{particles}$$

$$\text{Number of PEG 750 Da molecues in sample} = \frac{0.77054\ \text{mg}\ \times 10^{-3} \times 6.022\ \times 10^{23}}{750}$$
$$= 6.19\ \times 10^{17}$$

$$\text{Number of PEG 750 Da/particle} = \frac{6.19\ \times 10^{17}}{8\ \times 10^{12}} = 77375$$

$$\text{Number of PEG 750 Da/nm}^2 = \frac{77375}{6362} = 12\ \text{chain/nm}^2$$

Residual weight of PEGylated 5000 Da nanoparticles = 0.527 mg

Weight loss at 593^o C of PEGylated 5000 nanoparticles = 2.067 – 0.527 = 1.54 mg

Weight of PEG 5000 = 1.54 – (1.54 X 41%) = 1.54 – 0.6314 = 0.9086 mg

$$\text{Number of nanoparticles in sample} = \frac{0.527\ \text{mg}}{1.097\ \times 10^{-13}\ \text{mg}} = 4.8\ \times 10^{12}\ \text{particles}$$

$$\text{Number of PEG 750 Da molecues in sample} = \frac{0.9086\ \text{mg}\ \times 10^{-3} \times 6.022\ \times 10^{23}}{750}$$

$$= 1.09\ \times 10^{17}$$

$$\text{Number of PEG 5000 Da/particle} = \frac{1.094\ \times 10^{17}}{4.8\ \times 10^{12}} = 22792$$

$$\text{Number of PEG 5000 Da/nm}^2 = \frac{22792}{6362} = 3.6\ \text{chain/nm}^2$$

Residual weight of PEGylated 10000 Da nanoparticles = 0.431 mg

Weight loss at 593° C of PEGylated 10000 nanoparticles = 1.855 – 0.431 = 1.424 mg

Weight of PEG 10000 = 1.424 – (1.424 X 41%) = 1.424 – 0.5838 = 0.8402 mg

$$\text{Number of nanoparticles in sample} = \frac{0.431\ \text{mg}}{1.097\ \times 10^{-13}\ \text{mg}} = 3.9\ \times 10^{12}\ \text{particles}$$

$$\text{Number of PEG 10000 Da molecues in sample} = \frac{0.8402\ \text{mg}\ \times 10^{-3} \times 6.022\ \times 10^{23}}{750}$$

$$= 5.06\ \times 10^{16}$$

$$\text{Number of PEG 10000 Da/particle} = \frac{5.06\ \times 10^{16}}{3.9\ \times 10^{12}} = 12974$$

$$\text{Number of PEG 10000 Da/nm}^2 = \frac{12974}{6362} = 2\ \text{chain/nm}^2$$

Residual weight of bare nanoparticles at 550°C = 0.00143 g

$$\text{Number of nanoparticles} = \frac{\text{total mass of sample}}{\text{mass of a single nanoparticle}}$$

$$= \frac{0.00143\ \text{g}}{1.097\ \times 10^{-16}\ \text{g}} = 1.3\ \times 10^{13}$$

Residual weight of PEGylated 750 Da nanoparticles = 0.933 mg

Weight loss at 550° C of PEGylated 750 nanoparticles = 2.197 – 0.933 = 1.264 mg

Weight of PEG 750 = 1.264 – (1.264 X 39%) = 1.264 – 0.49296 = 0.77104 mg

$$\text{Number of nanoparticles in sample} = \frac{0.933\ \text{mg}}{1.097\ \times 10^{-13}\ \text{mg}} = 8.5\ \times 10^{12}\ \text{particles}$$

$$\text{Number of PEG 750 Da molecues in sample} = \frac{0.77104\ \text{mg}\ \times 10^{-3} \times 6.022\ \times 10^{23}}{750}$$

$$= 6.19\ \times 10^{17}$$

$$\text{Number of PEG 750 Da/particle} = \frac{6.19\ \times 10^{17}}{8.5\ \times 10^{12}} = 72834$$

$$\text{Number of PEG 750 Da/nm}^2 = \frac{72834}{6362} = 11.4 \text{ chain/nm}^2$$

Residual weight of PEGylated 5000 Da nanoparticles = 0.554 mg

Weight loss at 550⁰ C of PEGylated 5000 nanoparticles = 2.067 – 0.5543 = 1.51 mg

Weight of PEG 5000 = 1.51 – (1.51 X 39%) = 1.51 – 0.5899 = 0.9201 mg

$$\text{Number of nanoparticles in sample} = \frac{0.554 \text{ mg}}{1.097 \times 10^{-13} \text{ mg}} = 5 \times 10^{12} \text{ particles}$$

$$\text{Number of PEG 5000 Da molecues in sample} = \frac{0.9201 \text{ mg} \times 10^{-3} \times 6.022 \times 10^{23}}{5000}$$
$$= 1.11 \times 10^{17}$$

$$\text{Number of PEG 5000 Da/particle} = \frac{1.11 \times 10^{17}}{5 \times 10^{12}} = 22163$$

$$\text{Number of PEG 5000 Da/nm}^2 = \frac{22163}{6362} = 3.5 \text{ chain/nm}^2$$

Residual weight of PEGylated 10000 Da nanoparticles = 0.453mg

Weight loss at 550⁰ C of PEGylated 10000 nanoparticles = 1.855 – 0.453 = 1.402mg

Weight of PEG 10000 = 1.402 – (1.402 X 39%) = 1.402 – 0.5468 = 0.8552 mg

$$\text{Number of nanoparticles in sample} = \frac{0.453 \text{ mg}}{1.097 \times 10^{-13} \text{ mg}} = 4 \times 10^{12} \text{ particles}$$

$$\text{Number of PEG 10000 Da molecues in sample} = \frac{0.8552 \text{ mg} \times 10^{-3} \times 6.022 \times 10^{23}}{10000}$$
$$= 5.15 \times 10^{16}$$

$$\text{Number of PEG 10000 Da/particle} = \frac{5.15 \times 10^{16}}{4 \times 10^{12}} = 12875$$

$$\text{Number of PEG 10000 Da/nm}^2 = \frac{12875}{6362} = 2 \text{ chain/nm}^2$$

Residual weight of bare nanoparticles at 500⁰C = 0.00152 g

$$\text{Number of nanoparticles} = \frac{\text{total mass of sample}}{\text{mass of a single nanoparticle}}$$

$$= \frac{0.00152 \text{ g}}{1.097 \times 10^{-16} \text{ g}} = 1.4 \times 10^{13}$$

Residual weight of PEGylated 750 Da nanoparticles = 1.025mg

Weight loss at 500⁰ C of PEGylated 750 nanoparticles = 2.197 – 1.025 = 1.172 mg

Weight of PEG 750 = 1.172 – (1.172 X 35%) = 1.172 – 0.4102 = 0.7618 mg

$$\text{Number of nanoparticles in sample} = \frac{1.025 \text{ mg}}{1.097 \times 10^{-13} \text{ mg}} = 9.3 \times 10^{12} \text{ particles}$$

$$\text{Number of PEG 750 Da molecues in sample} = \frac{0.7618\ \text{mg}\ \times 10^{-3} \times 6.022\ \times 10^{23}}{750}$$
$$= 6.12\ \times 10^{17}$$

$$\text{Number of PEG 750 Da/particle} = \frac{6.12\ \times 10^{17}}{9.3\ \times 10^{12}} = 65771$$

$$\text{Number of PEG 750 Da/nm}^2 = \frac{65771}{6362} = 10.3\ \text{chain/nm}^2$$

Residual weight of PEGylated 5000 Da nanoparticles = 0.609 mg

Weight loss at 500⁰ C of PEGylated 5000 nanoparticles = 2.067 – 0.609 = 1.458 mg

Weight of PEG 5000 = 1.458 – (1.458 X 35%) = 1.458 – 0.5103 = 0.9477 mg

$$\text{Number of nanoparticles in sample} = \frac{0.609\ \text{mg}}{1.097\ \times 10^{-13}\ \text{mg}} = 5.5\ \times 10^{12}\ \text{particles}$$

$$\text{Number of PEG 5000 Da molecues in sample} = \frac{0.9477\ \text{mg}\ \times 10^{-3} \times 6.022\ \times 10^{23}}{5000}$$
$$= 1.14\ \times 10^{17}$$

$$\text{Number of PEG 5000 Da/particle} = \frac{1.14\ \times 10^{17}}{5.5\ \times 10^{12}} = 20752$$

$$\text{Number of PEG 5000 Da/nm}^2 = \frac{20752}{6362} = 3.3\ \text{chain/nm}^2$$

Residual weight of PEGylated 10000 Da nanoparticles = 0.496 mg

Weight loss at 500⁰ C of PEGylated 10000 nanoparticles = 1.855 – 0.496 = 1.359mg

Weight of PEG 10000 = 1.359 – (1.359 X 35%) = 1.359 – 0.4756 = 0.8834 mg

$$\text{Number of nanoparticles in sample} = \frac{0.496\ \text{mg}}{1.097\ \times 10^{-13}\ \text{mg}} = 4.5\ \times 10^{12}\ \text{particles}$$

$$\text{Number of PEG 10000 Da molecues in sample} = \frac{0.8834\ \text{mg}\ \times 10^{-3} \times 6.022\ \times 10^{23}}{10000}$$
$$= 5.32\ \times 10^{16}$$

$$\text{Number of PEG 10000 Da/particle} = \frac{5.32\ \times 10^{16}}{4.5\ \times 10^{12}} = 11822$$

$$\text{Number of PEG 10000 Da/nm}^2 = \frac{11822}{6362} = 2\ \text{chain/nm}^2$$

Residual weight of bare nanoparticles at 450⁰C = 0.00165 g

$$\text{Number of nanoparticles} = \frac{\text{total mass of sample}}{\text{mass of a single nanoparticle}}$$

$$= \frac{0.00165\ \text{g}}{1.097\ \times 10^{-16}\ \text{g}} = 1.5\ \times 10^{13}$$

Residual weight of PEGylated 750 Da nanoparticles = 1.142 mg

Weight loss at 450º C of PEGylated 750 nanoparticles = 2.197 – 1.142 = 1.055 mg

Weight of PEG 750 = 1.055 – (1.055 X 30%) = 1.055 – 0.3165 = 0.7385 mg

$$\text{Number of nanoparticles in sample} = \frac{1.142\ \text{mg}}{1.097\ \times 10^{-13}\ \text{mg}} = 1.04\ \times 10^{13}\ \text{particles}$$

$$\text{Number of PEG 750 Da molecues in sample} = \frac{0.7385\ \text{mg}\ \times 10^{-3} \times 6.022\ \times 10^{23}}{750}$$
$$= 5.93\ \times 10^{17}$$

$$\text{Number of PEG 750 Da/particle} = \frac{5.93\ \times 10^{17}}{1.04\ \times 10^{13}} = 57016$$

$$\text{Number of PEG 750 Da/nm}^2 = \frac{72834}{6362} = 8.9\ \text{chain/nm}^2$$

Residual weight of PEGylated 5000 Da nanoparticles = 0.681 mg

Weight loss at 450º C of PEGylated 5000 nanoparticles = 2.067 – 0.681 = 1.386 mg

Weight of PEG 5000 = 1.386 – (1.386 X 30%) = 1.386 – 0.4158 = 0.9702 mg

$$\text{Number of nanoparticles in sample} = \frac{0.681\ \text{mg}}{1.097\ \times 10^{-13}\ \text{mg}} = 6.2\ \times 10^{12}\ \text{particles}$$

$$\text{Number of PEG 5000 Da molecues in sample} = \frac{0.9702\ \text{mg}\ \times 10^{-3} \times 6.022\ \times 10^{23}}{5000}$$
$$= 1.17\ \times 10^{17}$$

$$\text{Number of PEG 5000 Da/particle} = \frac{1.17\ \times 10^{17}}{6.2\ \times 10^{12}} = 18847$$

$$\text{Number of PEG 5000 Da/nm}^2 = \frac{18847}{6362} = 2.96\ \text{chain/nm}^2$$

Residual weight of PEGylated 10000 Da nanoparticles = 0.558 mg

Weight loss at 450º C of PEGylated 10000 nanoparticles = 1.855 – 0.558 = 1.297mg

Weight of PEG 10000 = 1.297 – (1.297 X 30%) = 1.297 – 0.3891 = 0.9079 mg

$$\text{Number of nanoparticles in sample} = \frac{0.558\ \text{mg}}{1.097\ \times 10^{-13}\ \text{mg}} = 5\ \times 10^{12}\ \text{particles}$$

$$\text{Number of PEG 10000 Da molecues in sample} = \frac{0.9079\ \text{mg}\ \times 10^{-3} \times 6.022\ \times 10^{23}}{10000}$$
$$= 5.47\ \times 10^{16}$$

$$\text{Number of PEG 10000 Da/particle} = \frac{5.47\ \times 10^{16}}{5\ \times 10^{12}} = 10935$$

$$\text{Number of PEG 10000 Da/nm}^2 = \frac{10935}{6362} = 1.7\ \text{chain/nm}^2$$

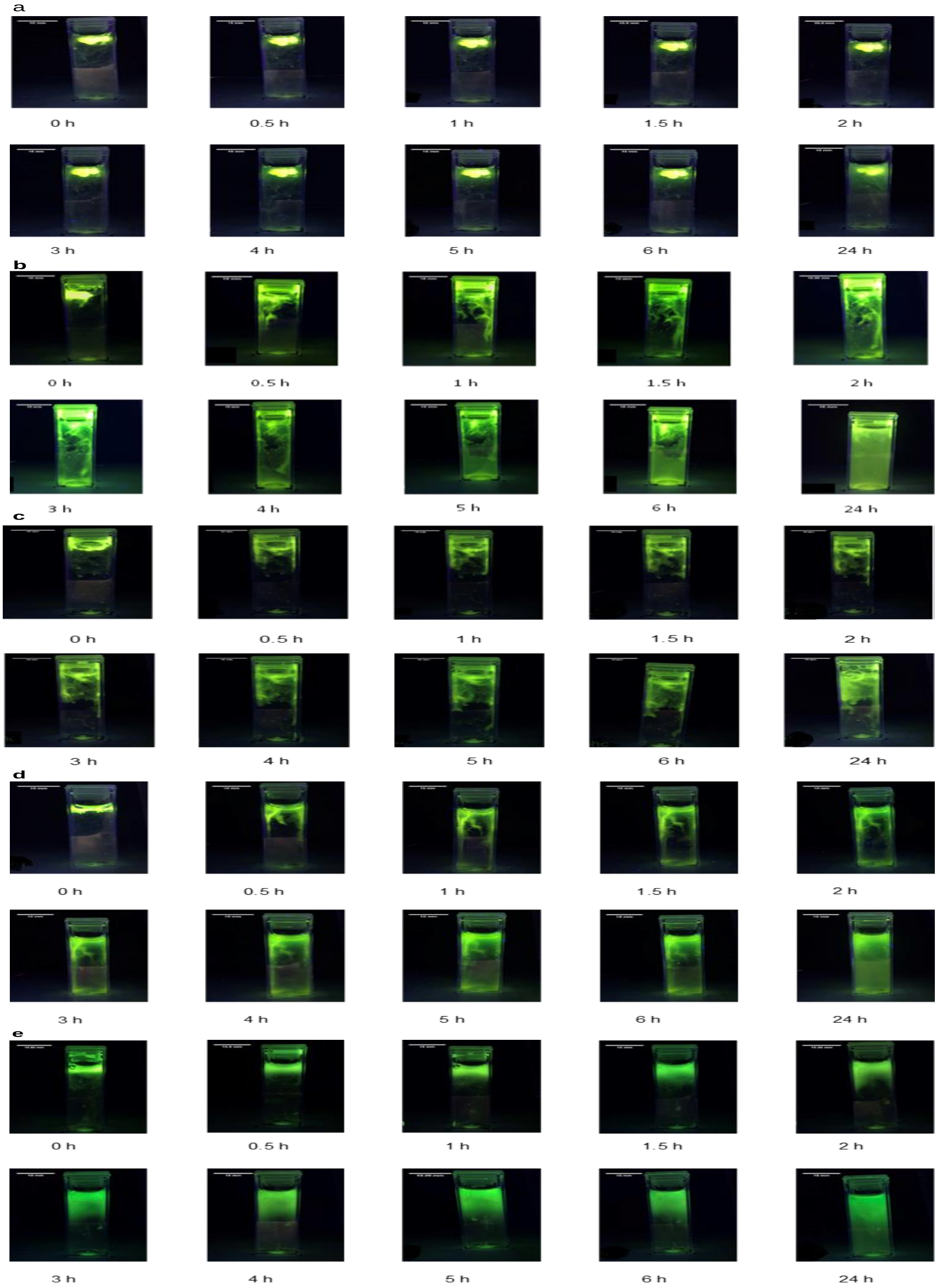

Figure S2: Diffusion study of thiolated (a), PEGylated 750 Da (b), 5000 Da (c), 10000 Da silica nanoparticles and sodium fluorescein into the bovine vitreous humour over time.

Chapter 5

General discussion and future work

General discussion

Nanosystems have gained great interest as carriers for targeted drug delivery to improve efficacy and reduce side effects. Silica is inert, biocompatible, stable, and can be easily functionalised with carboxylic, amino and thiol groups which make it a good candidate as a drug carrier [1]. In addition, it has been widely used as an additive in foods and cosmetics as it is recognised to be safe by US Food and Drug Administration (FDA) [2,3]. It is used in dentistry for tooth implants, orthopaedics as bone implants and in specialised medical devices such as ophthalmological and bio-glasses [4–7].

In this research thiol functionalised silica nanoparticles were synthesised and used as a model carrier for drug delivery. The first chapter provided an overview of thiol functionalised silica nanoparticles, various methods for their synthesis and possible biomedical and pharmaceutical applications. The presence of thiol groups on their surface facilitated their functionalisation with fluorescent dyes, polymers and loading with drugs. In addition, thiolated materials exhibited mucoadhesive properties which can be used for the development of promising mucoadhesive excipients for oral, nasal, ocular and intravesical drug delivery. The results of *in vivo* and *in vitro* experiments suggested potential applications for these nanoparticles in biomedical analysis, imaging, and as drug delivery systems. However, despite extensive research on the use of thiolated nanoparticles as delivery systems, progressing to clinical application is limited due the lack of information and studies on toxicity, degradation, and pharmacokinetics. In addition, translating the synthesis to large scale, producing particles with controlled size and reproducibility are further limiting factors.

The second chapter focused on the synthesis of thiolated silica nanoparticles using a modified Stöber method and exploited the reaction parameters that can be varied to produce nanoparticles with specific sizes. Particles prepared using the Stöber method are monodisperse, spherical, and electrostatically stabilised [7]. For drug carrier systems design, size, shape, and surface properties are important factors in ensuring drug delivery to the target site. Size plays an important role in nanoparticle circulation half-life, biodistribution, and clearance. For longer circulation half-life *in vivo*, higher intercellular uptake and reduced hepatic filtration, a particle size between 1 and 100 nm is required. However, nanoparticles smaller than 10 nm are cleared by the kidneys as they can easily exit the blood vessels. Contrarily, mononuclear phagocyte system cells capture larger particles. In addition to size, shape of the nanoparticles plays an important role in their internalisation and drug release [8]. Spherical nanoparticles were reported as good candidates for drug delivery due to the high likelihood of internalisation and faster internalisation than rod-shaped nanoparticles [9]. However, a higher probability of internalisation of rod shaped nanoparticles is achieved when their major axis is perpendicular to the cell membrane [10]. Surface properties include hydrophilicity and surface charge, where hydrophobic nanoparticles are prone to opsonisation and zeta potentials above (+/−) 30 mV are essential for stability in suspension and to prevent aggregation [8]. However, the size of nanoparticles typically prepared using the basic Stöber method ranges from 0.05 µm to 2 µm [7,11]. Therefore, the Stöber method was modified by Irmukhametova et al. and particles produced were spherical, sub-100 nm with zeta potential values around -37 mV [12]. This protocol was used in this study to explore the relationship between variable reaction conditions and particle size to enable rational design of thiolated silica nanoparticles with a predetermined size. Thus, a relationship between dielectric constant of the solvent or catalyst concentration and resulting particle size was established when using this protocol. The presence of thiol groups on the surface of these nanoparticles facilitated their modification with polymers and fluorescent dyes making them a good model for exploring targeted drug delivery in two different organs: hair follicles in skin and the ocular vitreous humour. However, the non-porous nature of these nanoparticles limits their loading with drugs.

The third chapter focused on the delivery of fluorescently labelled thiolated and PEGylated (750 and 5000 Da) nanoparticles to the hair follicles. Hair follicles can be a valuable route to deliver drugs in conditions such as alopecia and acne. In addition, this route can be used to deliver drugs to the lower layers of the skin without having to pass through the stratum corneum. As above, the size and surface chemistry of nanoparticles are important factors to consider when designing drug delivery systems. The presence of thiol groups on the surface of the nanoparticles is beneficial in mucosal tissues where mucoadhesion is required. However, penetration of thiolated nanoparticles to the hair follicles was hindered due to binding with keratin in the skin and hair. PEGylation reduced the number of exposed thiol groups and enhanced the penetration of PEGylated nanoparticles to variable degrees; particles coated with higher molecular weight PEG exhibited better penetration. In addition to the surface chemistry, size is another important factor that can be manipulated to target drug delivery to regions of the hair follicle. PEGylated 5000 Da nanoparticles sized 89 nm penetrated close to the bulge region deeper than those coated with PEG

750 Da. This was related to the difference in size, PEG chain length and flexibility. In order to achieve deeper penetration, nanoparticle size should be close to hair cuticles thickness which was reported to be around 500 nm for human hair [13]. Here, larger nanoparticles can be achieved by selecting the dielectric constant of the aprotic solvents as reported in chapter 2. Particles sized 455 nm were achieved by using a 1:1 ratio of THF/dioxane which can then be functionalised with PEG and their penetration to hair follicles can be explored. In addition, particles with variable sizes can be prepared and their penetration depth can be explored.

The fourth chapter investigated the diffusion of fluorescently labelled thiolated and PEGylated (750, 5000 and 10000 Da) in vitreous humour. Similarly to the skin, the eye is composed of complicated barriers which limit the delivery of drugs especially to the posterior segment. To deliver a drug to the retina it must be injected intravitreally and has to pass through the vitreous humour before reaching the internal limiting membrane which covers the retina and acts as a selective permeation barrier. Here, the diffusion of thiolated and PEGylated nanoparticles in the vitreous humour was explored using a simple fluorescence-based technique designed in this study. Again, size and surface chemistry of the particles enhanced or hindered the diffusion of nanoparticles in the vitreous humour. The mesh size of the bovine vitreous was reported to be in the range of 500 nm, therefore, nanoparticles must be smaller than this to facilitate their diffusion. In addition, the diffusion of anionic and neutral molecules is not restricted whereas cationic nanoparticles diffusion is restricted due to electrostatic interaction with hyaluronan [14–16]. Since both thiolated and PEGylated nanoparticles were sub-100 nm in size and negatively charged, diffusion was expected without restriction. Surprisingly, the diffusion of thiolated nanoparticles was hindered and they remained bound to the surface of the vitreous humour. These nanoparticles were reported to stay bound to the surface of corneal mucosa due to the formation of disulfide bonds between thiol groups and cysteine groups of mucins and PEGylated 5000 Da nanoparticles penetrated to the stroma when the cornea was de-epithelialized [12,17]. The vitreous humour contains structural proteins which include collagen II, IX, V/XI, fibrillin and cartilage oligomeric matrix proteins and non-structural proteins such as albumin and immunoglobulin. Collagen II was reported to be the most abundant protein and one of its splice variants codes for 69 cysteine-rich domains amino acids [18,19]. Moreover, cysteine, an amino acid highly reactive with thiol, is one of the non-enzymatic vitreous antioxidant systems [18]. Thus, the diffusion of thiolated nanoparticles was possibly hindered by cysteine. PEGylation reduced the thiol content by 50% and PEG forms a soft shell around the nanoparticles and masks the remining thiol groups which facilitated their diffusion.

These nanoparticles offer benefits in terms of stability, size control and ease of functionalisation with polymers and fluorescent tags. PEGylation in general improved and enhanced follicular delivery and vitreous diffusion of the nanoparticles. However, as the particles are non-porous, they cannot be loaded with drugs which is the main drawback for their application. Cargo can be linked to non-porous silica chemically via covalent bonding and the release profile will be controlled by the chemical linker, or by encapsulation and release is controlled by degradation [20]. Their size, easy functionalisation and stability make them a good model for research and promising for biomedical applications such as imaging.

Mesoporous silica nanoparticles (pore size 2- 50 nm) offer a better option for drug delivery as they can be loaded with drugs by physical or chemical adsorption and release at the target site. The release can be controlled by a “gatekeeper” or by manipulating the binding affinity of the drug by modifying the inner surface of the pores. The size of the mesoporous silica nanoparticles and their pores can be controlled by varying the concentration and composition of surfactants used during synthesis [20]. Several strategies have been used to functionalise mesoporous silica to achieve targeted and controlled drug release. Examples of surface functionalisation of mesoporous silica nanoparticles include functionalisation to achieve temperature, pH, light, ultrasound, and redox agent responsive properties [21]. To gain thermoresponsive properties, Poly(*N*-isopropylacrylamide) (PNIPAM), a known thermoresponsive polymer with lower critical solution temperature of 32-34 ºC, was modified to pyridine disulfide PNIPAM then conjugated to thiolated mesoporous silica nanoparticles. At temperatures below its critical solution temperature, it is water soluble, and it exhibits coil-to-globule transition above its critical solution temperature. It was used as a gatekeeper to block the pores of mesoporous silica at lower critical solution temperature after loading them with the bioactive molecules. The bioactive molecule is released when the nanoparticles are exposed to temperature higher than the lower critical solution temperature due to the formation of collapsed globules and exposure of the pores to the surrounding environment [22]. For light response release, sulforhodamine 101 was loaded to the pores of thiolated mesoporous silica and conjugated with (Ru(bpy)2(PPh3))Cl (bpy = bipyridine, PPh3 = triphenylphosphine). The capping molecule was triggered by irradiation with visible light (445 nm) and loaded molecules were released subsequently [23]. The role of glutathione as a redox molecule in degrading disulfide bonds and the release of cancer drugs such as doxorubicin loaded to the pores of thiolated mesoporous silica nanoparticles and degradation of the nanoparticles was extensively discussed in chapter 1. These are some examples of possible biomedical applications of thiolated mesoporous silica nanoparticles which were suggested in literature but as with non-porous silica further safety and toxicity studies are required.

The aims of this project have been achieved as a method to prepare nanoparticles with the desired size was developed. In addition, modification of the nanoparticles with PEG resulted in successful follicular delivery and diffusion in the vitreous humour. However, further research is required to investigate the safety and toxicity of this group of nanoparticles *in vivo* and *in vitro* with various physicochemical properties of the nanoparticles such as, size, shape, surface chemistry and solubility. The available toxicity reports indicating occupational inhalation exposure risk focused on natural crystalline silica particles with diameters 0.5- 10 µm [20].

Future work:

Controlled size synthesis, penetration to hair follicles and diffusion in the vitreous humour were investigated in this thesis. The mucoadhesion of these nanoparticles to several mucosal surfaces including the eye, urinary bladder, and the intestine was investigated previously. Based on the interesting properties of these nanoparticles including their small size, easy modification, colloidal stability, mucoadhesion, penetration and diffusion (after modification) they demonstrate a high potential for possible pharmaceutical application. However, being non-porous, the possibility of binding drugs covalently to the nanoparticles can be explored and a protocol can be developed. After successful binding, release studies can be carried and when efficient release is confirmed *in vitro* biological studies can be carried. In addition, cytotoxic assays to investigate the biocompatibility of thiolated and PEGylated silica nanoparticles are required. After successful *in vitro* studies and when confirmed to be biocompatible, *in vivo* studies can be planned and performed to explore the effect and pharmacokinetics of the drug covalently bound nanoparticles.

Alternatively, to exploit this research for targeted and controlled drug delivery, the approaches adopted here could be applied to mesoporous silica nanoparticles. The extent and ease of PEGylating mesoporous materials merits research and the impact of PEGylation on drug release and the influence on any gatekeeper systems attached would be of particular interest. Glutathione redox triggering can be used to release the drug when gatekeeper is attached to the mesoporous nanoparticles with disulfide bond.

Additionally, larger nanoparticles can produced by selecting the dielectric constant of the aprotic solvents as reported in chapter 2 to achieve deeper penetration to hair follicles as particles close to hair cuticle size were reported to have deeper penetration[13]. Particles sized 455 nm were achieved by using a 1:1 ratio of THF/dioxane which can then be functionalised with PEG and their penetration to hair follicles can be explored. In addition, particles with variable sizes can be prepared and their penetration depth can be explored. The same approach can be used to explore the diffusion of nanoparticles of different sizes before and after PEGylation on the diffusion of nanoparticles in the vitreous humour.

PEGylation was used to minimise opsonisation, prolong circulation time, and reduce side effects in case of IV administration and it showed improved penetration and diffusion in two different tissues in our research. PEG of two different molecular weights was used in the third chapter and of three different molecular weights in the fourth chapter. Grafting density and chain length were calculated in the fourth chapter to try to determine the conformation of the polymer chains and to correlate it to diffusion. However, it is interesting to prepare nanoparticles of the same size and decorate them with PEG with variable molecular weights and variable grafting densities to study the effect of varying the grafting densities within the same molecular weight of PEG on penetration and diffusion. Wang and co-workers reported rapid mucous penetration of particles with high surface coverage of low molecular weight PEG and increased mucoadhesion when particles were coated with high molecular weight PEG [24]. However, there is a lack in research, with few papers only, looking at effect of varying grafting density within PEG of the same molecular weight and with different molecular weights. Moreover, most of papers either do not mention grafting density or just mention it as one of the analysis carried for the decorated nanoparticles.

Another area for future study would be to compare PEGylation with other functional polymers such as poly(oxazolines) (POZ's); this was an initial area of research in this project but was limited due to time constrains. PEG is extensively used in research and preferred as it is already in clinical use, though some side effects were reported, but benefits of using it outweighed these risks. However, looking for another option and having variable choices in clinical use is advantageous in patients' care. POZ is a non-ionic polymer with many useful physicochemical properties, biocompatibility, and has stealth properties like PEG [25].

Our were tested the intestine as a model for nano-scale oral formulations as they are mucoadhesive. However, PEGylation and POZylation improved their muco-penetrating properties with variable degrees depending on the chain length [26]. Again, exploring the effect of grafting density and surface coverage on muco-penetrating properties is another field to explore as the interactions between the gastrointestinal mucous layer and nanoparticles are still poorly understood. Moreover, poorly absorbed drugs that are only given by injection is another area that can be targeted to establish absorption-enhancing nano-formulation [27].

Toxicity studies are another area of research which was not covered and need to be explored. Simple slug mucosal irritation test was previously carried on these nanoparticles and reported them as non-irritant [28]. Cell culture studies are still required and can be considered for future work. In addition, a planaria toxicity fluorescence protocol was developed by our research group as an assay for skin irritation and can be considered as one of the methods to study the skin irritability of these nanoparticles [29].

One of the richest areas of research is cancer therapy and nanotechnology for therapeutic drug delivery is studied to achieve targeted drug delivery and control drug release in addition to enhance drug absorption and permeability. It is believed that nanoparticle systems can avoid body's natural barriers resulting in avoiding early drug degradation or metabolism and successful delivery to the target site. Their size makes them able to interact successfully with biological molecules within cells and extracellularly which can be applied in cancer diagnosis and therapy [30]. Nanoparticles used in this research are easy and cheap to prepare, functionalised and can be easily labelled with fluorophore making them good candidates for imaging. They can be administered, and their journey can be tracked using different types of fluorescent microscopes. In addition, site-specific ligands such as, peptides, aptamers, or antibodies can be attached to the nanoparticles to achieve active targeted delivery. This is achieved by binding of the ligands onto receptors on the targeted cells resulting in highly site-specific targeting and more efficient treatment by avoiding unwanted cells. Another method of delivering therapeutic agent to tumour vasculature is passively by the enhanced permeability and retention effect. Nanosized therapeutic agent accumulate in the pores of rapidly forming tumour vasculature and stay trapped there due to poor lymphatic drainage resulting in high drug concentration in tumour site [30]. There is a wide range of cancers where studies have been carried and still there is much more to explore and huge area to research in cancer development, diagnostics, and treatment.

In addition to cancer, vaccines are another rich area of application of nanotechnology research. Due to their size, they facilitate the uptake into phagocytic cells resulting in efficient antigen recognition and presentation[31]. Research is ongoing to develop a vaccine for HIV and nanotechnology is one of the most popular carriers. Recently, a lipid based nanoparticles vaccine was developed and used to deliver mRNA in the COVID-19 pandemic [32]. The use of this vaccine opens the doors for more research on developing vaccines using nanotechnology.

Additionally, different delivery systems such as, lipid nanoparticles, liposomes, and polymeric nanoparticles (e.g., vesicles and solid nanoparticles) can be explored. These delivery systems can be used to encapsulate drugs for several delivery routes and among them liposomes are the most successful to date with many different formulations such as amphotericin and doxorubicin in clinical use. They are good drug delivery candidates for both topical and systemic formulations.

There is large body of research on the use of these delivery systems to deliver many diverse therapeutic agents including those which are poorly soluble.

Although there are over 50 nanomedicines are in clinical use, mainly for cancer therapy, there is a lack in regulation guidance. Challenges include deviation of nanomedicine pharmacokinetics from those of small molecules, issues of stability when scaled up, lack of unified global regulations and possible environmental impact. Due to this, whilst extensive research is undertaken with nanomaterials resulting in large number of publications, very few proceed to clinical trials and clinical application. Moreover, the urgent need for nanomedicines for the treatment of some diseases cannot be met under the current regulatory structure. More effort is required to unite regulations of nanomedicines use and regulations to push this field forward [33].

References:

(1) Foglia, M. L.; Alvarez, G. S.; Catalano, P. N.; Mebert, A. M.; Diaz, L. E.; Desimone, T. C. and M. F. Recent Patents on the Synthesis and Application of Silica Nanoparticles for Drug Delivery. *Recent Pat. Biotechnol.* **2011**, *5*, 54–61.

(2) Go, M.-R.; Bae, S.-H.; Kim, H.-J.; Yu, J.; Choi, S.-J. Interactions between Food Additive Silica Nanoparticles and Food Matrices. *Front. Microbiol.* **2017**, *8*, 10–13.

(3) Kasaai, M. R. Nanosized Particles of Silica and Its Derivatives for Applications in Various Branches of Food and Nutrition Sectors. *J. Nanotechnol.* **2015**, *2015*, 1–6.

(4) Lührs, A.-K.; Geurtsen, W. The Application of Silicon and Silicates in Dentistry: A Review. *Prog. Mol. Subcell. Biol.* **2009**, *47*, 359–380.

(5) Zhou, X.; Zhang, N.; Mankoci, S.; Sahai, N. Silicates in Orthopedics and Bone Tissue Engineering Materials. *J. Biomed. Mater. Res. Part A* **2017**, *105*, 2090–2102.

(6) Brunner, T. J.; Stark, W. J.; Boccaccini, A. R. Nanoscale Bioactive Silicate Glasses in Biomedical Applications. *Nanotechnologies Life Sci.* **2010**, *2*, 203–221.

(7) Gonçalves, M. C. Sol-Gel Silica Nanoparticles in Medicine: A Natural Choice. Design, Synthesis and Products. *Molecules* **2018**, *23*, 2021.

(8) Adamo, G.; Campora, S.; Ghersi, G. Functionalization of Nanoparticles in Specific

Targeting and Mechanism Release. In *Micro and Nano Technologies*; Ficai, D., Grumezescu, A. M. B. T.-N. for N. T., Eds.; Elsevier, 2017; pp 57–80.

(9) Chithrani, B. D.; Ghazani, A. A.; Chan, W. C. W. Determining the Size and Shape Dependence of Gold Nanoparticle Uptake into Mammalian Cells. *Nano Lett.* **2006**, *6*, 662–668.

(10) Champion, J. A.; Mitragotri, S. Role of Target Geometry in Phagocytosis. *Proc. Natl. Acad. Sci. U. S. A.* **2006**, *103*, 4930–4934.

(11) Stöber, W.; Fink, A.; Bohn, E. Controlled Growth of Monodisperse Silica Spheres in the Micron Size Range. *J. Colloid Interface Sci.* **1968**, *26*, 62–69.

(12) Irmukhametova, G. S.; Mun, G. A.; Khutoryanskiy, V. V. Thiolated Mucoadhesive and PEGylated Nonmucoadhesive Organosilica Nanoparticles from 3-Mercaptopropyltrimethoxysilane. *Langmuir* **2011**, *27*, 9551–9556.

(13) Lademann, J.; Patzelt, A.; Richter, H.; Antoniou, C.; Sterry, W.; Knorr, F. Determination of the Cuticula Thickness of Human and Porcine Hairs and Their Potential Influence on the Penetration of Nanoparticles into the Hair Follicles. *J. Biomed. Opt.* **2009**, *14*, 021014–4.

(14) Xu, Q.; Boylan, N. J.; Suk, J. S.; Wang, Y. Y.; Nance, E. A.; Yang, J. C.; McDonnell, P. J.; Cone, R. A.; Duh, E. J.; Hanes, J. Nanoparticle Diffusion in, and Microrheology of, the Bovine Vitreous Ex Vivo. *J. Control. Release* **2013**, *167*, 76–84.

(15) Peeters, L.; Sanders, N. N.; Braeckmans, K.; Boussery, K.; Van De Voorde, J.; De Smedt, S. C.; Demeester, J. Vitreous: A Barrier to Nonviral Ocular Gene Therapy. *Investig. Ophthalmol. Vis. Sci.* **2005**, *46*, 3553–3561.

(16) Del Amo, E. M.; Rimpelä, A. K.; Heikkinen, E.; Kari, O. K.; Ramsay, E.; Lajunen, T.; Schmitt, M.; Pelkonen, L.; Bhattacharya, M.; Richardson, D.; Subrizi, A.; Turunen, T.; Reinisalo, M.; Itkonen, J.; Toropainen, E.; Casteleijn, M.; Kidron, H.; Antopolsky, M.; Vellonen, K. S.; Ruponen, M.; Urtti, A. Pharmacokinetic Aspects of Retinal Drug Delivery. *Prog. Retin. Eye Res.* **2017**, *57*, 134–185.

(17) Mun, E. A.; Morrison, P. W. J.; Williams, A. C.; Khutoryanskiy, V. V. On the Barrier

Properties of the Cornea: A Microscopy Study of the Penetration of Fluorescently Labeled Nanoparticles, Polymers, and Sodium Fluorescein. *Mol. Pharm.* **2014**, *11*, 3556–3564.

(18) Ankamah, E.; Sebag, J.; Ng, E.; Nolan, J. M. Vitreous Antioxidants, Degeneration, and Vitreo-Retinopathy: Exploring the Links. *Antioxidants* **2020**, *9*, 1–20.

(19) Von Der Mark, K. Structure, Biosynthesis and Gene Regulation of Collagens in Cartilage and Bone. In *Dynamics of Bone and Cartilage Metabolism*; Seibel, M., Robins, S., Bilezikian, J., Eds.; Academic Press, 2006; pp 3–40.

(20) Tang, L.; Cheng, J. Nonporous Silica Nanoparticles for Nanomedicine Application. *Nano Today* **2013**, *8*, 290–312.

(21) Hoang Thi, T. T.; Cao, V. Du; Nguyen, T. N. Q.; Hoang, D. T.; Ngo, V. C.; Nguyen, D. H. Functionalized Mesoporous Silica Nanoparticles and Biomedical Applications. *Mater. Sci. Eng. C* **2019**, *99*, 631–656.

(22) You, Y.-Z.; Kalebaila, K. K.; Brock, S. L.; Oupický, D. Temperature-Controlled Uptake and Release in PNIPAM-Modified Porous Silica Nanoparticles. *Chem. Mater.* **2008**, *20*, 3354–3359.

(23) Knežević, N.; Trewyn, B. G.; Lin, V. S. Y. Functionalized Mesoporous Silica Nanoparticle-Based Visible Light Responsive Controlled Release Delivery System. *Chem. Commun.* **2011**, *47*, 2817–2819.

(24) Wang, Y.-Y.; Lai, S. K.; Suk, J. S.; Pace, A.; Cone, R.; Hanes, J. Addressing the PEG Mucoadhesivity Paradox to Engineer Nanoparticles That “Slip” through the Human Mucus Barrier. *Angew. Chemie - Int. Ed.* **2008**, *47*, 9726–9729.

(25) Mansfield, E. D. H.; Sillence, K.; Hole, P.; Williams, A. C.; Khutoryanskiy, V. V. POZylation: A New Approach to Enhance Nanoparticle Diffusion through Mucosal Barriers. *Nanoscale* **2015**, *7*, 13671–13679.

(26) Mansfield, E. D. H.; de la Rosa, V. R.; Kowalczyk, R. M.; Grillo, I.; Hoogenboom, R.; Sillence, K.; Hole, P.; Williams, A. C.; Khutoryanskiy, V. V. Side Chain Variations Radically Alter the Diffusion of Poly(2-Alkyl-2-Oxazoline) Functionalised Nanoparticles through a Mucosal Barrier. *Biomater. Sci.* **2016**, *4*, 1318–1327.

(27) Moss, D. M.; Curley, P.; Kinvig, H.; Hoskins, C.; Owen, A. The Biological Challenges and Pharmacological Opportunities of Orally Administered Nanomedicine Delivery. *Expert Rev. Gastroenterol. Hepatol.* **2018**, *12*, 223–236.

(28) Mun, E. A. Functionalised Organosilica Nanoparticles: Synthesis, Mucoadhesion and Diffusion, University of Reading, 2014.

(29) Shah, S. I.; Williams, A. C.; Lau, W. M.; Khutoryanskiy, V. V. Planarian Toxicity Fluorescent Assay: A Rapid and Cheap Pre-Screening Tool for Potential Skin Irritants. *Toxicol. Vitr.* **2020**, *69*, 105004.

(30) Manzur, A.; Oluwasanmi, A.; Moss, D.; Curtis, A.; Hoskins, C. Nanotechnologies in Pancreatic Cancer Therapy. *Pharmaceutics* **2017**, *9*, 39.

(31) Kim, M.-G.; Park, J. Y.; Shon, Y.; Kim, G.; Shim, G.; Oh, Y.-K. Nanotechnology and Vaccine Development. *Asian J. Pharm. Sci.* **2014**, *9*, 227–235.

(32) Shin, M. D.; Shukla, S.; Chung, Y. H.; Beiss, V.; Chan, S. K.; Ortega-Rivera, O. A.; Wirth, D. M.; Chen, A.; Sack, M.; Pokorski, J. K.; Steinmetz, N. F. COVID-19 Vaccine Development and a Potential Nanomaterial Path Forward. *Nat. Nanotechnol.* **2020**, *15*, 646–655.

(33) Foulkes, R.; Man, E.; Thind, J.; Yeung, S.; Joy, A.; Hoskins, C. The Regulation of Nanomaterials and Nanomedicines for Clinical Application: Current and Future Perspectives. *Biomater. Sci.* **2020**, *8*, 4653–4664.